Surface Brightness Fluctuations: An independent implementation of the method to uncover hidden stellar populations

Author:
L.M. (Lei) Titulaer

Supervisor:
Prof. dr. R.F. (Reynier) Peletier

Second reader:
Prof. dr. S.C. (Scott) Trager

June 23, 2024

Author: L.M. (Lei) Titulaer

Abstract

Surface Brightness Fluctuations (sbf) are variations in the smooth surface brightness profile of a galaxy due to the stochastic nature of the distribution of stars in the profile. The magnitude of these fluctuations is solely dependent on the distance to the galaxy and its underlying stellar population. Historically, sbf have mainly been used as a tool for measuring extragalactic distances, and it has been very successful to this extent. However, there consists a potential to use this method the other way around, and learn about stellar populations. Rodríguez-Beltrán et al. (2021) have shown that combining sbf-colors and standard integrated colors can potentially reveal hidden metal-poor components in elliptical galaxies. In this work, we provide an attempt to employ these results.

We provide a new implementation of the measurement pipeline required to measure the sbf magnitude. We use this implementation to measure the sbf magnitude in four different HST bands, ranging from the visible wavelengths to the infrared. We show that the parameter space that is populated by these galaxies in sbf color-space is vastly different from the parameter space covered using mean colors, confirming the predictions by Rodríguez-Beltrán et al. (2021). This indicates that the sbf method pertains an as of yet unemployed potential to learn about stellar populations in these galaxies.

Contents

1 Introduction

Surface brightness fluctuations (sbf) have been introduced by Tonry & Schneider (1988) as a technique that provided a new means to measure distance to galaxies. The technique is grounded in the idea that the smooth surface brightness profile of a galaxy is made up of individual stars. These stars are distributed discretely and randomly, which causes variance in the smooth profile of the galaxy. We can use techniques to measure this variance, ultimately allowing a measurement of the distance to the galaxy.

Conceptually, it is useful to consider a galaxy and visualising its individual stars. When a galaxy is close by, we can distinguish the individual stars in that galaxy, but once we move the galaxy further and further out, the stars tend to blend together into a smooth profile. However, although the profile looks smooth, the stars that make up the galaxy are still randomly distributed which leads to statistical fluctuations in the smooth profile distribution. Figure 1.1 aims to illustrate this idea idea by representing theoretical observations of a mock galaxy at various distances.

In a quantitative approach, we can understand surface brightness fluctuations as the intrinsic variance in the surface brightness divided by the average surface brightness. We can consider the simplified CCD model as presented by Cantiello & Blakeslee (2023) as to illustrate the mathematical description of surface brightness fluctuations that helps to provide a thorough understanding of the method. We consider a CCD image of a single stellar population, which for now we assume to be unblurred by the point spread function (PSF). We can consider L_* the luminosity per star, which we assume to be equal for all stars. n_* can be considered the average number of stars that we observe per pixel, and d the distance to the galaxy. The flux per star that reaches us can be represented by the scaling relation

$$f_* = \frac{L_*}{4\pi d^2}. \tag{1.1}$$

The flux that we measure per pixel is then given by the number of stars per pixel multiplied by the flux per star

$$F_* = f_* \cdot n_*. \tag{1.2}$$

But, since the number of stars per pixel scales with d^2 and Equation 1.1 shows that f_* scales with d^{-2}, the mean flux that we measure per pixel, the surface brightness F_*, is independent of distance d.

Similarly, we can represent the standard deviation of the surface brightness per pixel σ_{F_*}, by considering the fluctuations in the number of stars per pixel. The number of stars per pixel is Poisson distributed and thus its noise is Poissonian; $\sigma_{n_*} = \sqrt{n_*}$. This yields a standard deviation on the surface brightness of

$$\sigma_{F_*} = \sqrt{n_*} \cdot f_*. \tag{1.3}$$

As the sbf flux is defined as the ratio between the variance of the surface brightness profile to the mean (Tonry & Schneider, 1988), we yield

$$\overline{f} = \frac{\sigma_{F_*}^2}{F_*} = \frac{n_* \cdot f_*^2}{n_* \cdot f_*} = f_* = \frac{L_*}{4\pi d^2}. \tag{1.4}$$

We can see that see that the sbf flux is solely dependent on the luminosity per star L_* and the distance to the galaxy d.

Generalising this to a less trivial example in which the flux per star is not uniform for each star, we get (Moresco et al., 2022)

$$\overline{f} = \frac{\sum_i n_i f_i^2}{\sum_i n_i f_i} \equiv \frac{\overline{L}}{4\pi d^2}, \tag{1.5}$$
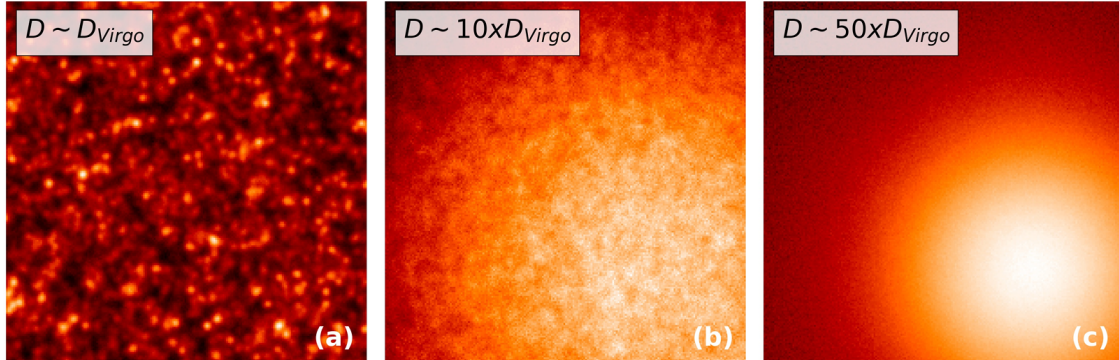
Figure 1.1: Illustration of the concept of surface brightness fluctuations. Each frame shows a simulation of an elliptical galaxy, as if it would be observed in one hour with the European Extremely Large Telescope (E-ELT, Gilmozzi & Spyromilio, 2007). Frame (a) corresponds to a distance of the Virgo galaxy (~ 16.5 Mpc). Frame (b) is an observation as if the galaxy would be 10 times as distant, and frame (c) shows a galaxy 50 times as distant. The image is taken from the review on surface brightness fluctuations by Cantiello & Blakeslee (2023).

with n_i the number of stars that correspond to a flux f_i, with $i = 1, \ldots, N$ covering the whole flux range of given stellar population. $\overline{L}$ is equal to the ratio of the second and first moments of the stellar luminosity function. The way of describing sbf as in Equation 1.5 is generally the way that is presumed in the context of stellar population models.

The sbf flux can then be converted to an sbf magnitude through

$$\overline{m} = -2.5 \log(\overline{f}) + m_0, \tag{1.6}$$

where m_0 is the zero-point magnitude of the magnitude system. This allows for a distance to be inferred from the distance modulus $(\overline{m} - \overline{M})$, with $\overline{M}$ is the absolute sbf magnitude. In order to know $\overline{M}$, calibrations are required. These can be made either theoretically with stellar population models, or empirically based on zero-points determined with other methods. The empirical approach, in which absolute sbf magnitudes are calibrated with broad-band colors, is generally most often employed.

An important characteristic of the sbf signal is the squared weighting of f_i in the numerator of Equation 1.5. The effect thereof is that the sbf signal is particularly sensitive to the brightest stars in a population. In old stellar populations, red giants dominate the sbf signal, whereas in composite stellar populations sbf are especially sensitive to the presence of young stars, even though these stars might contribute little to the mean luminosity of the galaxy (e.g. Rodríguez-Beltrán et al., 2021). Star formation thus can have a large effect on the sbf flux, which is the reason that galaxies that are actively star forming are generally avoided in sbf measurements to determine distance. Early type galaxies that tend to be dominated by old stellar populations are generally the preferred targets for sbf measurements. For these galaxies, the sbf calibration tends to be much better pronounced.

Historically, sbf have been used mainly as a means to determine distance to galaxies. That is, to assume knowledge about the stellar population $\overline{L}$ in Equation 1.5, and use the sbf measurement to infer the distance d. Advancements in the sbf method have mainly been focused into that direction, resulting mainly in works that provide sbf magnitudes in single filter bands. However, the sbf method also has the potential to work in the other direction, meaning to assume knowledge about the distance to the galaxy, and infer information about the stellar populations present. In a recent work, Rodríguez-Beltrán et al. (2021) have shown that sbf could pertain the potential to reveal composite stellar populations in massive galaxies. However, this would require consistent

sbf measurements in multiple wavelengths, which are currently not widely available.

In this work we will make an attempt to fill this gap by providing consistent sbf measurements in a number of wavelength bands. We will provide an independent implementation of the pipeline required to measure the sbf amplitude and will comment on each of the individual processing steps and their importance for accurately measuring the sbf magnitude. With the framework in place, we will provide measurements of the sbf magnitude in multiple wavelength bands and show how sbf colors differ from mean colors to potentially learn about stellar populations.

2 Implementation and background

The following section highlights the existing theoretical frameworks of sbf measurements. The general processing steps required to measure the sbf magnitude is given in Section 2.1. Section 2.2 succeeds with a short review of the work into sbf as a distance indicator, and an overview of the advances that have been made for sbf in the context of stellar population studies is provided in Section 2.3.

2.1 Measuring sbf

To measure the sbf flux from a ccd image in practice, a number of steps need to be performed. We give a summary of the generally required sbf measurement steps as in e.g. Tonry et al. (1990); Cantiello et al. (2005); Jensen et al. (2015); Carlsten et al. (2019b).

Given that we have a ccd image of a galaxy, cleaned of detector defects and cosmic rays, we must first estimate and subtract the background level. The next step is to make a smooth model of the mean galaxy surface brightness profile, and subtract that from the original data to obtain a residual frame. In this residual frame, fore and background sources need to be masked that do not contribute to the sbf signal. We then divide the residual masked image by the square root of the smooth model to obtain the normalised residual image. The fluctuations that are present in this image are a combination of the surface brightness fluctuations, which are convolved with the point spread function (PSF), and the detector noise, which is flat noise. These noise components can be disentangled in Fourier space. Therefore, the normalised residual image is Fourier transformed and the azimuthal average of the Fourier transform is taken to obtain the image power spectrum $P(k)$, which is the Fourier power as a function of wavenumber k. The sbf power can then be estimated fitting

$$P(k) = P_0 \cdot E(k) + P_1, \tag{2.1}$$

where P_1 is the power due to detector noise, P_0 corresponds to the power due to the sbf, and $E(k)$ is the expected power spectrum, which is a combination of the PSF power spectrum convolved with the mask power spectrum.

When masking fore and background sources, we are not able to mask sources beyond some detection limit. Hence, the measured sbf power P_0 must be corrected for flux coming from unmasked globular clusters and background galaxies. This power is represented by P_r. The final sbf magnitude is then represented by

$$\overline{m} = -2.5 \log(P_0 - P_r) + m_0, \tag{2.2}$$

with again m_0 the photometric zero point of the system. $P_0 - P_r$ represents the sbf flux $\overline{f}$ as in Equation 1.5.

We then require a calibration of the absolute sbf magnitude $\overline{M}$, often by calibrating with broadband color, in order to estimate the distance to the galaxy. Although the explanation in this subsection is rather sparse and not complete, it does give some insight in the steps required for the sbf signal to be measured, which might help interpreting some information in the subsequent

sections. In Section 4 we will then proceed with a detailed explanation of the sbf measurement employed in this work.

2.2 Sbf as a distance indicator

Historically, sbf have primarily been used as a method to measure distances to galaxies. Ever since the method has been introduced, efforts have been made to improve the method, with the main focus being to reduce uncertainties to probe outward as far as possible. With this goal in mind, developments have in specific lead to calibrations for large, elliptical galaxies, that have old, red populations for which the surface brightness fluctuations are bright in red and (near) infrared wavelengths, and for which the ralation between color and abolute sbf magnitude is relatively stable (e.g. Cantiello & Blakeslee, 2023).

After introduction of the sbf method by Tonry & Schneider (1988), who introduced the method as a technique for measuring extragalactic distances, efforts have been made to calibrate the method. Already in 1990, Tonry et al. (1990) have measured sbf magnitudes in the V, R, and I band, as to investigate the potential of the method. They provided the first theoretical calibration by calculating theoretical sbf magnitudes using isochrones to model stellar populations with a range of metallicity, age and mass. They found that, while $\overline{M}_V$ and $\overline{M}_R$ turned out to be very sensitive to age and metallicity, $\overline{M}_I$ seemed very stable. This was the first indication that redder wavebands could provide suitable, stable calibrations. Empirical calibrations quickly followed by Ajhar et al. (1997) and Tonry et al. (1997), who provided the first zero-point calibrations using Cepheid variables in the bulges of spiral galaxies in the I-band in combination with $V - I$ colors. These calibrations have lead to a first proper attempt on a measurement of the Hubble-Lemaître constant using sbf distances by Tonry et al. (2001).

In the decade that followed, the availability of space-based observations with HST provided a rapid advancement leading to new, mainly empirical calibrations. Surveys into the Virgo cluster (ACSVCS, Côté et al., 2004) and the later the Fornax cluster (ACSFCS Jordán et al., 2007) have lead to multiple improvements, guidelines and detailed descriptions of the sbf method (Jordán et al., 2004; Mei et al., 2005a,b). This series of papers have lead to calibrations in the z-band for the Wide Field Channel of the Advanced Camera for Surveys (ACS WFC) (Mei et al., 2007) which allowed (relative) distance measurements to the Virgo and Fornax clusters (Blakeslee et al., 2009). Parallel to this, numerous works have provided calibrations for the alternative optical bands not in the ACSVCS or ACSFCS (Cantiello et al., 2005; Biscardi et al., 2008; Blakeslee et al., 2010) as well as for the near-infrared bands (Jensen et al., 2001, 2003).

After installment of the Wide Field Camera 3 on the Hubble Space Telescope in 2009 (Dressel, 2015), the infrared bands provided an exquisite opportunity for new sbf measurements, reaching further out than before. This is because in the infrared the ratio between the luminosities of the red giants and dwarfs contributing most in these bands are much larger than is the case in the optical. Jensen et al. (2015) provided calibrations for both the F160W band as well as the F110W band. Using these calibrations, Jensen et al. (2021) have presented the most extended and complete sbf survey thus far, in which they have sampled 63 bright, early type galaxies in the F110W filter of HST WFC3. These sbf distances out to 100 Mpc were used in Blakeslee et al. (2021) to provide a new measurement of the Hubble-Lemaître constant.

While the space-based surveys have provided accurate sbf measurements, Cantiello et al. (2018b) has shown that also with ground-based surveys, good sbf measurements can be achieved, though reaching out less deep than with space-based data. Using imaging in various bands from the Next Generation Virgo Cluster Survey (NGVS, Ferrarese et al., 2012) on the Canada-France-Hawaii Telescope (CFHT), Cantiello et al. (2018b) provide a calibration in the i-band, using multiple colors for the color-sbf magnitude relation, as opposed to single color relations. Cantiello et al. (2024) use these calibrations to provide a detailed catalog of distances to individual galaxies in

the Virgo cluster.

The empirical calibration of the sbf distance scale has for a large share depended on the zero-point as calibrated with Cepheid distances. Calibrations by Tonry et al. (2001) and Blakeslee et al. (2002) based on Cepheid distances by Freedman et al. (2001) have shown a good correlation and align with estimates from stellar population models (Blakeslee, 2012). While the cepheid calibrations show a relatively good relation, an important issue is that the galaxies for which Cepheid distances are available, are generally not the ideal targets for sbf measurements due to the underlying stellar populations.

Hence, in a more recent effort, combining sbf distances with tip of the red giant branch (TRGB) distances has provided new, independent calibrations (Mould & Sakai, 2009; Carlsten et al., 2019b; Kim & Lee, 2021; Blakeslee et al., 2021). The advantage with the TRGB calibration is that the underlying populations on which the SBF and TRGB method are based are similar (e.g. Cantiello & Blakeslee, 2023). In general, the TRGB calibrations are in good correspondence with Cepheid calibrations. These have also been cross-matched with type Ia supernovae (SNe Ia) distances estimated from SNe Ia light-curve fits, again showing good correspondence (Garnavich et al., 2023).

Sbf distances measured in the classical way have been used among others to confirm distance to dark matter deficient dwarf systems (Van Dokkum et al., 2018; Blakeslee & Cantiello, 2018), investigate the structure of nearby clusters such as Virgo (Mei et al., 2007; Cantiello et al., 2018b, 2024), Fornax (Blakeslee et al., 2009), and the Hydra and Centaurus clusters (Mieske & Hilker, 2003; Mieske et al., 2005), and to study the populations of satellite and dwarf galaxies (Cohen et al., 2018; Carlsten et al., 2019b; Kim et al., 2022). Cantiello et al. (2018a) have used sbf to measure distance to the well known binary neutron star merger GW170817. In a number of works that have provided calibrations for the sbf distance using a reasonable sample, an attempt has been made to estimate the Hubble-Lemaître constant H_0 (Tonry et al., 2001; Blakeslee et al., 2002; Jensen et al., 2001; Biscardi et al., 2008; Jensen et al., 2021). In other recent works, Khetan et al. (2021) provide a measurement of the Hubble-Lemaître constant using sbf as a calibration for SNe Ia distances, and Uddin et al. (2023) combine sbf distances with Cepheid and TRGB distances to calibrate SNe Ia in a similar manner to determine H_0.

2.2.1 Dwarfs and Satellites

Besides the more classical approach, in which sbf are used to determine distance to mainly elliptical galaxies, some works have also attempted to provide calibrations towards the bluer part of the spectrum, and focusing more towards dwarfs and dwarf ellipticals, sometimes in more large scale surveys. Mieske et al. (2006) provided a calibration towards the bluer colors in the I-band, the regime of dwarf elliptical galaxies (dEs). More recently, Carlsten et al. (2019b) have provided calibrations and advice for measuring sbf distances to dwarf and satellite galaxies using CFHT imaging. In a number of papers that have followed, these calibrations have been used to evaluate the satellite system of M101 (Carlsten et al., 2019a), and extended this by looking into satellite systems by characterising host galaxies in the local volume (Carlsten et al., 2020, 2021). They finally obtain a very detailed and complete characterisation of the satellites in the systems of 31 Milky Way-like hosts in the Local Volume (Carlsten et al., 2022).

While Carlsten et al. (2022) provide one of the most detailed large studies into faint galaxies, some attempts have also been made to study what the implications of varying stellar populations are on sbf measurements. Greco et al. (2021) investigate the potential to measure distance to low-luminosity systems using stellar population models. Foster et al. (2024) try to measure sbf distances to irregular dwarfs in the COSMOS field using HST, but find it to be difficult for sbf to be properly measured for these systems. Kim & Lee (2021) provide another new calibration for sbf magnitudes extending into the blue regime, for the i-band of the Hyper Suprime-Cam (HSC) magnitude system. They do find a lower scatter at these wavelenghts than previously assumed. Polzin

et al. (2021) were able to use sbf to estimate the distance to a low-mass, likely quenched dwarf in the COSMOS field, allowing for a detailed study of the dwarf and its quenching mechanism.

2.3   Stellar populations studies with sbf

While most calibrations for sbf magnitudes are empirical, with the exception of Biscardi et al. (2008), many works do place their empirical sbf measurements within a theoretical stellar populations framework to validate their calibrations (e.g. Tonry et al., 1990; Jensen et al., 2003, 2015; Cantiello et al., 2018b; Carlsten et al., 2019b). But as already pointed out, the sensitivity of the amplitude of the luminosity fluctuations on the underlying stellar population could potentially uncover unknown information about the underlying populations.

Worthey (1993) and Buzzoni (1993) have provided stellar population synthesis models to study the first calibrations by Tonry et al. (1990). They ave both pointed out the sensitivity of the calibrations towards the blue wavelength bands. Opposed to what Tonry et al. (1990) proposed, Worthey (1993) were not able to find evidence for composite stellar populations in old elliptical galaxies. On the other hand, Buzzoni (1993) do point out the sensitivity of the sbf signal to (small) metal-poor components in the stellar population.

Cantiello et al. (2003) have provided a detailed study of theoretical sbf calibrations using single stellar population models. They have pointed out how sbf colors can be used in combination with mean colors to disentangle stellar population properties. In line with e.g. Worthey (1994), they find that using the right filters, sbf colors might be able to break down the age-metallicity degeneracy in stellar populations. These results are in line with those by Blakeslee et al. (2001), who additionally include composite stellar population models. In line with Buzzoni (1993) they point out the sensitivity of the sbf in early type populations to metal-poor components.

While calibrations with stellar population models have been prevalent, developments into further exploiting the potential for stellar population studies with sbf have been rather modest, partly due to multi-band sbf data being not prevalent (as pointed out by e.g. Rodríguez-Beltrán et al. (2021)). Although most sbf studies have been photometric, the method can also be employed in spectroscopy. Buzzoni (1993) have already depicted the first sbf spectrum in their stellar population study using sbf. Mitzkus et al. (2018) ave presented the first measurement of an SBF spectrum for a real galaxy, using data from the MUSE integral field spectroscopy (IFS) instrument. They apply the sbf method as presented in Tonry & Schneider (1988) to several thousand "pseudo-images" sampling various wavelength ranges, to yield a full sbf spectrum. They also present a stellar population synthesis tool that predicts sbf spectra, to place their measured spectrum in perspective. They find how these sbf spectra can set further constraints on stellar population parameters, indicating the potential to uncover the brightest stars in a population. In response, Vazdekis et al. (2020) present a library of sbf spectra covering a wide range of age, metallicity and initial mass functions. They indicate how these spectra can uncover metal-poor components in early type galaxies. This is remarkable due to the mean spectra being dominated by the old, metal rich populations, completely hiding this metal-poor component in the mean-photometric bands. This is illustrated by the sbf spectra presented in Figure 2.1. The secondary metal-poor component cannot be distinguished in the mean spectrum, but does become very clear using the sbf spectrum.

Rodríguez-Beltrán et al. (2021) build further on the sbf spectra presented by Vazdekis et al. (2020) and present a framework that allows unraveling secondary stellar populations using sbf colors in combination with mean colors. They create a large grid of composite sbf spectra, in which they mix a dominant population with a secondary population. They cover a large range of stellar population parameters, yielding mean and sbf spectra for a total of 178,200 different composite stellar populations (CSP). They integrate these spectra into various filter systems, and show how the combination of mean and sbf colors can be a promising tool for unraveling secondary stellar populations, by exploiting the difference in spectrum that is also illustrated in Figure 2.1.
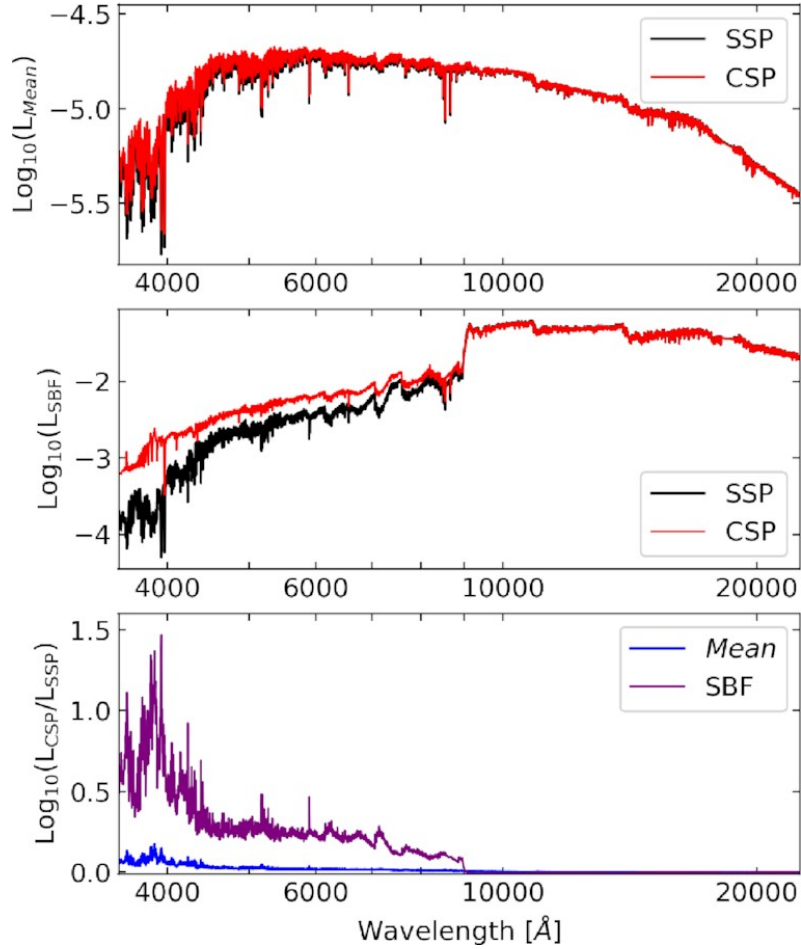
Figure 2.1: Example of sbf spectra for a composite stellar population. The red curve corresponds to a single stellar population (with a metallicity $M_1 = 0.15$), where the black curve is a composite stellar with the main component similar to the red curve mixed with a 4% metal-poor component tat has a metallicity $M_2 = -1.79$. The top frame shows the normalised *mean* spectra, whereas the bottom frame depicts the radio between the two spectra for the mean (blue) and sbf (purple) properties. The image is taken from Rodríguez-Beltrán et al. (2021), their Figure 1, and has been constructed using the Vazdekis et al. (2020) spectra.

Rodríguez-Beltrán et al. (2021) attempt to unveil potential secondary populations for a set of galaxies for which archival sbf magnitudes are available in multiple wavelength bands. They unravel secondary stellar populations for 5 of the 9 galaxies in their sample, but point out that the archival sbf magnitudes were measured in a range of works, with potentially inconsistent reduction pipelines. Hence, they stress the importance of consistent sbf measurements in multiple wavelength bands.

This work aims to fill this gap by measuring sbf magnitudes in four wavelength bands for a total of 15 galaxies. We will use the inferred sbf magnitudes in order to compute sbf colors. We will place the sbf colors into the perspective of the framework by Rodríguez-Beltrán et al. (2021), by comparing the yielded sbf colors with the parameter space as presented in that work. Although a direct comparison is not possible due to the different wavelength bands employed, the potential for unraveling stellar population components does become clear.

3 Data

In order to perform a study into stellar populations with the use of sbf, we must select a sample of galaxies for which archival data is available in multiple wavelength bands. Ideally, these observations have been made in wavelength bands for which sbf calibrations have been provided by literature. With that goal in mind, we compare different works that have measured surface brightness fluctuations in one or two bands. By cross-matching the sample of different works who have measured sbf, we retrieve a sample of galaxies for for which observations in multiple bands are available. This allows to finally select a sample of galaxies for which observations have been made in HST's F110W, F160W, F475W, and F850LP bands. Before reaching this sample, we give an overview of different works and the filter bands which they have measured surface brightness fluctuations in to illustrate the process to reaching the final sample.

3.1 Literature observations

The following studies provide sbf calibrations and observations for early type galaxies, and are mainly focused on calibrations for the absolute sbf magnitude - color relation.

- Tonry et al. (2001) measure i-band sbf magnitudes for a large number of early-type galaxies, located uniformly on the sky. The observations were done using various telescopes, and combined into a homogeneous system, leaving a sample of 300 galaxies. These measurements are essentially used to make a measurement of the Hubble-Lemaître constant.

- Jensen et al. (2003) measure the sbf signal in 65 galaxies in the F160W filter, using the Near Infrared Camera and Multi-Object Spectrometer (NICMOS) on the Hubble Space Telescope. The sample exists of early type galaxies, including elliptical and S0 galaxies in a range of environments. The sample exists of a number of galaxies in Virgo and Leo, and the main share of the galaxies are part of the Fornax cluster. They only look at galaxies for which either distances are know from reliable I-band sbf measurements, or from Cepheid variable stars. Their main goal is to better calibrate the F160W sbf measurement as a distance indicator, by looking at the variation of the measurement with stellar population. Compared to a preliminary calibration on a smaller sample by Jensen et al. (2001), they find that the $(V-I)_0 - \overline{M}_{F160W}$ relation cannot be constant, but that a slope exists. Jensen et al. (2003) compare the magnitudes with I-band sbf magnitudes by Tonry et al. (2001). Hence, there is an overlap between these galaxies for which at least V, I and F160W observations have been made.

- Blakeslee et al. (2009) provide new sbf measurements in the z_{850}-band for 43 early-type galaxies in the Fornax cluster. These observations have been made with the F850LP filter

on the Wide Field Channel of the Advanced Camera for Surveys (WFC ACS) on HST. The observations are combined with sbf measurements from Virgo in Mei et al. (2007), also in the F850LP, to create a total sample of 134 galaxies, which allows them to measure Virgo-Fornax relative distances. These galaxies are all within 25 Mpc, so should allow for accurate sbf measurements. Calibrations for this band with $(g_{475} - z_{850})$ colors are available. This means that for this sample of galaxies, observations in both the F475W as well as F850LP have been made.

- Blakeslee et al. (2010) provide a calibration for the HST ACS/F814W band using nine early-type galaxies in the Fornax cluster. The F814W has a significantly higher throughput than the F850LP, indicating a higher efficiency in performing sbf measurements. (Blakeslee et al., 2010) find a tight relation with the F850LP measurements from (Blakeslee et al., 2009), indicating that the uncertainties in both works have been properly estimated, as well as a tight correlation in the magnitude-color relation between the F814W and F850LP filter.

- Jensen et al. (2015) provide calibrations for the distance modulus of F110W (J_{110}) and F160W (H_{160}) bandpasses for the near-infrared channel on the Wide Field Camera 3 (WFC3 / IR) on the Hubble Space Telescope (HST). They sample 16 early-type galaxies for which high quality ACS sbf measurements were already available in z_{850} and $(g_{475} - z_{850})$ colors by Blakeslee et al. (2009). Their sample is not very large but they do allow for an accurate sbf calibration, which is also used in Jensen et al. (2021). For this sample, observations in at least four HST bands are available.

- Cantiello et al. (2018b) sample 89 galaxies from the Next Generation Virgo Cluster Survery (NGVS) and use these to calibrate the sbf distance measurement. They measure the i-band sbf magnitudes from observations with the MegaCam on the Canada-France Hawaii Telescope (CFHT). They calibrate the sbf measurements with u, g and z color combinations. They do not constrain their sample to early type galaxies; they select all galaxies from the sample that are brighter than $B_T \approx 13$ in the Virgo Cluster Catalog of Binggeli et al. (1987). Their sample covers distances out to ~ 32 Mpc.

- Jensen et al. (2021) measure sbf for 63 massive early-type galaxies, also using the WFC3/IR channel on HST. They sample galaxies between 30-100 Mpc and measure $\overline{m}_{110}$, the F110W-band sbf magnitude. They measure these with the main goal to measure the Hubble constant out to large distances. These galaxies are mainly located at distances further out than previous works, and hence do not show any overlap with previous sbf samples.

- Cantiello et al. (2024) create a catalog of sbf distances and a three-dimensional distribution of Galaxies in the Virgo Cluster. To do this they use 278 galaxies in the Virgo cluster. They build further on the sbf calibrations in Cantiello et al. (2018b), and measure sbf distances out to ~ 35 Mpc. Observations from CFHT/MegaCam are used, again following the NGVS.

Besides the usual, large scale surveys into early types and ellipticals that have been conducted, in a more recent effort attention has also gone to using surface brightness fluctuations to determine distance to dwarf galaxies. The following works are targeted at these dwarfs and provide calibrations for various systems and filter bands.

- Cohen et al. (2018) calculate the sbf distance for 23 very low surface brightness galaxies detected in the fields of four nearby galaxy groups (NGC4258, NGC3384/M96, NGC1052, NGC1084), and also measure TRGB methods for this sample. They use HST ACS imaging for their analysis, and they measure distances out to at most 20 Mpc. Their distance estimates are based on the sbf magnitude in the I_{814} filter. Their $\overline{M}_{814}$ calibration is based on the $V_{606} - I_{814}$ colors. This calibration is used later in Van Dokkum et al. (2018) to confirm distance to the dark-matter deficient dwarf NGC1052–DF2.

- Carlsten et al. (2019b) provide an empirical calibration for low-mass systems, using HST sbf measurements from Cohen et al. (2018). Their sample consists of objects with distances

12

below 11 Mpc. A calibration for low-mass-distance relation is given for the CFHT I-band magnitude with $g-i$ color. They also provide the relation between the CFHT systems and the Hubble I_{814} system. In a later work they apply their calibration to characterise satellite system of M101 (Carlsten et al., 2019a). They find that with the CFHT I-band sbf magnitudes, it must be possible to characterise dwarf satellite systems for distances within 20 Mpc.

- Foster et al. (2024) attempt to measure distances to 16 dwarf galaxies in the COSMOS field, using HST ACS images. They combine the I_{814} sbf magnitude with $g-i$ colors to determine the distance. Their sample extends accross the distance range of 17-130 Mpc. They use the calibration by Carlsten et al. (2019b) for $g-i$, and convert this calibration back to HST F475W-F814W color. Their results still show offsets with literature, partly due to the model choices that they have made and the difficulty that arises in measuring the sbf signal for dwarfs.

- Carlsten et al. (2021) have measured sbf magnitudes for potential satellites of 10 Milky Way-like galaxies in the local universe. They provide a calibration for the $\bar{M}_r$, as a large share of their sampled galaxies is only available in the r-band or is significantly deeper in the r-band. Their data mainly comes from CFHT/MegaCam imaging. Their calibration is based on a small subset of satellites for which also i-band sbf magnitudes were available.

- Carlsten et al. (2022) provide sbf measurements for sattelites in the Exploration of Local VolumE Satellites (ELVES) Survey. They determine distances to a large number of potential satellite galaxies to a number of bright hosts in the local universe. Among others with sbf distances, they confirm 338 satellite systems in the local universe. Their observations are done in r and i band in observatories that use sloan-like filters (CFHT/MegaCam, Subaru/HSC, Blanco/DECam, Gemini/GMOS, and Magellan/IMACS). Based on the sbf distance and Signal to Noise, they classify satellite candidates either to be a confirmed satellite, a background contaminant, or unconfirmed.

3.2 Potential filter bands

With the goal of performing sbf measurements in order to learn something about stellar populations, we can infer from the literature a subset of galaxies for which multi-band observations are available. Ideally, we would like to have an as large sample as possible, with consistent measurements in multiple bands. We are not necessarily looking for galaxies that are located at large distances, as opposed to as until yet has been a large motivation in the sample selection (e.g. Tonry et al., 2001; Jensen et al., 2021). Furthermore, the data should be publicly available or alternatively we should be able to obtain the data.

Although the works employing ground based data generally look at large samples and obtain colors in multiple bands (Tonry et al., 2001; Cantiello et al., 2018b; Carlsten et al., 2022; Cantiello et al., 2024), the data that has been used is not (yet) publicly available. Hence, we cannot use these samples in our analysis. On the other hand, space-based data from HST is available at the HST archive. Hence, we cross-match the samples of works employing HST measurements to create a multi-band sample.

Overlapping the data sets by Jensen et al. (2003), Jensen et al. (2015), Blakeslee et al. (2009) and Blakeslee et al. (2010), we find that for a subsample of 26 galaxies from Blakeslee et al. (2009, observations in F475W and F850LP), F160W data is available; either from HST's NICMOS (Jensen et al., 2003) or from WFC3 (Jensen et al., 2015). A more detailed look into the observations learns that especially the large field of view of WFC3 and the detailed calibrations and methodological outline from Jensen et al. (2015), makes the WFC3 observations to be a suitable sample for our multi-band sbf measurements.

Galaxy	Cluster	FCC/VCC	Type	B_T	$m - M$	$g_{475} - z_{850}$	$J - K$
NGC 1399	F	FCC 213	E0	10.6	31.596 ± 0.091	1.490 ± 0.005	0.924 ± 0.023
NGC 1374	F	FCC 147	E0	11.9	31.458 ± 0.070	1.375 ± 0.011	0.894 ± 0.024
IC 2006	F	IC 2006	E1	12.2	31.525 ± 0.086	1.409 ± 0.013	0.919 ± 0.025
NGC 1404	F	FCC 219	E2	10.9	31.526 ± 0.072	1.471 ± 0.006	0.948 ± 0.022
NGC 1344	F	NGC 1340	E5	11.3	31.603 ± 0.068	1.319 ± 0.007	0.862 ± 0.024
NGC 1387	F	FCC 184	S0	12.3	31.430 ± 0.087	1.517 ± 0.011	0.963 ± 0.020
IC 1919	F	FCC 43	dS0	13.5	31.485 ± 0.073	1.163 ± 0.037	0.768 ± 0.090
NGC 4458	V	VCC 1146	E1	12.9	31.063 ± 0.070	1.236 ± 0.049	0.893 ± 0.027
NGC 4472	V	VCC 1226	E2	9.3	31.116 ± 0.075	1.514 ± 0.006	0.883 ± 0.023
NGC 4649	V	VCC1978	E2	9.8	31.082 ± 0.079	1.559 ± 0.014	0.938 ± 0.022
NGC 4489	V	VCC 1321	S0	12.8	30.935 ± 0.069	1.257 ± 0.014	0.878 ± 0.035
IC 3032	V	VCC 33	dE2	14.7	30.886 ± 0.133	1.006 ± 0.030	0.817 ± 0.099
IC 3487	V	VCC 1488	dE6	14.8	31.053 ± 0.134	1.068 ± 0.060	0.837 ± 0.164
IC 3025	V	VCC 21	dS0	14.8	31.421 ± 0.130	0.919 ± 0.074	0.730 ± 0.189
IC 3586	V	VCC 1695	dS0	14.5	31.093 ± 0.080	1.118 ± 0.040	0.801 ± 0.098

Table 1: General galaxy properties of the selected sample. Cluster: The corresponding cluster, F for fornax, V for Virgo. FCC/VCC: The Fornax Cluster Catalog (FCC)designation (Ferguson, 1989) or Virgo Cluster Calatog designation (Binggeli et al., 1985). Type: Morphological type as determined by the ACSVCS (Côté et al., 2004) or the ACSFCS (Jordán et al., 2007). B_T: Total B magnitude from VCC or NED, as reported by Blakeslee et al. (2009) $m - M$: Distance modulus as measured in Blakeslee et al. (2009). $g_{475} - z_{850}$: HST ACS mean galaxy color in the HST ACS/WFC F475W and F850LP bands following Blakeslee et al. (2009). $J - K$: infrared 2MASS color, calculated with magnitudes from the 2MASS archive (Skrutskie et al., 2006).

All galaxies evaluated in Jensen et al. (2015) are cross-matched with Blakeslee et al. (2009), finding that all of the 16 galaxies by Jensen et al. (2015) are also part of the (Blakeslee et al., 2009) sample. We initially sample all these galaxies, for which ACS F850LP, ACS F475W, and WFC3 F110W and F160W images are available. By coincidence, we find an additional galaxy that is part of the Blakeslee et al. (2009) sample for which WFC3 F110W and F160W observations have also been made. This galaxy, NGC 1387, is not part of the Jensen et al. (2015) sample but we do add it to our sample here.

For two of the now in total 17 galaxies, we were not able to measure the sbf signal due to problems in the sbf pipeline. For NGC 1375, the smooth galaxy profile could not be fit using the implemented procedure due to a barred component in the galaxy, while for NGC 1380 a dusty central torus results in similar complications. We have had to discard these observations, which leaves a final sample of 15 galaxies. This sample includes mainly early type galaxies while also holding some bluer dwarf galaxies. The general properties of the galaxies are listed in Table 1.

3.3 Galaxy data

For each of the 15 galaxies in Table 1, we download observations in multiple bands from the HST archive[1]. We download the ACS WFC images in the F475W band and in the F850LP band. All of these observations have either been made for the ACS Virgo Cluster Survey (ACSVCS Côté et al., 2004) or for the ACS Fornax Cluster Survey (ACSFCS Jordán et al., 2007). Both these surveys have collected imaging in the F475W and F850LP bands, with one of the aims of these surveys being to determine accurate distances to the Virgo and Fornax clusters. Mei et al. (2007) have measured F850LP sbf magnitudes for the ACSVCS, which have been combined with similar measurements for the ACSFCS in Blakeslee et al. (2009). While $\overline{m}_{850}$ (the sbf magnitude in the F850LP band) have been measured, the F475W band has only been used to determine the $g_{475} - z_{850}$ color for calibration of the absolute sbf magnitude $\overline{M}_{850}$. This is because the sbf signal is smaller in this band, making the analysis more difficult. This will be one of the first works that

---

[1] https://mast.stsci.edu/portal/Mashup/Clients/Mast/Portal.html

will also measure sbf magnitudes in the F475W.

Next to imaging in the ACS bands, we download the F110W and F160W files from the same archive. These observations have been made with the WFC3 for Jensen et al. (2015), with the goal to provide calibrations for the absolute $\overline{M}_{160}$ and $\overline{M}_{110}$ magnitude. These calibrations have been used later in Jensen et al. (2021) to probe outward to over 100 Mpc, allowing a new measurements of the Hubble-Lemaître constant (Blakeslee et al., 2021). The galaxies in this sample were selected by Jensen et al. (2015) as they populate a broad color range, which would allow an as generally applicable calibration as possible. This broad range is also interesting for the study into stellar population models to learn about the behaviour of sbf colors versus mean colors.

3.3.1   HST image processing stage: drizzled or not

When extracting information from the HST archive, we have the option to download data from various processing stages in the HST processing pipeline. HST images are processed following a pipeline specifically designed for HST in order to convert the raw images into images that can be used for certain science goal. The data from the final processing stage in the HST pipeline have among others been drizzled; multiple exposures have been combined into one frame by identifying cosmic rays and correcting for distortion (Gonzaga et al., 2012). The *drizzle* algorithm was developed by Fruchter & Hook (2002) as a tool specifically for combining HST images.

However, drizzling introduces correlated noise into the resulting data product, which affects the Fourier power spectrum at large wave numbers, as has been shown by Mei et al. (2005a) and Cantiello et al. (2005). This is the reason that instead of using the images from the final processing stage of the HST pipeline, Jensen et al. (2015) and Jensen et al. (2021) use the F160W images from the flat-fielding stage of the pipeline; the files with the `flt` extension. They then combine these images following integer pixel shifts, avoiding the effect of correlated noise.

On the other hand, Mei et al. (2005a) have also shown that the effect of drizzling can be avoided by excluding the highest wave numbers from the fit of the Fourier power spectrum. Following this line of thought, Mei et al. (2007) and Blakeslee et al. (2009) use the drizzeled images for their sbf measurement in the F850LP.

As to stay as close as possible to the analysis by Jensen et al. (2021), we download the images from the flat-fielding stage (the `flt` files) for the F160W filter. We do however find that using this approach results in some complications in our analysis due to undetected cosmic rays. Hence, we also download the fully processed drizzled images for the F160W (the `drz` files), and we will show that the choice of file extension has only little effect on the finally measured sbf magnitude in Section 5.1.1. For the F110W, F850LP and F475W bands, we only download the drizzled images (the `drc` files) for our analysis.

4   Methodology

In the following sections we present the full methodology that has been implemented for measuring the sbf magnitude in multiple wavelength bands. We attempt to stay as close as possible to the most complete implementation of the method as of yet by Jensen et al. (2021) and Jensen et al. (2015), but where necessary we divert from this procedure. Each step will be discussed in detail in the following sub sections. We first present a description of the sbf measurement procedure here as an addition to Section 2.1, by listing all the variables that will be computed within the sbf measurement pipeline. These will eventually allow to measure the sbf flux as represented in Equation 1.5.

We can represent the combined HST image in a given filter band by H_{ij}, where the subscript

indicates that the flux is different at each pixel i, j. H_{ij} has units of $\mathrm{e}^- s^{-1}$. The first step is to estimate the background level B, which we assume uniform over the frame, to obtain the background subtracted image

$$D_{ij} = H_{ij} - B. \tag{4.1}$$

We can then estimate the smooth galaxy profile O_{ij}, which represents the mean surface brightness. Subtracting this smooth model from the data frame D_{ij} yields the residual image

$$R_{ij} = D_{ij} - O_{ij}. \tag{4.2}$$

We have to mask all pixels in the frame that do not contribute to the surface brightness fluctuations. We call this mask M_{ij}, which is equal to 1 for each pixel that contributes to the sbf signal, and 0 otherwise. The mask is a combination of the mask due to bad pixels and cosmic rays ($M_{ij}^{\mathrm{bad\ pix}}$), the mask due to the galaxy model ($M_{ij}^{\mathrm{galmodel}}$), the mask due to fore and background sources (M_{ij}^{source}) and potentially a radial mask that allows measuring the sbf signal in a certain area of the image (M_{ij}^{radial}). Each of these masks is 0 for pixels to be excluded from the sbf calculation and 1 otherwise. The combined mask is the product of these individual masks:

$$M_{ij} = M_{ij}^{\mathrm{bad\ pix}} \cdot M_{ij}^{\mathrm{galmodel}} \cdot M_{ij}^{\mathrm{source}} \cdot M_{ij}^{\mathrm{radial}} \tag{4.3}$$

The normalised and masked residual image, which is the frame for which the one dimensional, azimuthally averaged power spectrum is taken to measure the sbf signal, is then given by

$$I_{ij} = \frac{R_{ij} \cdot M_{ij}}{\sqrt{O_{ij}}}. \tag{4.4}$$

To represent the expectation power $E(k)$, we need to have a representation of the Point Spread Function (PSF). Calling the PSF image PSF, we can represent the expectation power by

$$E(k) = (\mathcal{PS}(PSF) \otimes \mathcal{PS}(M))_r, \tag{4.5}$$

where $\mathcal{PS}$ indicates that we have taken the (radially averaged, denoted by r) Fourier power spectrum and $\otimes$ is the convolution operator.

To illustrate the different sbf processing stages, we show representations of D_{ij}, O_{ij}, R_{ij} and I_{ij} for the F160W image of NGC 1399 in Figure **??**. In Sections 4.1 to 4.7, we will be explaining the steps that were followed to obtain each of the components in Equations 4.1 to 4.5. At the end of each subsection, we will shortly list the components that were computed in those steps.

4.1 Extracting the data

The first step is to process the data that has been downloaded from the HST archive, providing an image cutout of reasonable size for further processing, free of cosmic rays and detector defects. Furthermore we make an initial estimate of the background level and subtract this from the frame. We will further refine this background estimate in Section 4.2 but it does turn out to be useful for an initial background estimate to be made when the method in Section 4.2 fails.

4.1.1 Drizzled frames

There is a difference in the way in which we process the fully processed drizzled frames and the flat fielded `flt` frames. The drizzled frames have already been cleaned of cosmic rays and detector defects by the HST processing pipeline. Each bad pixel is represented by a `nan` value, which means that we do not have to wory about the detector defects and cosmic rays. The only step that needs to be performed is to make a cutout of the frame of suitable size for further processing in the developed sbf pipeline. We have empirically found that a too large frame can cause complications in among others estimating the smooth galaxy profile and furthermore has an exponential effect on

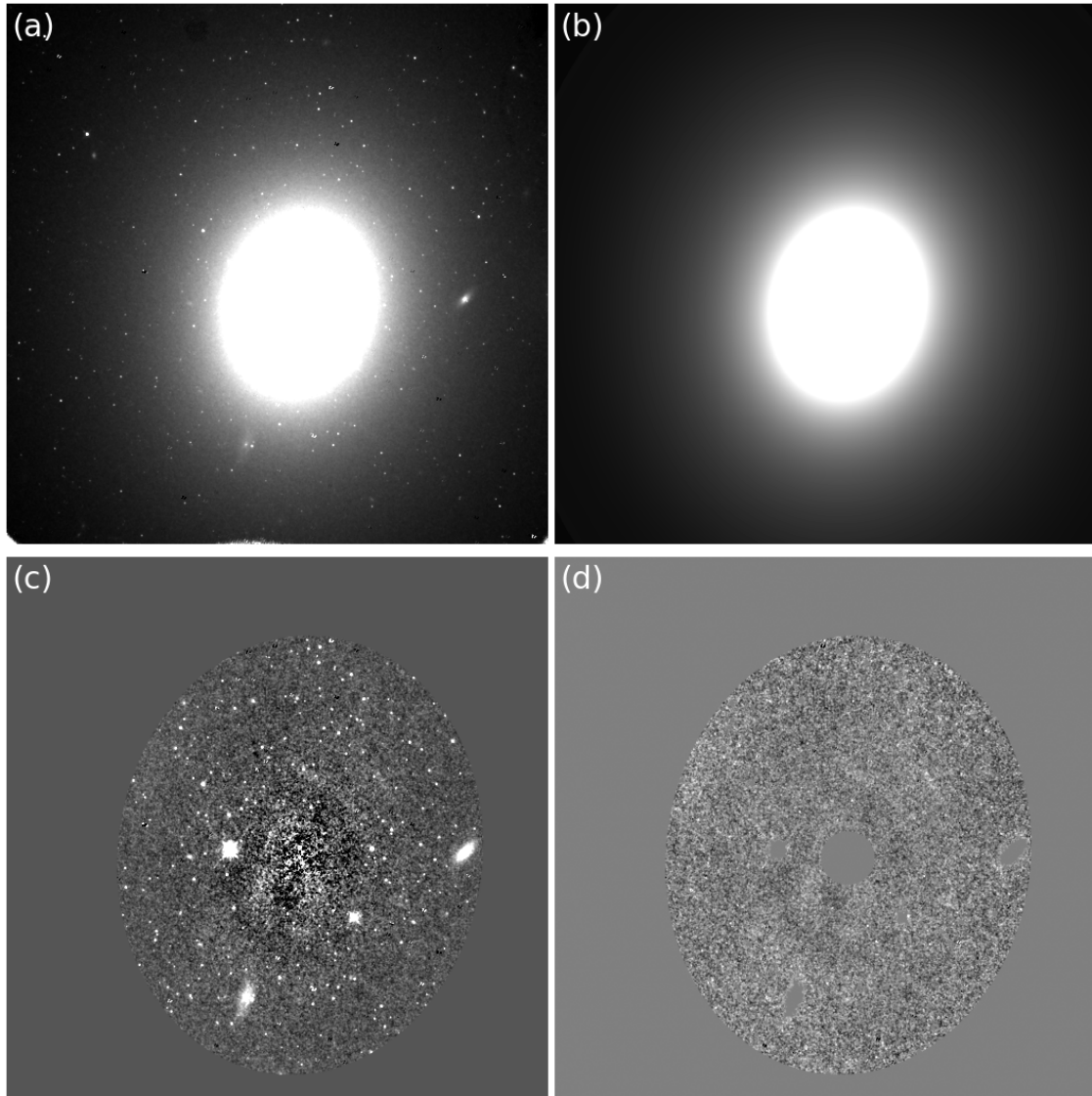Figure 4.1: The different stages in the sbf processing pipeline, illustrated using the F160W image of NGC 1399. (a): The background subtracted image D_{ij}. (b): The smooth galaxy profile O_{ij}. (c): The residual image multiplied by the mask due to the galaxy model, $R_{ij} \cdot M_{ij}^{\mathrm{galmodel}}$. (d): The normalised, masked residual image I_{ij}.

Galaxy	F160W flat-field		F110W drizzled		F160W drizzled		F850LP drizzled		F475W drizzled	
	Size	Exp	Size	Exp	Size	Exp	Size	Exp	Size	Exp
NGC 1399	1008	1196	974	1197	962	1197	1500	1130	1500	680
NGC 1374			1344	1320	1344	1021	1500	1220	1500	760
IC 2006			1152	1320	1152	1021	1500	1220	1500	1440
NGC 1404	1009	1021	1402	1320	1402	1021	1500	1220	1500	760
NGC 1344	1009	1021	1282	1320	1282	1021	1500	1220	1500	760
NGC 1387			600*	527	1500	1329	1500	1220	1500	760
IC 1919	1008	1021	1334	1320	1334	1021	1500	1220	1500	760
NGC 4458			1010	1320	1010	1021	1000	1210	1000	1210
NGC 4472	1009	1021	1336	1320	1336	1021	1500	1210	1500	750
NGC 4649			1310	1320	1310	1021	1500	1210	1500	750
NGC 4489	1008	1021	1068	1320	1068	1021	1500	1210	1500	750
IC 3032			600*	1320	600*	1021	600*	1210	600*	750
IC 3487			500*	1320	400*	1021	600*	1210	600*	750
IC 3025			1270	1320	400*	1021	800*	1210	800*	750
IC 3586	1009	1021	1154	1320	1154	1021	1500	1210	1500	750

Table 2: The frame size and exposure times for each observation in our sample. "Size" corresponds to the frame size in pixels, "Exp" is the total exposure time in seconds. If a size is marked with a star (*), this means that a manual cutout has been made for that frame. If a field is empty, this means that no observation was made in this band.

computation time in each processing stage. This problem is most apparent for the dwarf galaxies in the sample.

Hence, we make a cutout with max width 1500 pix in the original frame, centered on the galaxy. We find the center of the galaxy using the find_galaxy procedure from the mgefit package in python (Cappellari, 2002). This cutout is mainly required dor the ACS images (F850LP and F475W), as the number of pixels in this detector are much larger than for the WFC3. The WFC3 observations have width 1014, which is far below the value of 1500.

For NGC 1378, NGC 4458, IC 3032, IC 3487 and IC 3025 it was required make a manual cutout in the drizzled exposures due to the galaxy being either too faint for find_galaxy to find the center, or due to problems arising later in the fit of the smooth galaxy profile. For these galaxies, we make a manual cutout of smaller frame size. This is expected to have little effect on the finally measured sbf signal, as the areas outside of this cutout will be too faint to measure the sbf signal anyways.

We note that although the size of the WFC3 detector is 1014 pix, the frames are twisted in the drizzled exposures. This leads to a larger frame size for some of the exposures.

For each of the frames, we also compute the first mask that is due to detector effects and cosmic rays, represented by $M_{ij}^{\mathrm{bad\ pix}}$. This mask is given by a frame that is equal to one everywhere, and zero at the pixels that are nan values.

The frame size and exposure time for each observation are listed in Table 2.

4.1.2 Flat-fielded frames

The flat-fielded frames are not yet cleaned of cosmic rays and detector defects, and still need to be combined into one combined image. The observations are typically made up of 5 individual exposures, that are pointed at the galaxy with slight offsets.

For each of the frames, we identify cosmic rays with the `lacosmic` algorithm, which identifies cosmic rays with a framework based on Laplacian Edge Detection (Van Dokkum, 2001). This algorithm iterates over the frame and identifies outliers based on the sharpness of the pixel edge. These pixels are marked as cosmic rays. Hence, for each individual exposure this results in a mask of cosmic ray pixels.

We then combine the individual exposures following integer pixel shifts, as proposed by Jensen et al. (2021). This results a slight decrease in resolution, but also makes sure that the background detector noise is not correlated. This is mainly advantageous for the fit of Equation 2.1 in Fourier space as correlated noise in the drizzled frames causes a decrease in the Fourier power spectrum at large wave numbers (Mei et al., 2005a; Cantiello et al., 2005).

The shifts required for the individual frames to be overlayed is calculated using the pixel world coordinate system (WCS, e.g. Greisen et al., 2006), for which we use `astropy.wcs` in python. Starting with the first frame, we identify the coordinates of the central pixel using WCS. We then identify the pixel corresponding to that coordinate in the next frame, which we use to calculate the shift required for the frames to be overlapped. WCS returns the pixel coordinate of the second frame as a decimal number. We round this to an integer as to obtain the integer shift required for the frames to be overlapped. Evidently, the shift results in some pixels at the borders to fall outside of the original frame. We discard all those pixels that do not have observations in both frames.

The frames are combined by summing the individual exposures, weighted by the exposure time of each individual frame. After two frames have been combined, we combine the next frame with the combined image following the same procedure, until all frames have been combined. We finally divide the combined exposure by the total exposure time of all frames, to yield the flux in $e^- s^{-1}$. Finally, we make a final cutout to retrieve a square frame, as is required for the Fourier analysis in Section 4.7.

The individual cosmic ray masks are combined following the same integer pixel shifts as the individual exposures. If a pixel is identified as cosmic ray in at least one of the individual frames, that pixel is disposed in all of the frames. This in the same way results in a final bad pixel mask $M_{ij}^{\text{bad pix}}$. H_{ij} in Equation 4.1 is then represented by the combined image.

4.1.3   Initial background estimate

Similar to Jensen et al. (2021), we make an initial estimate of the background level for each of the galaxies in our sample by estimating the background value in the corner of the combined image H_{ij}. Jensen et al. (2021) as well as Jensen et al. (2015) and Goullaud et al. (2018) do not elaborate deeply on how this estimate is made, except for the value being estimated from the corners of the image. Hence, we apply the following procedure.

For each extracted frame H_{ij}, we make square cutouts of width 5 pixels in the corner of the image. For each of these four cutouts, we find the median intensity of the unmasked pixels in the frame. We take the median intensity instead of the mean, as this will account for outliers such as stars or other sources. The initial background estimate is then calculated as the mean of the four median background values, weighted by the number of unmasked pixels in that corner. This yields an initial background estimate B_0 which we subtract from the data image H_{ij}.

Although this initial background estimate is not very refined and does not more than once lead to (very) inaccurate initial estimates of the background level, this almost always gets corrected by the final background estimation procedure as described in Section 4.2. Although we could have opted to leave this step out of the pipeline, we do find that for some galaxies the procedure as in 4.2 fails for various reasons. In those cases we can use the initial background level B_0 as the background estimate. For galaxies for which the improper background estimate leads to problems in the final

background estimation procedure in Section 4.2, we do provide the option to not estimate the initial background estimate B_0 when running the sbf pipeline.

4.2 Background level estimation

When extracting the data into one image, an initial estimate B_0 has already been made of the background level by estimating the background from the intensity in the corners of the image. We further refine this estimate and assign an uncertainty to this value, by performing a Sérsic fit to the galaxy profile, superimposed with a background level. This method is comparable to the method performed by Jensen et al. (2021), who fit an $r^{1/4}$ profile to the outer isophotes, although with some modifications. In general, we perform a number of iterations in which the a Sérsic model with a constant background component is fit to the image, until it converges.

The procedure is as follows:

1. For each galaxy, we find the coordinates of the center of the galaxy by using the `find_galaxy` procedure from the `mgefit` package (Cappellari, 2002). This method has turned out to be very efficient in estimating the galaxy center, which is why it is used in this work as opposed to other tools that can be employed for the same cause.

2. At each iteration step i, elliptical isophotes are fit to the image using the `ellipse` tool from the `photutils` package (Bradley et al., 2020) (a further elaboration on `ellipse` within `photutils` can be found in Section 4.3.3).

3. A one-dimensional brightness profile is made from the intensity as a function of semi-major-axis length.

4. The isophotal intensities of the one-dimensional profile are fit to a Sérsic model, superimposed with a background level. This combined equation is given by

$$I_i(r) = I_{Sérsic,i}(r) + B_i,\qquad(4.6)$$

where B_i is the background level at iteration step i and $I_{Sérsic}(r)$ is the Sérsic profile given by (Sérsic, 1963, 1968)

$$I_{Sérsic}(r) = I_e \exp\left\{-b_n\left[\left(\frac{r}{r_e}\right)^{\frac{1}{n}} - 1\right]\right\}.\qquad(4.7)$$

$I_{Sérsic}(r)$ represents the intensity at radius r from the center of the galaxy, n is the Sérsic index, r_e is the so-called effective radius and I_e is the intensity at the effective radius. b_n is a constant defined such that r_e contains half of the light profile, and can be approximated by $b_n \approx 2n - 0.33$ (e.g. Graham & Driver, 2005).

When fitting the one dimensional profile, n, r_e, I_e and B_i are the free parameters to be fit. Fitting using the `curve_fit` procedure from `scipy` yields best fit parameters $\hat{n}$, $\hat{r_e}$, $\hat{I_e}$ and $\hat{B_i}$.

5. The background level $\hat{B_i}$ estimated in the previous step is subtracted from the data, giving the intensity for the next iteration step

$$I_{i+1}(r) = I_i(r) - \hat{B_i}.$$

6. The total background at iteration step i can then be estimated as the sum of the estimated background level at each iteration step:

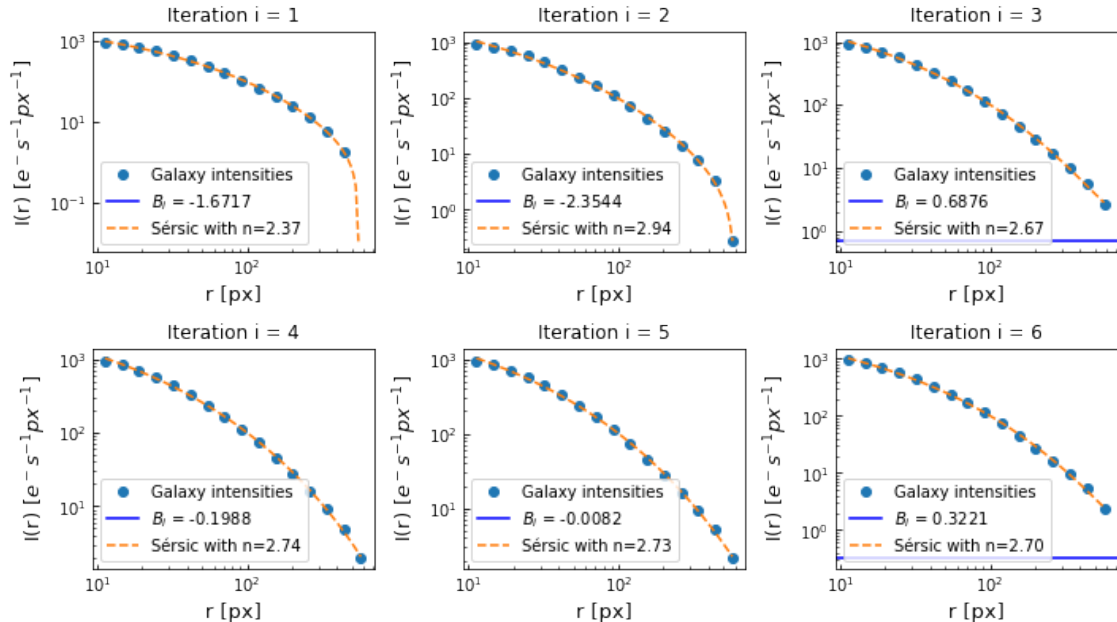$$B_{[i,\ total]} = \sum_{j=0}^{i} \hat{B_j}\qquad(4.8)$$

Figure 4.2: First six fits of the Sérsic profile superimposed by a background level per iteration number for NGC 1399 in F110W. Note that the x-axis as well as the y-axis are in log-scale. The radius is the radius from the center of the galaxy, the intensities are those as have been measured by the `ellipse` function.

7. Steps 2 to 6 are repeated a fixed number of iteration steps N. As the estimated background level gets subtracted from the data at each iteration step i, the background value eventually converges, such that the fitted value $\hat{B}_i$ in each iteration step gets close to 0. In practice, it turns out that the level converges and the B_i start to oscillate around 0.

In order to assess the uncertainty in the total background level, we estimate the background level as the average of the total background level at the last n_b iteration steps. This is given by

$$B_{final}(N, n_b) = \frac{1}{n_b} \sum_{i=N-n_b}^{N} B_{[i,\ total]}.\tag{4.9}$$

Similarly, the uncertainty is estimated as the standard deviation of the last n_b iteration steps;

$$\sigma_B(N, n_b) = \sqrt{\sum_{i=N-n_b}^{N} \left(B_{[i,total]} - B_{final}(N, n_b)\right)^2}.\tag{4.10}$$

As to illustrate fitting procedure, the Sérsic + background fit for the first 6 iteration steps is shown in Figure 4.2 for NGC 1399 in the F110W. The development of the total noise as a function of iteration step is shown in the left frame of Figure 4.3.

4.2.1 Determine N and n_b

A challenge in the background estimation procedure outlined in Section 4.2, is to determine the values of N and n_b that will consistently yield a robust estimate of the background and its uncertainty, given that we apply the method to a large set of galaxies. We would like to have as many iteration steps as possible, as well as an as large possible value for n_b to gain a statistically large enough value to estimate σ_b from. On the other hand, we are (slightly) limited by computation time, the `ellipse` procedure is not a very quick method. For the HST ACS frames (F475W and F850LP) that have larger image sizes than WFC3, the computation per iteration step can go up
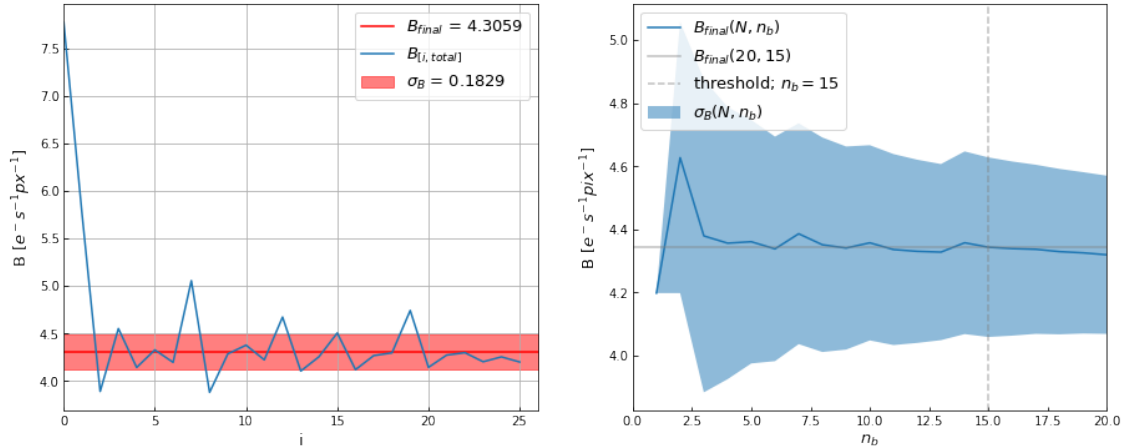
Figure 4.3: Left: development of background per iteration step for NGC 1399 in F110W. In red, the final estimated background level together with its estimated standard deviation is plot. Right: The development of $B_{final}(N, n_b)$ and $\sigma_B(N, n_b)$ as a function of the number of included background estimation iteration steps n_b. Here the total number of iteration steps N is equal to $N = n_b + 5$, i.e. the first 5 iteration steps are excluded from the background level estimate.

to two minutes. Ideally, one would like to determine some stopping criterion, dependent on the change in B_{final} and σ_B, given each additional iteration step, and stop the algorithm when this change gets below some threshold. However, declaring a robust stopping criterion turns out to be rather challenging, as this criterion would need to take into account B_{final}, σ_B, N and n_b, and additionally a threshold would be required, which would be another free parameter that would need to be set.

Since the effect of the background on the final measured SBF amplitude is relatively small compared to the uncertainties arising from other components (as we will see in Section 4.8, Table 5), we decide to simply choose values for N and n_b that seem appropriate for our goal. To assess the quality of the choice, some tests are conducted that show the behavior of B_{final} and σ_B for different N and n_b.

In the left frame of Figure 4.3, we shown the development of $B_{[i,\ total]}$ as a function of iteration step N for NGC 1399 in the F110W band. We can see that the total background level converges relatively quickly. After about 3 iteration steps, the algorithm already seems to have converged and oscillates around some value. This behavior is similar when we apply the algorithm to other galaxies (for which the Figures are available in Appendix A.1). This justifies the relatively conservative assumption to use the B_i for $i > 5$ in order to determine B_{final} and σ_B.

The next challenge is to determine how large N must be in order for n_B to be sufficiently large to get a stable estimate for the standard deviation. Therefore, we show B_{final} and σ_B as a function of n_b in the right frame of Figure 4.3, where we include all $n_b = N - 5$ when we calculate the background. We can see that B_{final} as well as σ_B seem to stabilise. Comparing this plot over various galaxies (see Appendix A.1), we decide to choose a value of $n_b = 15$ to calculate the background level. This seems a robust value and leaves enough iterations such that outliers in $B_{[i,\ total]}$ will not significantly affect the result. This leaves the final values of $N = 20$ and $n_b = 15$, which are used in the remainder of the paper to estimate the background level.
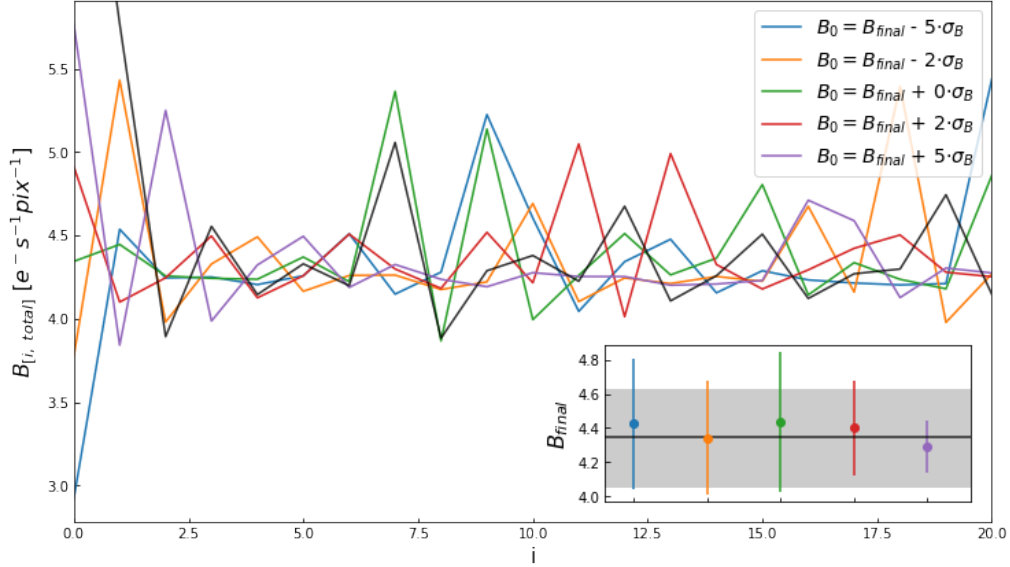
Figure 4.4: Development of the background $B_{[i,\ total]}$ as a function of iteration step i for NGC 1399 with various initial background estimates B_0, equal to the final background level, plus and minus 3 and 6 times the standard deviation. The different colors correspond to the different runs of the algorithm; the dark curve shows the original algorithm run as in Figure 4.3. The inset frame shows the output B_{final} with the uncertainty σ_B for each different run, compared with that from the original run in grey.

4.2.2 Methodological Robustness

As to check whether the background estimation is robust in the sense that given the input B_0, the algorithm converges to the same final background level with similar uncertainty, we run the algorithm for different initial background estimates B_0. Figure 4.4 shows the background development $B_{[i,\ total]}$ for NGC 1399, where for each run, a different value of B_0 was used. The algorithm is run with B_0 equal to the true background level, and B_0 equal to the true background level plus or minus 3 and 6 times the standard deviation of the background level. For reference, the background level as in the left frame of Figure 4.3 is also shown. The inset frame shows the output B_{final} with the uncertainty for each different run, compared with the background level and uncertainty of the original run in grey. As before, we show the consistency of this graph with different galaxies in Appendix A.1.

We can see that the runs all converge to approximately the same background level, given the original uncertainty. There is some slight difference in the uncertainty of each individual run. One of the reasons might be that there are numerical artifacts in how the elliptical isophotes are fitted using the `ellipse` tool, such as the way in which the galaxy center is calculated or how sigma clipping is applied to mask out bright objects. In general, the B_{final} from the black curve seems a good approximation for the background level and its uncertainty.

We substitute the value B_{final} into B in Equation 4.1, in order to obtain the data-subtracted image D_{ij}

4.3 Modelling the galaxy surface brightness profile

Galaxy modelling is an important step in the measurement of the sbf signal as the sbf amplitude is a function of the galaxy light profile. Hence, when we inaccurately model the galaxy brightness profile, the SBF measurement will be offset. This subsection explores the importance of the smooth galaxy model, gives a short overview about how the smooth model has been estimated in previous

works, and gives an outline of how the estimate of the smooth model is eventually implemented within this work.

4.3.1   Literature

In literature, most works measure the smooth galaxy profile by fitting elliptical isophotes to the galaxy image. Blakeslee et al. (2021) and Jensen et al. (2021) do this by using a galaxy modelling tool specifically developed for measuring surface brightness fluctuations, called ELLIPROF (Tonry et al., 1997; Jordán et al., 2004). Some works have experimented with using alternative methods (e.g. Foster et al., 2024), and some attempt their own approach (Carlsten et al., 2022).

It is important to note that in essentially all works, modelling the smooth galaxy profile is an iterative procedure between estimating the smooth galaxy profile, and modelling background sources. In general, the smooth profile is modeled initially, and subtracted from the image. In the residual image, fore- and background sources then are identified and masked. In the masked image, the smooth model image then is re-fit, being free from contaminating sources.

We will briefly discuss the modelling procedure for various works here.

- Jensen et al. (2021) use the galaxy modelling procedure that is thoroughly explained in the work of Goullaud et al. (2018). An interesting component in this work is that they fit the smooth galaxy model in an iterative manner in order to attempt to also estimate the background level. They use the ELLIPROF tool, which is described by Goullaud et al. (2018) as a fitting routine that fits elliptical annuli to a galaxy. However, documentation about this tool is rather sparse; the original papers by Tonry et al. (1997) and Jordán et al. (2004) only briefly discuss the tool and the tool cannot be found online.

  With a surface brightness profile fit, the background level is estimated by fitting an $r^{1/4}$ profile (which is a Sérsic fit with index $n = 4$, see Equation 4.7). This is done iteratively, finding a new background level, inserting that into the image, regenerating the isophotal model, and so on until residuals are minimised (Goullaud et al., 2018).

  They mention that for some galaxies the $r^{1/4}$ was not accurate, and they model the background as well by comparing to 2MASS J-band photometry. The idea is that when a profile does not follow $r^{1/4}$, they look at the same galaxy through 2MASS (which has a much larger field of view) and hence they can correct the profile to match the 2MASS profile; these tend to correspond with each other, and because of the larger field of view the 2MASS background can be more accurately estimated.

  The Galaxy profile is then once more modeled using ELLIPROF to obtain a final residual. Potentially, if there are more overlapping bright companion galaxies these are iteratively and independently fit. These galaxy models are then stored as the "final" galaxy model. If there still turn out to be large residuals, a bicubic spline model is applied to take these away, and this is accounted for by excluding the lowest wave numbers in the SBF fit.

- Carlsten et al. (2022) use the method as outlined more detailed in Carlsten et al. (2020). Instead of using a non-parametric approach in which elliptical isophotes are fit as a function of radius, they fit more simple Sérsic profiles using imfit (Erwin, 2015). Since Carlsten et al. (2022) are mainly focused on measuring the sbf signal for dwarf galaxies, they revert to imfit, even though this method does generally lead to remaining structures in the residual image.

- Foster et al. (2024) explore three different methods for the smooth galaxy model fit. They attempt fitting a Sérsic profile, a bicubic spline model, and a smoothed image model with a Gaussian kernel. In the end, they find the best results by using the Gaussian smoothed

image model.

In their discussion, they mention that both the bicubic spline model as well as the `imfit` Sérsic fit leave too much residual structure in the galaxy-subtracted image. They mention that the smoothed image model leaves the lowest amount of residual variance, and hence they decide to use that model for the analysis.

4.3.2 Model differences

In modelling the smooth surface brightness profile, we have attempted a number of different methodologies, exploring the range of available options.

One of the attempts has been the use of `imfit` (Erwin, 2015), which allows fitting a Sérsic profile to the galaxy. This method works, but only allows one orientation of the model. It has shown that for some galaxies, this is not a good approximation, as the orientation of the isophotes towards larger radii of the galaxy might be changing. Eventually, this leads to remaining structures in the residual image R_{ij}.

Another attempt has been to apply a Multi-Gaussian Expansion (MGE) to the galaxy model. In this method multiple Gaussians are fit to the image, aiming to optimally represent the smooth galaxy profile while also allowing multi-component structures to be fit that might be missed by elliptical modelling tools. Cappellari (2002) provide a python implementation called `mgefit`, allowing both variation in the orientation of the Gaussian ellipses as well as the option to keep the Gaussians in a fixed position. While estimating the smooth model, the tool calculates the optimal number of Gaussians to be fit. In attempting this tool, we have found significant residual structures to be remaining in the residual image.

Although we would have liked to attempt the use of the `ELLIPROF` procedure as used by among others Jensen et al. (2021), Jensen et al. (2015) and Blakeslee et al. (2009), this software is not publicly available. Therefore, we revert to the use of the `ellipse` tool. This method from the `photutils` package in python (Bradley et al., 2020) iteratively fits elliptical isophotes following the procedure by Jedrzejewski (1987). Ellipses are fit to the galaxy's isophotes, keeping a fixed semi-major axis length. According to Goullaud et al. (2018), `ellipse` works similarly to `ELLIPROF`, with the difference that `ellipse` does not allow extrapolation of the smooth model beyond the outer isophote. This does lead to a strict border in the model-subtracted image.

As to keep as close to the sbf measurement procedure by Jensen et al. (2021), Jensen et al. (2015) and Blakeslee et al. (2009), we finally decide to use the `ellipse` tool. This method leads to the most smooth residual images leaving least residual structure.

4.3.3 Implementation

The `ellipse` tool has a number of parameters that can be adjusted, including the center of the ellipse to be fit, the spacing between the subsequent ellipses, and the fraction of pixels in an elliptical isophote that need to be non-masked before an isophote can be fit. The tool allows sigma-clipping, and furthermore an estimate for the center of the galaxy needs to be input, as `ellipse` does not allow for a procedure to estimate the galaxy center.

As to find the galaxy center, we use the `find_galaxy` procedure from the `mgefit` package, similar to what was done in Section 4.2. We complete in total two runs to estimate the smooth galaxy model. In the first run, we allow sigma clipping, leading to bright fore and background sources not being included in the model fit. This run is made with a moderate isophote spacing, and excluding the fit of higher order terms, which could reveal "boxy" or "disky" shapes. This model is then subtracted from the galaxy after which we use the procedure outlined in Section 4.4 to

mask stars and other fore- and background sources.

We then lay this mask over the original background-subtracted data image, and re-run the `ellipse` model. This prevents the ellipse tool from being influenced by external sources. In this last run of the model, we run with a smaller isophote spacing, and we do include the higher order harmonics in the model build. This takes slightly longer to compute but does lead to a more complete model fit. This finally yields the smooth surface brightness model O_{ij} that is used to create the residual image R_{ij}.

We also use the model to create a mask due to the galaxy model. In line with Jensen et al. (2021), we only measure the sbf amplitude in the area where the smooth galaxy profile contributes 60% of the flux. This means that we only select the pixels for which $O_{ij} \geq 1.5B$. This works well for the elliptical galaxies in our sample. For the dwarfs, we briefly reduce this threshold, and set it to 30%. This still allows to properly measure the sbf signal, although yielding slightly more uncertainty. The mask due to this threshold is indicated by $M_{ij}^{\mathrm{galmodel}}$ in Equation 4.3.

4.3.3.1 Model boundary

When building the galaxy model using `photutils`, the tool prevents from building ellipses for which the isophote falls outside of the image frame. This leads to ineffective results, as for many galaxies the galaxy stretches outside of the frame, hence leading to valuable information being missed.

As to allow the tool to build the model further than the image frame, we slightly modify the source code of the function `buildEllipseModel` from the `photutils` package. By allowing the larger frame size, we are able to also model more extended galaxies.

4.3.3.2 Central source mask

When extracting the mask of background sources following the procedure in Section 4.4, often the central area of a galaxy is returned as being masked, as this is generally the area in the galaxy where the `ellipse` model leaves the most residual structure. However, if this area is masked, `ellipse` will not be able to fit the elliptical isophotes as it cannot detect the central brightness. Hence, as to de-mask the central area of the galaxy, we implement the following short procedure.

We take the segmentation map that is extracted from SExtractor, and identify all sources that fall within 10 pix of the center of the image. We then un-mask all these sources. This does not only lead to the central sphere of width 10 pix to be free from masking, but also leads to all sources that have any component within this central sphere to be unmasked. Empirically, we find that this is sufficient for the `ellipse` tool to be able to fit the second smooth brightness profile.

4.4 Masking external sources

The next step that needs to be performed in measuring the SBF signal is to mask fore and background sources in the residual image that are not part of the intrinsic surface brightness fluctuations such as foreground stars, background galaxies and globular clusters. In order to identify such sources a number of tools are available, but the most widely used tool is SExtractor (Bertin & Arnouts, 1996). The software allows identification, deblending, measurement and classification of sources in astronomical images. By inserting an astronomical image, a catalogue of sources in that image is returned, including among others position, magnitude and orientation for each source. A segmentation map, indicating the pixels belonging to each source in the frame is also provided. Especially the segmentation map and object fluxes are very relevant for the cause of measuring surface brightness fluctuations.

By utilising SExtractor, we follow a long tradition of other works that have used SExtractor to identify sources for SBF measurements (e.g. Jordán et al., 2004; Biscardi et al., 2008; Jensen et al., 2015; Cohen et al., 2018; Carlsten et al., 2022). As to keep the full SBF measurement pipeline within python and maintain a flexible algorithm, we use the python implementation for SExtractor called `sep`, which provides the core SExtractor algorithm within a python environment (Barbary, 2016).

4.4.1 SExtractor noise model

In order to identify sources from the inserted astronomical image, SExtractor first estimates the background level, uses this background as a measure for uncertainty in each pixel, and this uncertainty then is then used to define the threshold above which a source will be identified. The (non-uniform) background level is estimated by passing the image with a grid, estimating the background at each position, and finally fitting a bicubic spline model to obtain the background image. This background image is then subtracted from the inserted image. The subtracted background then becomes part of the uncertainty used for identifying astronomical objects in the background-subtracted image. In the previous section, we have subtracted the galaxy model from the original data image. We must take take this into account when identifying sources, in order to prevent SExtractor from identifying surface brightness fluctuations in the central area of the galaxy as point sources, while also not missing out on more faint objects in the outer edges (e.g. Jensen et al., 2021; Jordán et al., 2004).

The exact ways in which various works have included the subtracted galaxy when identifying point sources varies, but most include the galaxy model into the SExtractor weight image by adding the galaxy model multiplied by a constant, to the `rms` image (Cantiello et al., 2005; Jensen et al., 2021). The `rms` image is an image representative of the uncertainty for each pixel. Jordán et al. (2004) provide an even more extended and complete explanation of how to include the noise components that make up the residual image, including the exposure time, instrumental variance, and galaxy model. However, since in most works, the exact choice of threshold is either not listed (e.g. Biscardi et al., 2008), or empirically determined (e.g. Jensen et al., 2021), we decide to revert to an empirical approach as well.

As to give SExtractor the correct weight map, we first estimate the background using SExtractor, with a grid-size dependent on the Sextractor run. The uncertainty due to background subtraction is then assumed to be constant for the whole image. The uncertainty due to the subtracted galaxy model is then incorporated into SExtractor by adding the galaxy model squared to the `rms` map. This is different from works in literature, and does lead to a rather awkard choice of the detection threshold, but it does lead to sources being identified appropriately in the center of a galaxy as well as in the outskirts with an individual run.

4.4.2 Choice of SExtractor parameters

For those who have worked with SExtractor, the broad availability of parameters that can be adjusted to allow tweaking of the algorithm in order to achieve a desired outcome is well known. Although this possibility to adjust the algorithm can be very useful for specific science goals, the disadvantage is that the algorithm can become very fragile when the incorrect input parameters are chosen. Furthermore, finding the input parameters that lead to accurately identifying fore- and background sources without masking the surface brightness fluctuations themselves turns out to be a challenge.

Following the outline by (Jensen et al., 2021) we first identify bright foreground sources and saturated stars that might lead SExtractor to not identify fainter sources initially. Also, this masks areas that retain residual structure due to incorrect subtraction of the galaxy model. These

Filter	file type	Run	Thresh.	Invert	Frame size	Min pix	Max pix	Scale gal
F160W	flt	1	0.5	True	256	50	None	True
		2	5	True	256	1	4	False
		3	0.5	False	64	5	None	True
F160W	drz	1	0.5	True	256	50	None	True
		2	0.5	False	64	5	None	True
F475W	drc	1	0.1	True	256	100	None	True
		2	0.1	False	64	5	None	True
F850LP	drc	1	0.2	True	256	100	None	True
		2	0.2	False	64	5	None	True

Table 3: Parameters used in the different SExtractor runs to identify background sources. *Thresh.* corresponds to the detection threshold, *Invert* shows whether the algorithm was run on the inverse image, *Frame size* is the width of the grid used to determine the SExtractor background in pix, *Min pix* and *Max pix* correspond to the minimum and maximum pixel size that objects must have for them to be detected, *Scale gal* indicates whether the subtracted galaxy model has been taken into account in the SExtractor `rms` image.

areas are not suitable for measurement of the SBF signal, so in this way these areas are directly removed. The algorithm is run with a relatively large frame size, a large minimal number of pixels, and a threshold similar to the final run. The algorithm using these parameters is also run on the inverse image in order to identify areas for which galaxy model subtraction had lead to significant negative residuals.

For the algorithm run on the flat-fielded frames, we also perform an additional preliminary run with parameters that allow detection of extreme outliers such as bad pixels or cosmic rays that had not been detected by `lacosmic`. This is done with a large threshold and pixel size smaller than the detection threshold for the final run, meaning that no sources will be removed in this stage that would otherwise be identified as point sources. In this stage the algorithm is also run on the inverse image to detect negative outliers.

For the final run, the algorithm is run with default minimum pixel size, moderate frame width, and an empirically determined thresholds for each filter band. This yields a final catalog of extracted sources. The SExtractor parameters used in each filter band and each run are listed in Table 3.

4.4.3 Masking extracted sources

For the first run (and the second for the flat-fielded images), a mask is created from the SExtractor segmentation map, masking all non-zero pixels in the segmentation map. The masked image is then inserted into the next Sextractor run, which prevents the extended sources from being identificated twice, and prevents those sources to be part of the final source catalog. For the final run in each band, the sources are not directly masked from the segmentation map. The catalog of identified sources is first used to estimate the combined globular cluster and background galaxy luminosity function. From this luminosity function, a detection limit m_{cut} is retrieved, and only the sources that fall within the detection limit are masked. This yields the source mask M_{ij}^{source}. For the sources fainter than the detection limit, the residual power left in the image due to unmasked sources is estimated following the outline in Section 4.5.

4.5 Estimate residual power

The measured sbf power P_0 must be corrected for undetected globular clusters and background galaxies. This is usually done by fitting a Gaussian globular cluster luminosity function (GCLF) combined with a power law for the background galaxies to the catalog of extracted sources (Cantiello & Blakeslee, 2023). Following the outline by Mei et al. (2005b), the residual power

from unmasked sources is calculated as follows.

Following the notation by Cantiello & Blakeslee (2023), the measured power in a galaxy net residual image can be written as

$$P_0 = P_f + P_r. \tag{4.11}$$

P_f is the power coming from the surface brightness fluctuations, which is of our interest, and P_r is the power coming from the unmasked sources. The flux coming from these sources can be subdivided into the globular cluster component σ_{gc}^2 and the background galaxy component σ_{bg}^2, and is given by

$$P_r = \frac{\sigma_{\mathrm{gc}}^2 + \sigma_{\mathrm{bg}}^2}{\langle O_{ij} \rangle}. \tag{4.12}$$

The normalisation by the mean galaxy flux is required as to scale P_r with P_0. The sources are detected in the galaxy-subtracted image, as P_0 is measured after scaling the residual image with the galaxy model (Equation 4.4). Hence, P_r must also be scaled with the mean galaxy flux within the galaxy field. The first of the individual components can be represented by the galactic cluster luminosity function, which describes the number count of sources as a function of magnitude following a Gaussian distribution. This luminosity function is given by

$$N_{\mathrm{gc}}(m) = \frac{N_{\mathrm{gc}}^0}{\sqrt{2\pi}\sigma} \exp\left[\frac{-(m - m_{\mathrm{peak}}^{\mathrm{gc}})^2}{2\sigma^2}\right], \tag{4.13}$$

with $m_{\mathrm{peak}}^{\mathrm{gc}}$ the apparent peak GCLF flux which is dependent on distance to the galaxy. Although calibrations are available for the absolute peak GCLF flux (e.g. Nantais et al., 2006; Jensen et al., 2015), we decide to keep $m_{\mathrm{peak}}^{\mathrm{gc}}$ a free parameter in the combined luminosity function fit, as proposed by Mei et al. (2005b) and Jensen et al. (2015). We do fix the width of the distribution σ. Jensen et al. (2021) keep the width as a free parameter between $\sigma = 1.2$ mag and $\sigma = 1.4$ mag, Jensen et al. (2015) keep σ fixed at 1.2 mag, and Mei et al. (2005b) adapt a value of 1.35 mag for the Virgo cluster. As to keep the value as close as possible to the reference values in Jensen et al. (2015), we decide to also a width of $\sigma = 1.2$ mag for all filter bands.

The background galaxy count as a function of luminosity can be represented by a power law and is given by

$$N_{\mathrm{bg}}(m) = N_{\mathrm{bg}}^0 10^{\gamma m}. \tag{4.14}$$

The power law follows a different slope γ in each band. For the F475W, we can use the ACS WFC faint galaxy counts by (Benítez et al., 2004) and use a value of $\gamma = 0.32$. For the F850LP, (Mei et al., 2005b) use a value of $\gamma = 0.35$, which we also adapt. For the F110W and F160W, a value of $\gamma = 0.25$ is used (Jensen et al., 2015).

The total number count of identified sources as a function of magnitude then is simply a sum of the globular cluster and background galaxy component:

$$N_{\mathrm{tot}}(m) = N_{\mathrm{gc}}(m) + N_{\mathrm{bg}}(m). \tag{4.15}$$

Using the catalog of extracted sources generated with SExtractor, we can make a histogram of the source counts in each magnitude bin and use that to fit the combined luminosity function N_{tot}. A detailed explanation of the fitting procedure is given in Section 4.5.1. Given the fitted combined luminosity function, we yield a completeness limit m_{cut}, which is the limiting magnitude above which the catalog of extracted sources is incomplete. From the segmentation map extracted from SExtractor, we mask all sources with fluxes larger than the completeness limit and use that as the final source mask M_{ij}^{source}.

	F110W	F160W	F850LP	F475W
m_0	26.8223	25.9463	24.862	26.068

Table 4: AB Zero-point magnitudes for each filter system. Zero-points for the ACS bands come from Sirianni et al. (2005), for the WFC3 bands come from Jensen et al. (2015)

The residual power coming from sources fainter than the completeness limit then can be represented by the globular cluster component

$$\sigma_{\mathrm{gc}}^2 = \frac{1}{2} N_{\mathrm{gc}}^0 10^{0.8\left[m_0 - m_{\mathrm{peak}}^{\mathrm{gc}} + 0.4\sigma^2 \ln(10)\right]} \cdot \mathrm{erfc}\left[\frac{m_{cut} - m_{\mathrm{peak}}^{\mathrm{gc}} + 0.8\sigma^2 \ln(10)}{\sqrt{2}\sigma}\right] \tag{4.16}$$

and the background galaxy component

$$\sigma_{\mathrm{bg}}^2 = \frac{N_{\mathrm{bg}}^0}{(0.8 - \gamma)\ln(10)} 10^{0.8(m_1 - m_{\mathrm{cut}}) + \gamma(m_{\mathrm{cut}})}, \tag{4.17}$$

where m_0 in Equation 4.16 is the photometric zero point flux, given for each filter band in 4, and erfc() is the complement of the error function (Blakeslee & Tonry, 1995). σ_{gc}^2 and σ_{bg}^2 then are combined as in Equation 4.12 to yield the total residual power from unmasked sources.

When performing the fit of the combined globular cluster and background galaxy luminosity function as in Equation 4.15, we fix σ and γ, and consider $m_{\mathrm{peak}}^{\mathrm{gc}}$, N_{gc}^0 and N_{bg}^0 the free parameters to be fit. In order to generate the source counts to which N_{tot} is fit, we use the SExtractor catalog of extracted sources from the final Sextractor run in each filter band.

The python implementation for SExtractor, `sep`, does not directly supply the magnitude for each identified source, but it does list a total flux. Hence, we convert the fluxes to magnitudes following (e.g. Blakeslee & Tonry, 1995)

$$m = -2.5\log(f) + m_0, \tag{4.18}$$

with f being the flux in units of $\mathrm{e^- \ s^{-1}}$ and m_0 the zero point magnitude (listed for each filter in Table 4).

4.5.1   Fitting the combined luminosity function

In order to fit the combined luminosity function, we have to bin the galaxies into certain magnitude bins, but we empirically find that the choice of bin width does have an effect on the final fitted parameters. Furthermore, a procedure has to be developed that regulates the magnitude bins to be included into the fit; the faintest magnitude bins are incomplete hence should not be included, but when fitting we do not yet know what is the completeness limit. In literature, no detailed procedure has been provided in which these problems are addressed. Hence, we assess the problem ourselves, and empirically find that the following fitting procedure retrieves appropriate results.

As to tackle the choice of bin width, the decision is made to fit the luminosity function for bin widths of 0.5, 0.4, 0.3 and 0.2 mag. For each choice of bin width, we then fit the luminosity function setting the following constraints on the bins to include in the fit. This yields a number of counts $N_{\mathrm{tot}}^{\mathrm{count}}(m)$ in each bin, with m being the central magnitude in that bin.

Then in fitting the luminosity function, we discard the brightest magnitude bin. Although when identifying sources using SExtractor we have made an initial run to mask bright and extended sources, it does sometimes still happen that a bright foreground star is included in the extracted source catalog. As to prevent including this potential source in the fit, we discard the brightest magnitude bin. For the galaxies for which no bright foreground sources are identified in the fit,

we find that excluding the brightest bin does not have a significant effect on the finally estimated residual power.

We then fit Equation 4.15 a number of times, including a different number of bins in each fit. We start with including all of the faintest magnitude bins for the first fit, and for each subsequent fit one lesser bin is included in the fit. We do this until half of the magnitude bins are included into the fit. If less than half of the total number of bins are included, we stop with fitting the luminosity function for that bin. For each fit j, we yield a best fit total number of sources $\widetilde{N}_{\text{tot}}^{j}(m)$.

In order to assess the performance of each fit and to decide whether that fit is of sufficient quality to be included for the final estimate of N_{tot}, we set a number of conditions depending on the magnitude of the faintest bin included in the fit and the yielded completeness limit for that fit.

In order to determine the completeness limit $m_{\text{fit},j}^{\text{cut}}$, we first identify the bins for which the empirical number count $N_{\text{tot}}^{\text{count}}(m)$ is below $0.8 \cdot \widetilde{N}_{\text{tot}}^{j}(m)$. These bins are identified as incomplete. The completeness limit $m_{\text{fit},j}^{\text{cut}}$ is then set to the magnitude of the largest complete bin.

Furthermore, we can call the magnitude of the largest bin that has been included into the fit $m_{\text{fit},j}^{\text{max}}$. If we have included the correct number of bins into the combined luminosity function fit, then the yielded completeness limit should be close to the maximum included magnitude bin. If $m_{\text{fit},j}^{\text{cut}}$ is much above $m_{\text{fit},j}^{\text{max}}$, then we have most likely included too little bins into the fit, and the fit is not of proper quality. Similarly, if we have included too many bins, $m_{\text{fit},j}^{\text{cut}}$ will be below $m_{\text{fit},j}^{\text{max}}$, meaning we have included incomplete bins to the fit, which affects the true result. Therefore, the bound we set on a proper fit is to include the fit j if

$$\|m_{\text{fit},j}^{\text{cut}} - m_{\text{fit},j}^{\text{max}}\| < 0.6 \text{ mag.} \tag{4.19}$$

We can then define the indicator function $\mathbb{I}_{\text{fit}}(j)$, that indicates if condition 4.19 is satisfied for the jth fit. This indicator is given by

$$\mathbb{I}_{\text{fit}}(j) = \begin{cases} 1 & \text{if} \quad \|m_{\text{fit},j}^{\text{cut}} - m_{\text{fit},j}^{\text{max}}\| < 0.6 \text{ mag} \\ 0 & \text{otherwise.} \end{cases} \tag{4.20}$$

Figure 4.5 shows the luminosity function fit for all different bin widths. The different luminosity function fits are represented by the different curves. If $\mathbb{I}_{\text{fit}}(j) = 1$, the curve is shown in bold, and we include the fit into the final estimate for $N_{\text{tot}}(m)$.

Given that each fit yields a number of best fit parameters $\widetilde{m}_{\text{peak},j}^{\text{gc}}$, $\widetilde{N}_{\text{gc},j}^{0}$ and $\widetilde{N}_{\text{bg},j}^{0}$, we estimate the final best fit parameters $\hat{m}_{\text{peak}}^{\text{gc}}$, $\hat{N}_{\text{gc}}^{0}$ and $\hat{N}_{\text{bg}}^{0}$ as the mean of the best fit parameters for which 4.19 holds. This can be written as

$$\hat{m}_{\text{peak}}^{\text{gc}} = \frac{1}{\sum_{j=1}^{J} \mathbb{I}_{\text{fit}}(j)} \sum_{j=1}^{J} \mathbb{I}_{\text{fit}}(j)\, \widetilde{m}_{\text{peak},j}^{\text{gc}} \qquad\qquad j = 1, 2, \ldots, J, \tag{4.21}$$

$$\hat{N}_{\text{gc}}^{0} = \frac{1}{\sum_{j=1}^{J} \mathbb{I}_{\text{fit}}(j)} \sum_{j=1}^{J} \mathbb{I}_{\text{fit}}(j)\, \widetilde{N}_{\text{gc},j}^{0} \qquad\qquad j = 1, 2, \ldots, J, \tag{4.22}$$

$$\hat{N}_{\text{bg}}^{0} = \frac{1}{\sum_{j=1}^{J} \mathbb{I}_{\text{fit}}(j)} \sum_{j=1}^{J} \mathbb{I}_{\text{fit}}(j)\, \widetilde{N}_{\text{bg},j}^{0} \qquad\qquad j = 1, 2, \ldots, J, \tag{4.23}$$

where J is the total number of performed fits over all bin sizes. Similarly, the final completeness limit $\hat{m}_{\text{cut}}$ is estimated as

$$\hat{m}_{\text{cut}} = \frac{1}{\sum_{j=1}^{J} \mathbb{I}_{\text{fit}}(j)} \sum_{j=1}^{J} \mathbb{I}_{\text{fit}}(j)\, m_{\text{fit},j}^{\text{cut}} \qquad\qquad j = 1, 2, \ldots, J. \tag{4.24}$$
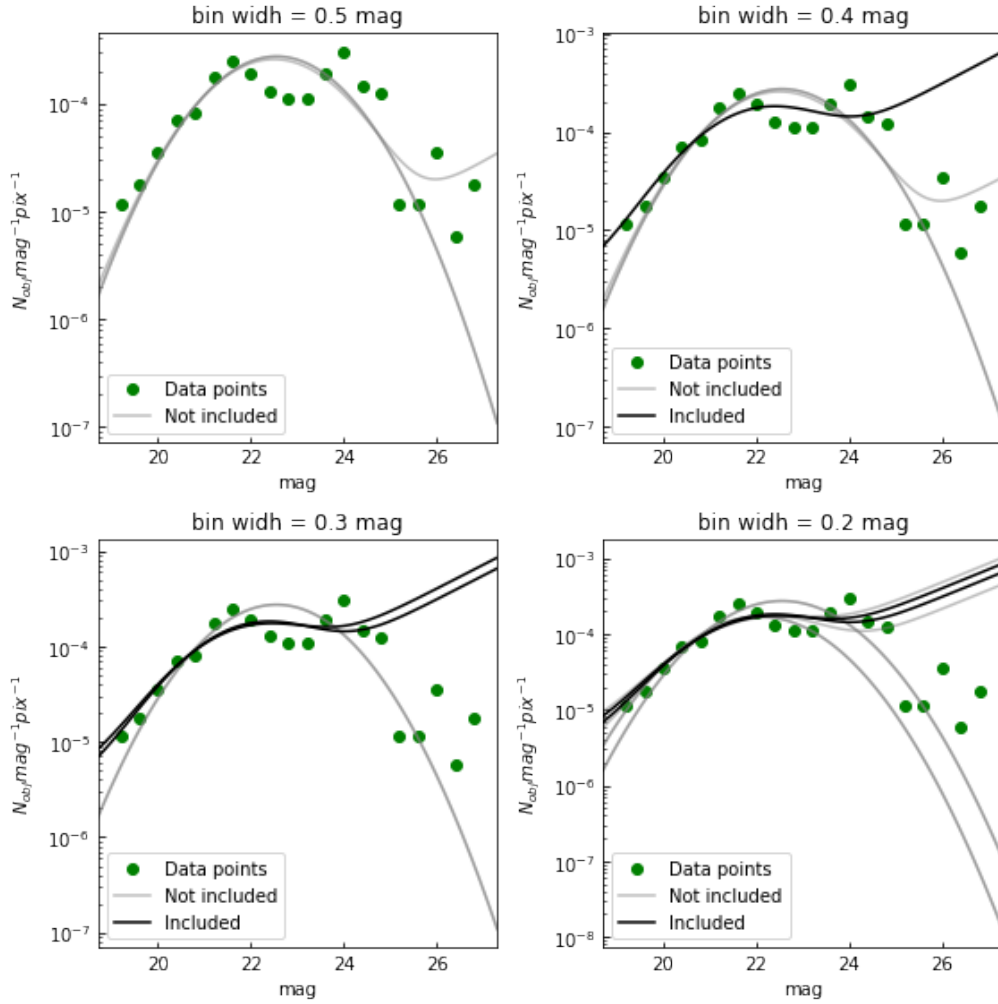
Figure 4.5: The number count of extracted Sextractor sources as a function of apparent magnitude for NGC 1399 in the F160W. The different frames show the number counts for each different bin width. The curves correspond to the fitted combined luminosity function (Equation 4.15), for different numbers of included magnitude bins, as described in Section 4.5.1. The fits for which condition 4.19 holds are shown in bold. Figure 4.6 shows the final fit combining the black curves. The number count is in units of N_{obj} $\mathrm{mag}^{-1}\mathrm{pix}^{-1}$.
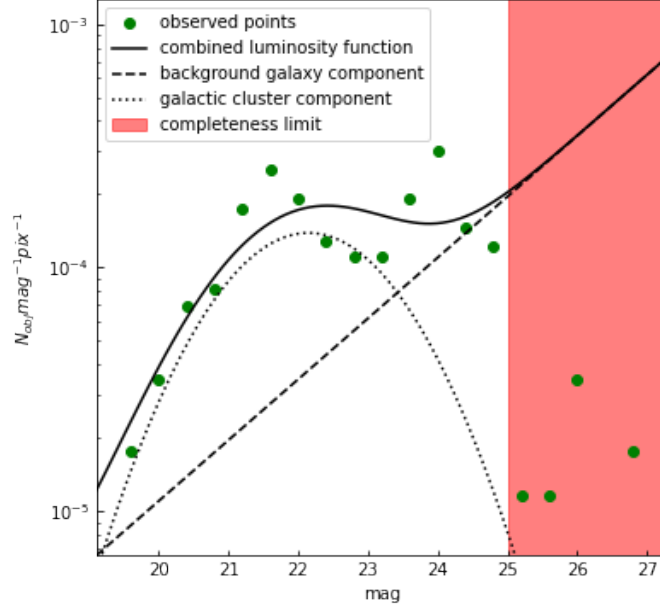
Figure 4.6: The final fitted combined luminosity function N_{tot} for NGC 1399 in the F160W band. The globular cluster component and background galaxy component are both individually plot. The magnitudes fainter than the detection threshold are shown in red. The number count is in units of $N_{\text{obj}} \, \text{mag}^{-1} \text{pix}^{-1}$.

Given these estimates, we eventually calculate the residual power P_r following Equations 4.16, 4.17 and 4.12, where we substitute the best fit $\{\hat{m}_{\text{peak}}^{\text{gc}}, \, \hat{N}_{\text{gc}}^{0}, \, \hat{N}_{\text{bg}}^{0}\}$ into $\{m_{\text{peak}}^{\text{gc}}, \, N_{\text{gc}}^{0}, \, N_{\text{bg}}^{0}\}$. Figure 4.6 shows the combined luminosity function for NGC 1399 in the F160W band, indicating individually the globular cluster component and the background galaxy component (Equations 4.13 and 4.14 respectively).

4.5.2 Some notes on the residual power estimate

For reproducibility of the above results, we make the following notes about the procedure.

- The final residual power is provided in units of e^- pix^{-1}. Hence, $N_{\text{tot}}(m)$ must also be supplied in units of $N_{\text{obj}} \, \text{mag}^{-1}\text{pix}^{-1}$. However, when fitting the luminosity function, we first fit in units of total objects per magnitude, after which we scale the final retrieved N_{tot} with the number of pixels. This is done because the `curve_fit` procedure from `scipy`, which we use to fit the luminosity function, does not work as well at small scales of N_{gc}^{0} and N_{bg}^{0}.

- Sometimes it happens that `curve_fit` does not converge for a chosen bin width. In that case the bin width is reduced by 0.1 for that fitting sequence.

- The currently investigated sample of galaxies allows for almost all fore and background sources to be identified. P_r is in the order of $10^{-3} \cdot P_0$ for essentially all galaxies. Hence, the procedure does not result in a significant effect on the final measured sbf amplitude, but for completeness we do include it in our pipeline.

4.6 Modelling the Point Spread Function (PSF)

In general, the point spread function (PSF) can be modelled following a number of approaches. One can use synthetically modeled PSF's (e.g. TinyTim, Krist et al., 2011), use empirical PSF's or observed PSF's from a data base (e.g. Dauphin et al., 2021) or take bright objects from the observed field of view and model the PSF manually. For SBF measurements, it has been stated

by Pahre et al. (1999) that it is more desirable to use an empirical PSF as opposed to a modeled TinyTim PSF for HST WFC3. Although Jensen et al. (2021) check their inferred PSF with one generated by TinyTim, they also empirically model the PSF for their SBF calculations. Dauphin et al. (2021) discuss the difficulty in accurately modelling the PSF in the infrared, which is challenging due to "breathing" of the instrument (small variations in focal length due to different amounts of warming due to the sun (Anderson, 2022)), changing PSF accross the field, and the centering of the star in a pixel. They provide a library of observed PSF's that can be used to accurately model the PSF for specific scientific applications. The use of this library provides an ideal opportunity to model the PSF for the specific application of measuring Surface Brightness Fluctuations.

In order to model the PSF power spectrum, we hence take the following approach. Since we are dealing with infrared HST images, we initially aim to model the PSF by extracting observed PSF frames from the Dauphin et al. (2021) library, observed around the period that the analysed images were taken. This yields a relatively good PSF power spectrum. Additionally, we make an attempt to model the PSF solely from stars observed in the image field of view. We will see that visually, the resulting PSF power spectrum is not as good of quality as the library-based PSF, but it shows that even without a very accurate externally modeled PSF, the SBF signal can still be measured from a single observation only.

In the following subsections the procedure in modelling the PSF from library observations will be outlined, which is followed by the extension on how to extract the PSF solely from the observed image. The resulting PSF's are compared in Section 4.6.3.

4.6.1   Modeling F160W PSF from library

In order to model PSF's from library observations, by downloading for each individual galaxy a number of PSF frames from the MAST Database[2] (Dauphin et al., 2021), which is the same website as which we have downloaded the original observations. We search for "WFC3 PSF" and select the F110W or F160W band, depending on the observation. Only PSF frames observed at the day of the observation are selected, and we select only PSF frames that have a fit quality parameter below `qfit` $= 0.05$ (selecting only the best quality PSF observations). If less than 40 psf frames are available at the day of the observation, we extend the range of days by one day, until sufficient frames can be downloaded.

In the remainder of this section, we illustrate the PSF selection procedure by showing how the PSF frames are identified for NGC 4073 in the F110W. The procedure for PSF selection is identical to the PSF selection for the F160W band. When selecting suitable PSF frames from the data base, we yield a sample of 82 observed PSFs for NGC 4073.

A sample of PSF frames from the Dauphin et al. (2021) library consists of cutouts with width 51 pixels, centered at the observed star. These PSF's have been observed during various observations of the instrument, and are selected based on how well they are represented by certain models. The PSF's are relatively clean, although some do contain other objects in the cutout field of view. Furthermore, some observations contain `nan` values, e.g. due to cosmic rays. We perform the following processing steps in analysing, selecting and processing the suitable PSF frames.

1. For each of the PSFs we make an estimate of the background level. We estimate the background level by taking a square cutout of width 18 pixels in each of the corners of the image. For each of the four cutouts, we calculate the average flux per pixel. The background level is then assumed to be the median of the four mean signal values. By taking the median we account for the possibility that some pixels might contain outliers such as cosmic rays, corrupt pixels, or other background sources.

---

2. To each `nan` value in the frame, the mean background level calculated in step 1 is assigned.

3. We subtract the median background level from the frame and normalise the cutout such that the sum of pixel values is equal to 1.

4. The 1-dimensional, azimuthally averaged power spectrum is calculated (see Section 4.7 for a detailed explanation of the analysis in Fourier space).

Figure 4.7 shows a subsample of the selected PSFs, in which we also represent the 1-dimensional power spectrum (scaled to fit the image). Clearly, not each of the PSFs are of as good quality as the other. Some frames do not seem to be point sources but background galaxies (e.g. frame 16, 19), in some frames multiple point sources seem to be present in the cutout (e.g. frame 12, 15, 23), and in some the peak of the power spectrum seems to be raised compared to what we see in other frames (e.g. 1, 3, 5). In order to select only the sources of optimal quality, we select PSFs based on the following conditions.

1. From e.g. Dauphin et al. (2021) we know that about 40% of a star's flux in the F110W band must fall on the central pixel. Since the total PSF flux has been normalised to 1, this means that the maximum pixel flux must be around 0.4. Hence, a (moderate) cut is made only selecting the frames for which the maximum pixel flux is larger than 0.2. This removes all sources that are not point sources, while accounting for sources that are not exactly centered at a single pixel.

   For each filter, the maximum pixel flux is different. For the WFC3 F160W band, 20% of the flux falls on the central pixel (Dauphin et al., 2021), so we set a cut of 0.1 for this filter. The cuts for the F850LP and F475W bands are discussed in Section 4.6.4, and are 0.12 and 0.15 respectively.

2. A second cut is made on the standard deviation of the background, in order to only select the highest signal to noise PSF's. Since the standard deviation of the background has been scaled as well when normalising the PSF flux to 1, the standard deviation is a proxy to the signal to noise.

   We estimate the standard deviation of the background in the area 20 pixels from the border of the image (essentially, we mask a box of 11 pixels centered at the PSF). Empirically, we find an adequate cut on the background noise to have the value 0.002 for the infrared bands. A lower signal-to noise level leads to a smaller sample but with better quality sources, with the risk that the sample becomes very small. On the other hand, a higher threshold leads to more sources of questionable quality to be included. All frames with larger background noise level are discarded.

3. Lastly, we make a cut on outliers in the background. If, in the area in which the background was calculated, there exist pixels that have a value smaller or larger than 10 standard deviations from the mean, this means that the background contains other sources or outliers, which we empirically find to raise the peak of the power spectrum at low wavenumbers (as in frames 1, 3 and 5 in Figure 4.7). We discard those frames.

Given that we apply the conditions 1 to 3, we yield a sample of N_{PSF} suitable PSF sources. We denote the image of each individual sampled PSF frame by F_{lib}^i, where "lib" corresponds to the frame being extracted from the library and $i = 1, \ldots, N_{PSF}$. The radial power spectrum of each individual frame then is represented by $\mathcal{PS}(F_{\mathrm{lib}}^i)_r$ (for details see Section 4.7.1).

For NGC 4073, we show the selected PSF power spectra together with the final, combined power spectrum in Figure 4.8. We attempt to combine the PSF frames following two approaches. In the first approach, we estimate the combined power spectrum as the average of the individual PSF power spectra in Fourier space, giving

$$\mathcal{PS}(PSF)_r^{\mathrm{lib}} = \langle\, \mathcal{PS}(F_{\mathrm{lib}}^i)_r \,\rangle_i, \tag{4.25}$$

where $\langle * \rangle_i$ indicates that we take the mean over all components $i = 1, \ldots, N_{PSF}$. In the second approach, we combine the suitable PSF frames into one average PSF cutout, by summing the individual PSF frames and then normalising the combined cutout to have total flux of 1. The power spectrum is ten taken after averaging the individual frames;

$$\mathcal{PS}(PSF)^{\text{lib}}_r = \mathcal{PS}(\ \langle F^i_{\text{lib}} \rangle_i \ )_r. \tag{4.26}$$

We can see in Figure 4.8, the combined power spectrum following either method results in similar spectra for te F110W band.

4.6.2 Modeling PSF from image frame

In section 4.6.3 we will see that the PSF from library stars performs relatively well for measuring the SBF signal. Still, we make an attempt to model the psf solely from the observed image frame. This has the advantage that we should be able measure the SBF signal without any input other than the image. In order to construct the PSF from the observed image, we can use a similar procedure compared to when we estimate the library PSF. We can cut out stars from the original image frame, select good quality PSFs based on criteria, and combine the power spectra to obtain a combined PSF power spectrum. However, we are limited by the quality of our observations and the number of stars in our field of view. In general, the observed stars are less bright and the observed PSFs are more than the library PSF's contaminated by background sources. Hence, we need to perform a number of additional steps in order to optimally make use of the observed stars in the field of view.

4.6.2.1 Identification and selection of stars

First of all, we need to identify, cutout and select the useable stars from the observed image. Although it seems plausible to use the sources that have been extracted by SExtractor when masking background sources in Section 4.4, in practise this does not work as well as we would like due to the different SExtractor runs and chosen thresholds necessary for the source masking. Furthermore, the source catalog that `sep` returns does not offer a suitable overview of point sources with its position, as opposed to the original SExtractor output. Hence, we apply an approach that is based on detecting sources with the `DAOStarFinder` algorithm from the `photutils` package in python. This tool employs the `DAOFIND` algorithm by Stetson (1987), and provides a very effective way to identify point sources. With that in mind, the following approach is applied:

1. We take the observed image and subtract the final galaxy model as estimated with the photutils `ellipse` tool in Section 4.3 to make the residual image R_{ij}. We mask the area for which the profile was not modelled, i.e. equal to 0.

2. We use SExtractor to mask extended sources in the residual frame such as background galaxies and other residual structures left from inappropriate model subtraction.

3. With the `DAOStarfinder` algorithm, we identify point sources in the non-masked area of the frame.

4. For each object, a square cutout is made centered at the object, of width 51 pixels (the same sized cutouts as for the library PSF frames).

5. The sources for which no full 51 pixel width cutout could be made are discarded (i.e. all sources located within 25 pixels from the border of the image).

6. Lastly we discard all sources for which more than 1% of the pixels in the cutout frame were masked.

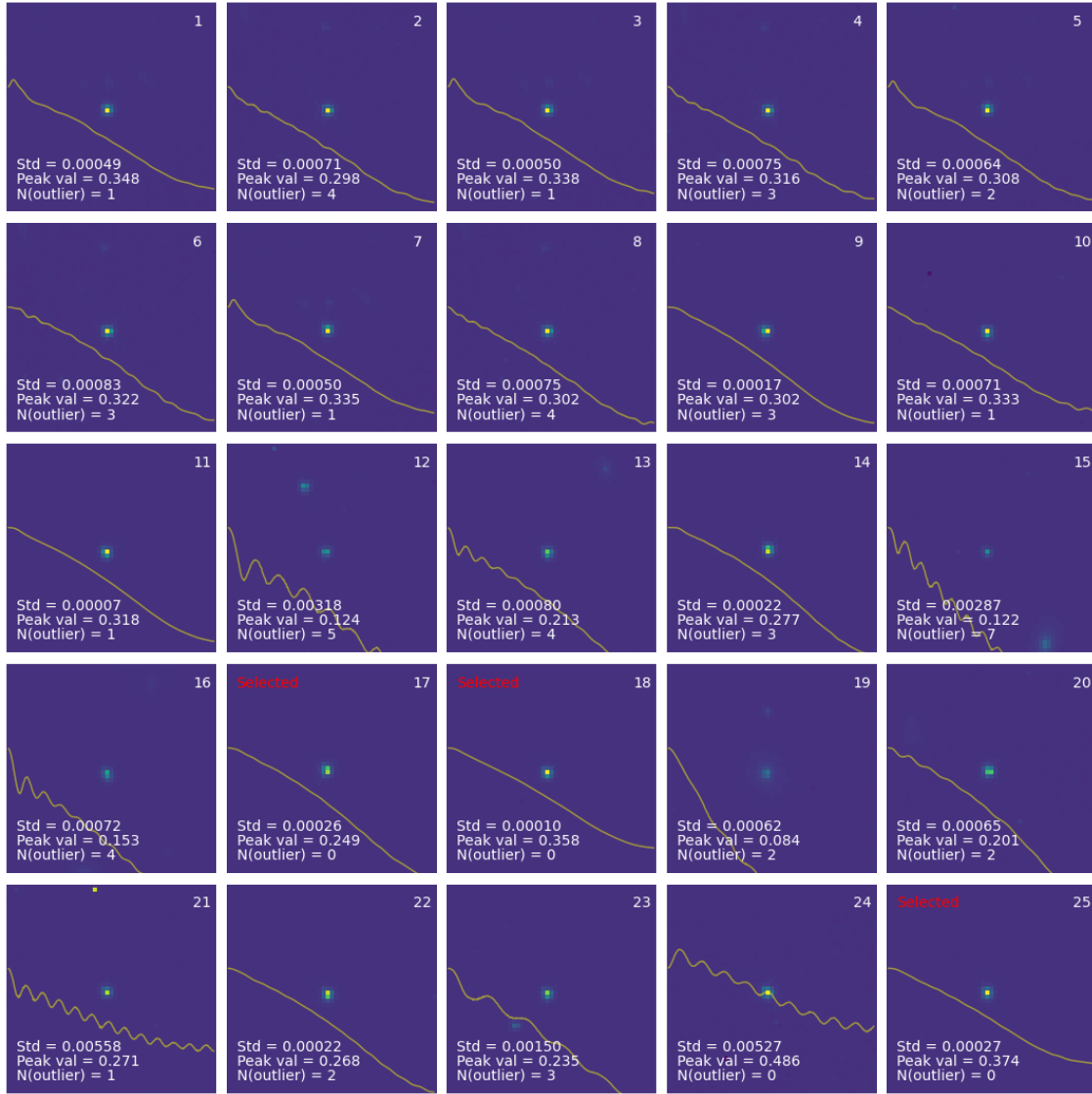The selection of sources shown within the residual image frame is shown in Figure 4.9 for NGC 4073.

Figure 4.7: A Sample of library PSF's from the Dauphin et al. (2021) database. Shown are the data frames, all scaled to the same intensity, and the (scaled) one-dimensional power spectrum of these PSFs. In the bottom left we list the values used to select the frames for the combined PSF. If each of the conditions hold, this is indicated in the top left of the frame. Note that this is not the complete sample of library PSF's for NGC 4073, but only a subsample for visualisation purposes.
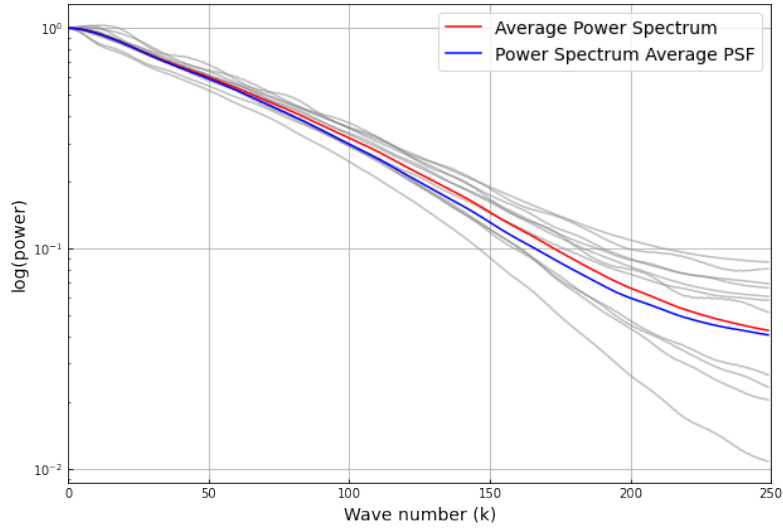
Figure 4.8: The one-dimensional power spectrum of the library PSF frames for NGC 4073. The faint curves correspond to the power spectra of the individual PSF sources. The solid two curves are the combined PSF's, combined by either taking the mean of the individual power spectra (Eq. 4.25), or by taking the power spectrum of the mean combined PSF (Eq. 4.26). The red curve, the power spectrum averaged in Fourier space, is the spectrum used for the final PSF measurement.
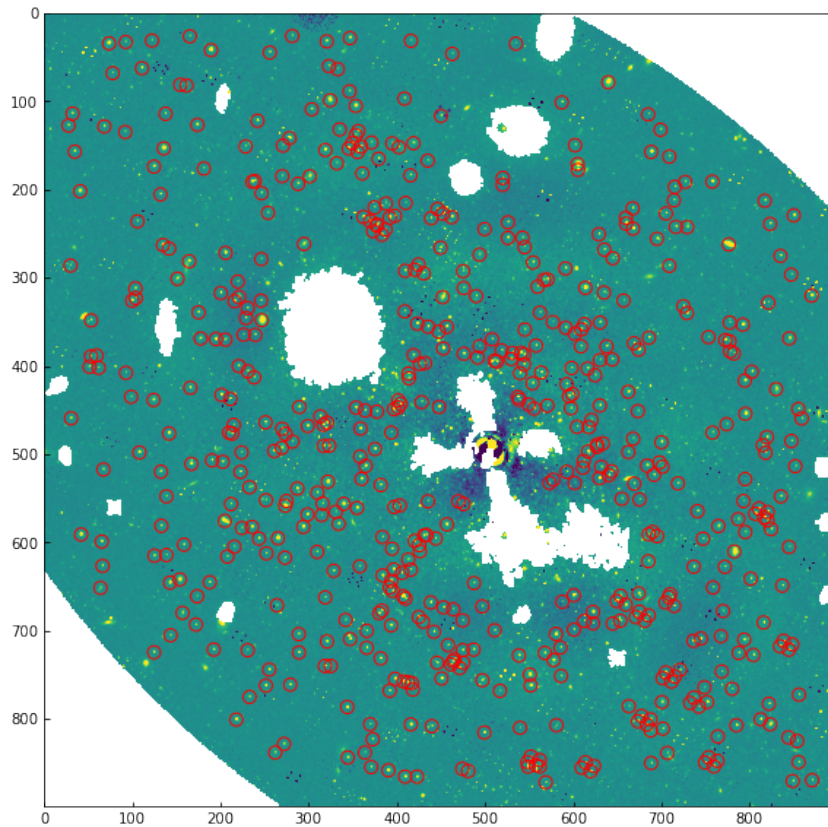
Figure 4.9: Residual image for NGC 4073 with the selection point sources identified with `DAOStarFinder` circled in red. The blank areas have been masked with SExtractor or correspond to the area for which the smooth profile has not been modelled.
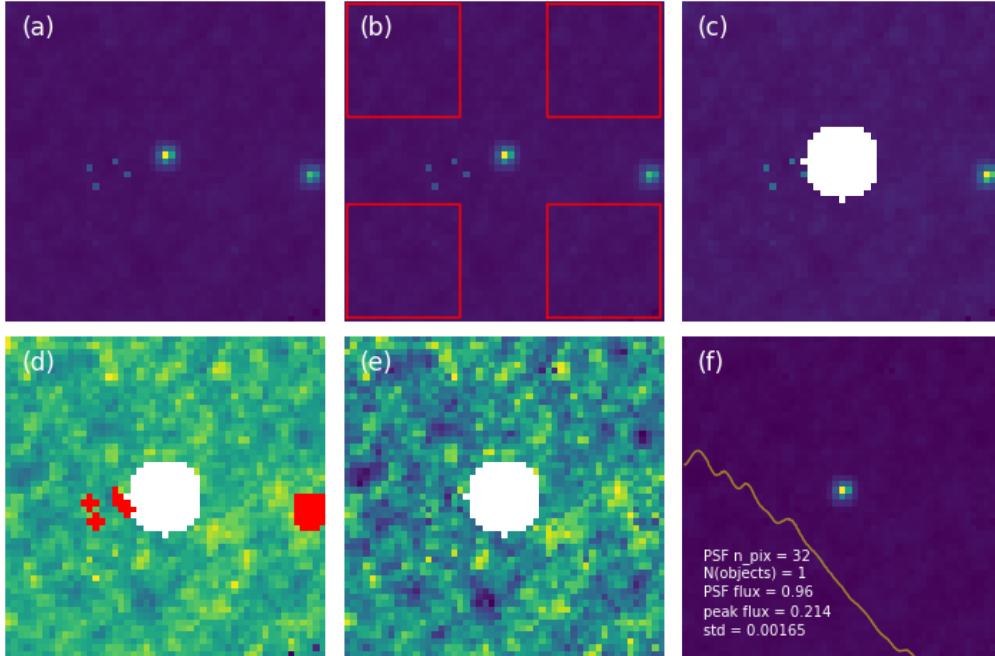
Figure 4.10: An illustration of the psf processing steps for an empirically extracted psf source. (a): The raw psf source extracted from the residual image. (b): The boxes in the corners of the frame in which the background level is estimated. (c): The central annulus masked. (d): The sources identified with SExtractor shown in red. (e) The same masked frame, but Gaussian noise has been substituted at the outliers. (f): The final psf frame with the Fourier power spectrum and the quality parameters.

4.6.2.2 Processing of PSF background

In general, the selected PSF frames from the image frame are of much lower quality than compared to the library PSF frames. The frames are much more noisy (partly due to the subtracted foreground galaxy), and there are many more fore and background sources that affect the power spectrum of the PSF frames. Hence, we want to remove all outliers, fore-, and background sources in the frame. An illustration of the employed processing steps is given in Figure 4.10.

1. First, for each cutout frame, we estimate and subtract the background level as for the library PSF frames (see Step 1). The frames are then normalised such that the sum of pixel values is equal to one (frame (b) in Figure 4.10).

2. A circular annulus of fixed pixel radius centered in the cutout frame is masked (frame (c) in Figure 4.10).

3. We use SExtractor to identify positive and negative outliers in the unmasked area of the frame. We use a threshold of three standard deviations and a minimum area of one pixels. These outliers are masked as well by masking all non-zero pixels from the segmentation map (frame (d) in Figure 4.10).

4. We estimate the mean and standard deviation in the non-masked area of the image (the "clean" background).

5. We remove the sources identified in step 3, and substitute random gaussian noise with mean and standard deviation estimated from the "clean" background (frame (e) in Figure 4.10).

6. We iterate over the area outside of the masked annulus again, and remove outliers larger

than 3 standard deviations from the mean background. Again, random Gaussian noise is substituted with mean and standard deviation estimated from the non-masked area.

7. Lastly, the circular annulus mask is removed, the background is again estimated and subtracted and the image is normalised such that the sum of pixel values is equal to one.

The above steps process the individual PSF frames such that the background area is free from outliers, while keeping the noise properties in the background and keeping an as large part of the original image as possible. However, within the inner annulus no processing has happened and there might still be obscuring objects present in that area. The final selection of PSF frames used for the final PSF calculation is hence based on the following selection criteria:

1. We estimate the standard deviation in the background and remove the frames for which the standard deviation is above 0.003. This value is larger than compared to for the library PSF's because these are generally of better quality. This does in general yield a sample of worse quality PSF frames, but due to the larger size of the sample, the imperfections tend to average out.

2. Each PSF is again passed through SExtractor in order to infer some additional properties of the object:

    (a) If the number of identified sources is larger than one, this means that there is more than one source present and the frame is discarded.
    (b) When the number of pixels that make up the one extracted source is smaller than 20, the frame is discarded (a proper HST PSF should empirically be larger than 20 pixels, otherwise a source often tends to be something that is more closely related to a bad pixel or a cosmic ray).
    (c) The total flux of the extracted source in the SExtractor segmentation map must be between 0.9 and 1.1.

3. We also pass the inverse image through SExtractor in order to identify negative outliers. If these are present, the image is discarded.

4. Again a bound of 0.2 (or 0.1 for the F160W) is set on the peak pixel value, discarding all extended objects.

Executing these selection steps, we eventually identify a number of M_{PSF} suitable PSF frames that can be used to construct the empirical PSF power spectrum. These frames are denoted by F_{emp}^j, with "emp" indicating that these sources are empirical, and have been extracted from the observed image frame, and $j = 1, \ldots, M_{PSF}$. In Figure 4.11 we display the resulting (combined) power spectrum.

Again, we combine the psf frames into an average both by taking the average in Fourier space as well as the average combined psf frames (as in Equations 4.25 and 4.26). Although the two yielded PSF curves were similar to each other for the library PSF, we can see that for the empirical PSF frames, the PSF combined by summing the individual PSF frames follows a different slope as compared to the individual PSF frames. This is most likely due to the centering of the individual PSF frames on the pixel, due to the undersampling of the PSF (e.g. Lauer, 1999), which averages out the PSF frames and makes the combined image more extended. Since for the sbf calculations we are mainly interested in the slope of the power spectrum in Fourier space, it is intuitive to also average the individual PSF frames in Fourier space (similar to what e.g. Jensen et al. (2015) or Foster et al. (2024) do). Hence, we take the power spectrum averaged in Fourier space as the final combined empirical PSF power spectrum, yielding

$$\mathcal{PS}(PSF)_r^{\text{emp}} = \langle\, \mathcal{PS}(F_{\text{emp}}^j)_r \,\rangle_j. \tag{4.27}$$

To keep consistent with the library PSF measurement, we decide to also use the PSF combined in Fourier space for the library PSF, sticking to Equation 4.25.
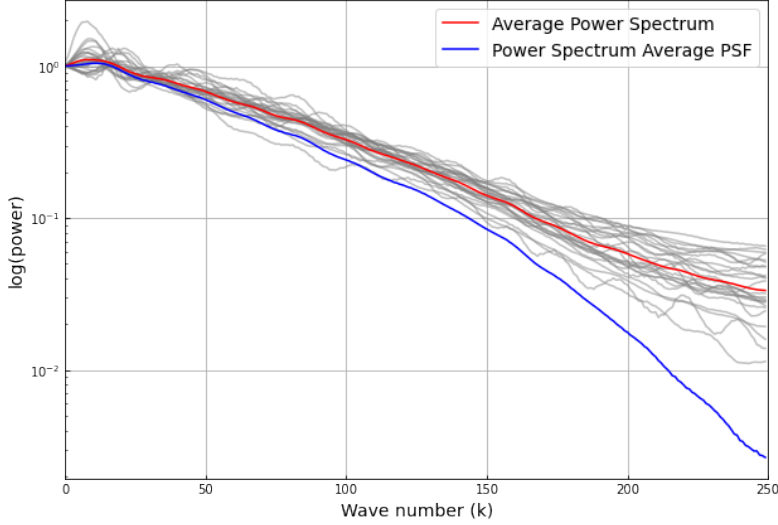
Figure 4.11: The PSF power spectrum for NGC 4073 empirically constructed from suitable observed stars in the image frame (Figure 4.9). The combined psf is shown as the mean of the individual power spectra or as power spectrum of the average psf.

4.6.3 Comparing the infrared library and empirical PSF

In Figure 4.12 we can see the PSF's constructed with the library as well as empirically compared. It is clear that although of lower quality, the empirical PSF is not too far off compared to the PSF constructed with the library. This indicates that, although an accurately modeled PSF is optimal, we can extract a proper PSF from an observed image frame and use that to measure the SBF signal. In Section 5.1.3 we will see that the choice of library PSF or empirical PSF has little effect on the measurement of the final sbf signal in the infrared images. Hence, we will revert to combining the library PSF frames with the empirical PSF frames for the final PSF for the final measurement.

4.6.4 F850LP and F475W passbands

For the F475W and F850LP passbands, the effect of "breathing" of the detector on the PSF is much smaller than for the infrared WFC3 bands, as has been shown by Mei et al. (2007) and Blakeslee et al. (2009) who do not attempt to model the PSF for each detection individually. Instead, they model the PSF from a detection of the moderately crowded globular cluster NGC 104 (Jordán et al., 2004). As we have the framework in place for estimating the PSF from the detected image, we decide to use both the empirical approach as well as the "library" approach, where as the "library" PSF we extract the PSF from the same globular cluster field as in Jordán et al. (2004).

For measuring the empirical PSF in the F475W and F850LP bands, we use that the central pixel encloses approximately 30% of the flux in the F475W band and approximately 25% in the F850LP band (Sirianni et al., 2005). Hence, we set the maximum pixel flux to conservative values of 15% and 12% for extracting suitable PSF sources in the empirical image. We set a threshold on the standard deviation of 0.002, similar as for the WFC3 passbands.

For the "library" PSF, we as mentioned use the observed stars in the globular cluster NGC 104. We download this image from the HST archive, and extract sources in the original data image as done for the empirical PSF (Section 4.6.2). Due to the large number of stars in the field, we are able to set a relatively strict threshold on the standard deviation of the background of 0.0001, yielding only the best quality, highest signal to noise sources. We yield a final sample of
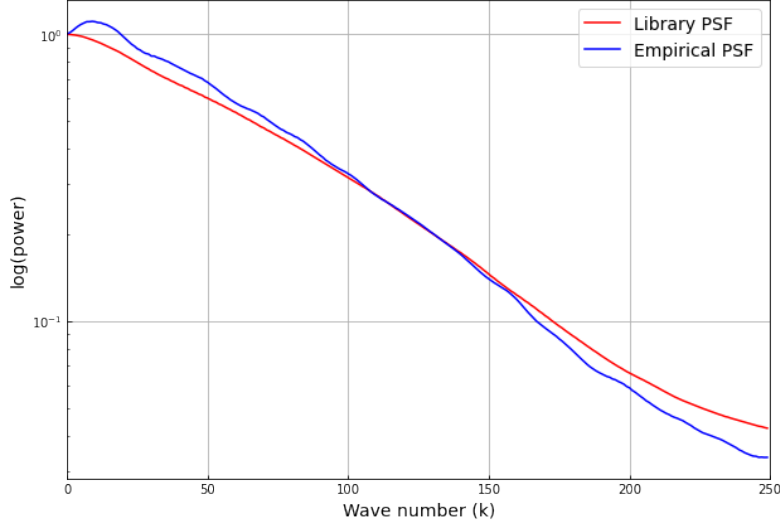
Figure 4.12: The PSF power spectrum for the Library PSF and the Empirical PSF for NGC 4073 compared with each other.
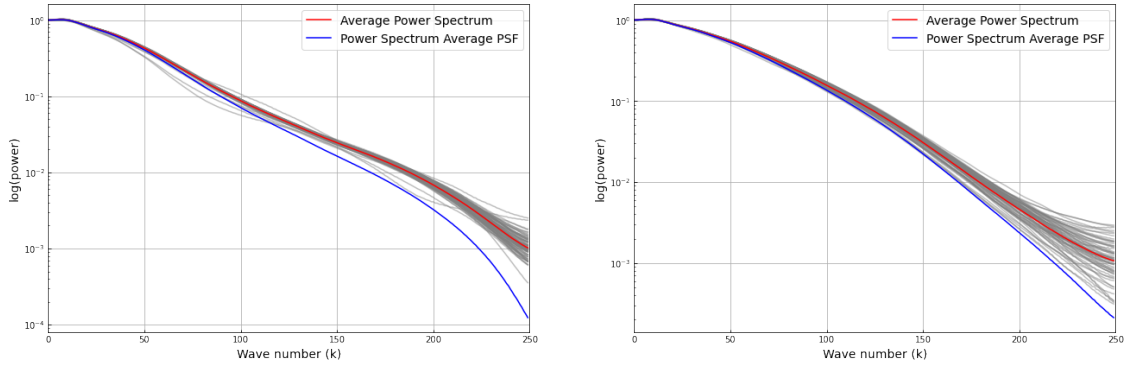

Figure 4.13: Extracted Library PSF for the F850LP filter (left) and the F475W filter (right) from the glubular cluster NGC 104. The grey curves are the power spectra of the individual PSF frames. The red curve is the average of the individual power spectra, and the blue curve is the power spectrum of the combined PSF frames. The red curve is the PSF used for the final sbf measurement.

62 suitable PSF frames for the F475W band and 79 frames for the F850LP band. The extracted PSF power spectra are shown in Figure 4.13.

4.7 Fourier power spectrum

With all the components in place for the sbf measurement, we can move into Fourier space in order to disentangle the instrumental noise component and the sbf component that has been convolved with the psf. To describe the operations in Fourier space required to measure the sbf signal, we follow the detailed outline as presented by Rodríguez-Beltrán et al. (2024).

4.7.1 Fourier derivation

The frame of residual fluctuations I_{ij} is made up of the sbf component and the instrumental noise compontent. This sbf component is convolved with the PSF, while the instrumental noise component is assumed flat, Poissonian noise. If we represent the two dimensional Fourier transform

42

by $\mathcal{F}(*)$, we can represent the Fourier power spectrum by

$$\mathcal{PS}(f) = |\mathcal{F}|^2 = \mathcal{F}(f) \cdot \mathcal{F}(f)^\dagger, \tag{4.28}$$

where $\dagger$ represents the complex conjugate. If we would assume an idealised galaxy, for which the mask M_{ij} is equal to 1 for all i, j, i.e. no areas in the image have been masked, then the normalised residual image would be represented by

$$I = I_{fluc} \otimes PSF + Q, \tag{4.29}$$

where we have left out the i, j in I, I_{fluc} are the surface brightness fluctuations, PSF is the PSF frame, and Q is the residual noise component (which strictly speaking, is the instrumental noise normalised by the squared galaxy model). The power spectrum of Equation 4.29 is represented by

$$\mathcal{PS}(I) = \mathcal{PS}(I_{fluc}) \cdot \mathcal{PS}(PSF) + \mathcal{PS}(Q), \tag{4.30}$$

where we have applied the convolution theorem $\mathcal{F}(f \otimes g) = \mathcal{F}(f) \cdot \mathcal{F}(g)$. The cross terms that should show up in Equation 4.30 due to the sum in Equation 4.29 is neglected. Rodríguez-Beltrán et al. (2024) show that these cross terms are three orders of magnitude lower than the rest of the terms, indicating that these can safely be neglected.

The Fourier power spectrum $\mathcal{PS}$ is still a two-dimensional image of dimensions $(n_{\mathrm{pix}} \times n_{\mathrm{pix}})$, which are the same dimensions as the original frame I. We apply an azimuthal average to these power spectra and collapse the power to one dimension. This results in a radial profile of dimensions $n_{\mathrm{pix}}/2$. The radial profile is a function of frequency k in units pix^{-1}. The total azimuthal average will be the sum of the azimuthal average of the individual components. The sbf fluctuations $\mathcal{PS}(I)$ reduce to a constant component that we represent by P_0, the sbf power. By representing the azimuthal average with the subscript r, we reduce Equation 4.30 to

$$\mathcal{PS}(I)_r = P_0 \cdot \mathcal{PS}(PSF)_r + \mathcal{PS}(Q)_r. \tag{4.31}$$

In this derivation, the mask M_{ij} has not yet been taken into account. Rodríguez-Beltrán et al. (2024) show that when the mask is included, Equation 4.31 becomes

$$\mathcal{PS}(I)_r = P_0 \cdot (\mathcal{PS}(PSF) \otimes \mathcal{PS}(M))_r + \mathcal{PS}(Q \cdot M)_r, \tag{4.32}$$

were we point out that the azimuthal average of $(\mathcal{PS}(PSF) \otimes \mathcal{PS}(M))$ only gets taken after convolving the two components in 2D Fourier space.

In the classical notation, Equation 4.32 is represented as

$$P(k) = P_0 \cdot E(k) + P_1, \tag{4.33}$$

with $P(k)$ the Fourier power of the normalised residual image I_{jk}, $E(k)$ the expectation power due to the PSF power spectrum and the mask, and P_1 the flat Poissonian instrumental noise.

4.7.2 Measurement in practise

In practise, we can measure the Fourier power spectrum by calculating the radial Fourier power spectrum of the normalised residual image I_{ij}, the mask M_{ij}, and the PSF, represented by PSF. While the first component $P(k)$ is computed relatively easily, we note that for the expectation power spectrum $E(k)$, we cannot simply compute the power spectrum of the final combined PSF frame. At the end of Section 4.6.2.2, we have made the choice to take the average of the psf power spectra in Fourier space and use that to characterise the final psf power spectrum. However, as to compute the expectation power spectrum, the PSF power spectrum is convolced with the mask power spectrum before averaging to one dimension. Hence, as to average the individual PSF frames and compute the expectation power spectrum, we first convolve the power spectrum of
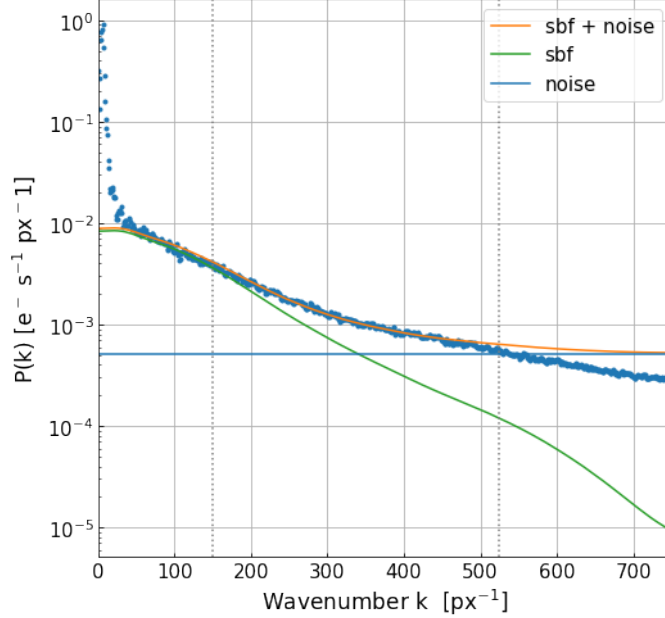
Figure 4.14: The fit of Equation 4.33 for the sbf signal of NGC 1404 in the F850LP band. The orange curve corresponds to the fit of the combined power spectrum $E(k)$. The green curve is the power due to the sbf signal $P_0 \cdot E(k)$, and the blue horizontal curve is the instrumental noise component P_1. The vertical dotted lines indicate the lower and upper bound on the wavelength range for which he fit has been made.

each individual PSF frame with the mask power spectrum, and then we take the average.

Given that each individual PSF frame that is combined to create the final PSF can be represented by PSF_i, we compute the final expectation power spectrum by

$$E(k) = \big\langle\, (\mathcal{PS}(PSF_i) \otimes \mathcal{PS}(M))_r \,\big\rangle_i ,\qquad(4.34)$$

where the operators $\langle * \rangle_i$ indicate that we are taking the average over the components i.

We calculate the Fourier transforms and the radial power spectra using the `numpy.fft` module in python. The convolution of the mask and psf power spectra is made with `scipy.signal.convolve` (Virtanen et al., 2020).

4.7.3 Fitting the components

With the calculated power spectrum of the normalised residual image and the expectation power spectrum as in Equation 4.34, we can make a fit to estimate the components P_0 and P_1. Taking $P(k)$ and $E(k)$ as given, we fit the components in python using `scipy.optimize.curve_fit` (Virtanen et al., 2020). We present an example of the power spectrum fit in Figure 4.14.

However, a crucial component of fitting the power spectrum relates to the wave numbers to be included into the fit. As has well been established (e.g. Biscardi et al., 2008; Cantiello et al., 2013; Kim & Lee, 2021), the sbf power at low wavenumbers is affected by large scale residuals due to subtraction by the smooth surface brightness profile, while the power spectrum at large wave numbers is affected by the correlated noise from stacking the individual images (Mei et al., 2005a; Cantiello et al., 2005). Hence, the highest and lowest wave numbers should be excluded from the power spectrum fit.

However, there is no well established procedure on how the lower and higher wavenumber are determined. Some works fit the spectrum for a range of wavelength ranges and find where the measured sbf power stabilises (Biscardi et al., 2008; Cantiello et al., 2013, 2018b). Other works estimate the sbf amplitude with a Monte Carlo approach; randomly sampling the upper and lower wavenumber and taking the median or mean value as the final sbf amplitude (Carlsten et al., 2019b) and its standard deviation as the uncertainty. Jensen et al. (2015) and Foster et al. (2024) simply set empirically determined bounds on the wavelength range to include.

In our analysis, we will apply a version the approach by Carlsten et al. (2019b). Instead of measuring the sbf amplitude for a randomised set of wavenumbers, we instead create a grid of initial and final wave numbers, and fit the power spectrum for the whole grid of wave numbers. We then take the mean of the grid as the final sbf amplitude and the standard deviation of all the measurements as the uncertainty on the fit.

Given that the wavenumber range of the power spectrum is $k \in \{0, \dots, k_{max}\}$, with $k_{max} = n_{\mathrm{pix}}/2$, we can call the lower bound on the wavenumber to be included in the fit k_- and the upper bound k_+. We then create a grid of the lower bound between $0.1 \cdot k_{max} \leq k_- \leq 0.4 \cdot k_{max}$. For the upper bound we set $0.6 \cdot k_{max} \leq k_+ \leq 0.8 \cdot k_{max}$. We fit Equation 4.33 for each initial and final wavenumber in the grid. The mean sbf amplitude is taken as the final value for P_0. The standard deviation on the amplitudes is assumed as the uncertainty on the fit.

For vizualisation purposes and as to have a set wavenumber range for fitting the sbf amplitude for estimation of the uncertainties due to other components (as will be outlined in Section 4.8), we set the lower wavelength number to $k_- = 0.2 \cdot k_{max}$ and the upper bound to $k_+ = 0.7 \cdot k_{max}$. These bounds are indicated by the vertical dotted lines in Figure 4.14.

4.8 Uncertainties

With all the components for the sbf measurements in place, we have extracted the Fourier power P_0 and the residual power P_r and combine those to calculate the sbf apparent magnitude following Equation 2.2. We assess the uncertainty on this measurement in four components; the uncertainty of the background, the uncertainty due to the PSF, the uncertainty due to the Fourier fit and the wavenumbers used for the fit, and the uncertainty on the residual power P_r. Lastly we will describe the procedure employed to measure the sbf signal in various radii of the galaxy.

- **Background**: The uncertainty on the background can be computed relatively easily, as we have an estimate of the uncertainty on the final background level, computed in Section 4.2. We calculate the uncertainty at the various background levels by creating two alternative normalised residual images

$$I_{ij}^+ = \frac{(R_{ij} + \sigma_B) \cdot M_{ij}}{\sqrt{O_{ij} - \sigma_B}} \tag{4.35}$$

  and

$$I_{ij}^- = \frac{(R_{ij} - \sigma_B) \cdot M_{ij}}{\sqrt{O_{ij} + \sigma_B}}. \tag{4.36}$$

  For both the sbf power is estimated and the apparent sbf magnitude is calculated. The uncertainty on the magnitude due to the background level, σ_{bck}, is equal to half of the difference between the two sbf magnitudes.

- **PSF**: We measure the uncertainty of the PSF by calculating the sbf magnitude for each individual PSF frame. For each PSF frame in the sample, we then yield a magnitude $\overline{m}(F^i)$. The standard deviation of the PSF is then equal to the standard deviation of the individual PSF magnitudes, and is represented by σ_{psf}.

	F110W			F160W			F850LP			F475W		
	mean	min	max	mean	min	max	mean	min	max	mean	min	max
σ_{tot}	0.18	0.08	0.29	0.16	0.08	0.31	0.14	0.11	0.18	0.18	0.08	0.27
σ_{psf}	0.14	0.04	0.27	0.15	0.02	0.30	0.07	0.07	0.07	0.03	0.03	0.03
σ_{fit}	0.10	0.07	0.22	0.06	0.01	0.09	0.12	0.08	0.17	0.17	0.08	0.27
σ_{bck}	0.00	0.00	0.01	0.00	0.00	0.01	0.00	0.00	0.00	0.00	0.00	0.01

Table 5: Overview of the individual uncertainties in each filter band. The units are in mags. For each uncertainty type and filter, the mean, minumum, and maximum of the uncertainties are reported, given all galaxies in the sample. σ_{res} is not shown, as this is a factor 10^3 lower than each of the other uncertainties.

- **Fourier fit**: As presented in Section 4.7.3, the final sbf power is estimated by fitting Equation 4.33 for a grid of initial and final wavenumber k. For each of these fits, we find an sbf power P_0, wich we can use to calculate an sbf magnitude. The uncertainty on the sbf magnitude due to the Fourier fit, is then given by the standard deviation of the sbf magnitudes in the grid. This uncertainty is denoted by σ_{fit}.

- **Residual power**: The uncertainty on the residual power has been difficult to characterise. In line with Mei et al. (2005b) and Blakeslee et al. (2009), set the the uncertainty of P_r equal to 25% of P_r. This should capture all effects due to the varying combined luminosity function fits. This also yields an uncertainty on the sbf magnitude that is denoted by σ_{res}.

We combine the individual uncertainties into a total uncertainty by

$$\sigma_{\mathrm{tot}} = \sqrt{\sigma_{\mathrm{bck}}^2 + \sigma_{\mathrm{psf}}^2 + \sigma_{\mathrm{fit}}^2 + \sigma_{\mathrm{res}}^2}. \tag{4.37}$$

We provide an overview of the yielded uncertainties for each band in Table 5.

4.8.1 Annular mask

We note that we do not incorporate the effect of varying the radius in which the sbf signal is measured in the uncertainty measurement. Just as Blakeslee et al. (2009), Jensen et al. (2015) and Jensen et al. (2021) we measure the sbf amplitude in a series of consecutive, concentric annuli, with sizes between 4 and 9 arcsec, 9 and 16 arcsec, 16 and 30 arcsec, and 30 and 60 arcsec. We convert these radii to pixels using the plate scales of 0.13 arcsec/pixel for WFC3 and 0.05 arcsec/pixel for ACS WFC (Dressel, 2015). This yields the various radial masks M_{ij}^{radial}.

The condition for a radial mask to be considered are that at least 50% of the pixels in the annulus must not be masked by any of the other masks $M_{\mathrm{bad\ pix}}, M_{ij}^{\mathrm{galmodel}}$ or M_{ij}^{source}. Besides the measurements in the radial masks, we also make a measurement including the whole part of the galaxy incorporated by $M_{ij}^{\mathrm{galmodel}}$.

4.9 Some final notes

Given the presented methodology, a pipeline has been implemented that is able to measure the sbf magnitude and its uncertainties in an automated manner. The constructed variables in each stage are stored in a directory and can be called for later use. The Figures 4.2, 4.3 (left frame), 4.5, 4.6, 4.1 (frame d) 4.7, 4.9, 4.11 and 4.14 are made for each galaxy and the corresponding filter band. For each galaxy in our sample, we store these Figures on the following cloud service, to be used for reference: link[3]. Furthermore, we provide the documented code, with some examples of how the code can be used on the following web page: link[4].

---

[3]https://astrodrive.astro.rug.nl/index.php/s/Tg5yRlV5vKWcavg
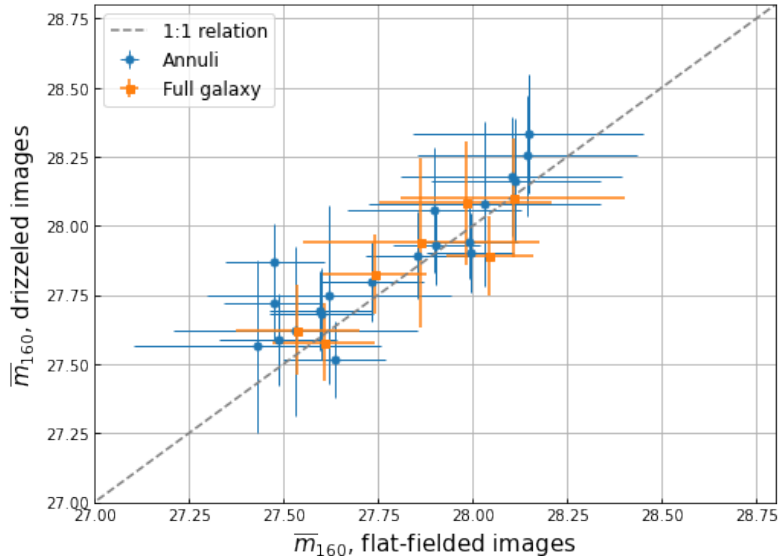[4]https://github.com/leititulaer/SBF_Pipeline/tree/main

Figure 5.1: The apparent sbf magnitudes in the F160W measured from the drizzeled images compared with the sbf magnitudes measured from the flat-fielded images. The blue points correspond to the measurements in the different annumi, whereas the orange squares correspond to the full galaxy measurement.

5 Results

The first results, showing the effect of various model choices on the measured sbf amplitude are discussed in Section 5.1. Based on these analysis the final model choices for the psf is made, allowing to make a comparison with the sbf measurements measured in this work and results from literature in Section 5.2. In Section 5.4 an overview of the results in the context of stellar population models will be provided.

5.1 Methodological choices

Following the full methodology as outlined in Section 4, we have left a number of different options in the way in which the final sbf signal can be measured, including the use of files from a different HST processing stage (flat-fielded or drizzeled, Section 4.1), or the use of either the empirical PSF or the library PSF (Section 4.6). This subsection aims to show the effect of these model choices on the finally measured sbf magnitude, and makes a decision on the model choices to be employed for the remained of the results.

5.1.1 flat-fielded frames against drizzeled frames

For the F160W band, we have measured the sbf magnitude both by using the images from the flat-fielding stage in the HST processing pipeline, or by using the fully processed files for which the individual exposures have been drizzeled in order to obtain the combined image.

Figure 5.1 shows the apparent sbf magnitude in the F160W band measured with the drizzeled images compared with the magnitudes measured with the flat-fielded images. Both the measurements in the individual annuli as well as for the full galaxies are shown.

We can see that in general, the measurements seem to correspond well between the two processing stages. Although there is a small systematic difference between the mean measurements ($\langle \overline{m}_{160,drz} - \overline{m}_{160,flt} \rangle = 0.088 \pm 0.110$ mag), this is well within the average uncertainty of the sbf measurements within this range, which is equal to 0.199 mag.
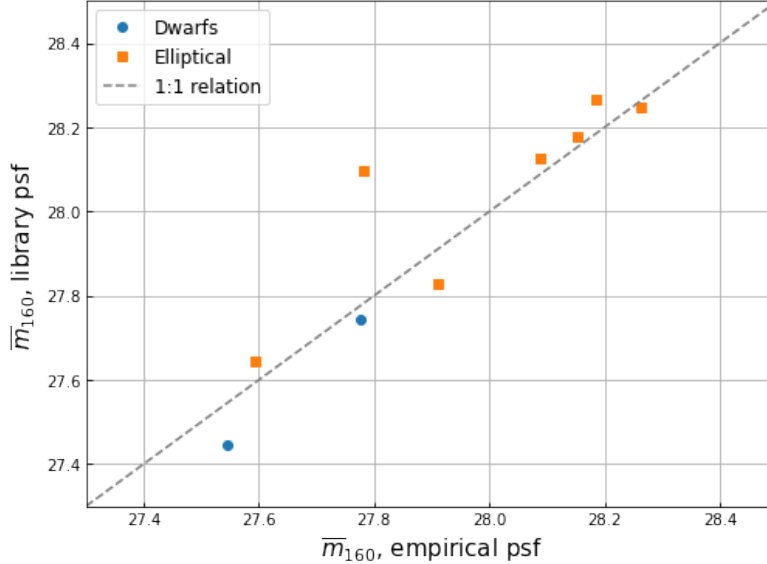
Figure 5.2: The F160W apparent sbf magnitude measured using the library PSF from the HST archive, compared with the magnitude measured using the PSF extracted from the observed image. The dwarfs and ellipticals in the sample have different icons and colors. The measurements have been made from the drizzeled images and uncertainties are not shown here, as these are calculated at a later stage in the pipeline at which a choice has been made to use a specific subset of PSF frames.

As the difference between the measured sbf amplitude is well within the uncertainties between the flat-fielded measurements and the drizzeled measurements, we decide to only proceed with the measurements from the drizzeled stage, as it has in general proven easier to measure the signal for those frames.

Note that we were only able to properly measure the sbf signal from the flat-fielded frames for 7 of the 15 galaxies. For the others, sbf measurements mostly failed due to the galaxies being too small for the field of view, leading to difficulties in the isophotal model fit. Although we could have chosen to make a manual image cutout for these galaxies, we decided to not do this as we have seen that the measurements for the drizzeled and flat-fielded images in general show good correspondence.

5.1.2 Library PSF against empirical PSF

Both for the infrared as well as the visible bands, we can make the comparison between the measured sbf magnitude using the empirical PSF and the library PSF. Since the results are slightly different for the WFC3 bands and the ACS bands, we will address those separately. We will only address the F160W band and the F850LP bands here, the results are similar for the F110W and F475W.

5.1.3 Infrared

In Figure 5.2 we show the measured apparent sbf magnitudes in the F160W band in which we compare the measurement made using the empirical PSF, with that using the library PSF. We do not show uncertainties in this plot because these are calculated in a later stage of the sbf pipeline, at which a final choice has been made in which PSF frames to be used.

We can see that in general, there seems to be good correspondence between the sbf measurement between the empirical PSF and the library PSF. Again, there is a slight discrepancy of $\langle \overline{m}_{160,emp} - \overline{m}_{160,lib} \rangle = 0.083 \pm 0.143$ mag, but this falls well within the uncertainties.

Since there is no significant difference in the result between the empirical PSF and the library PSF, we decide to use both the extracted empirical PSF frames as well as the library PSF frames for the final sbf measurement in the F160W.

We note that NGC 4458, IC 3025, IC 3487 and IC 3586 are not shown in Figure 5.2. This is due to the fact that no suitable empirical PSF sources could be extracted for these galaxies. As we have decided to combine the library PSF frames with the empirical PSF frames and there does not seem to be a significant difference between the two sbf measurements, we do not deem this to be a problem for the final sbf measurement in these galaxies.

5.1.4 Visible bands

In the left frame of Figure 5.3 we show the the measured apparent sbf magnitude comparing the measurement with the library PSF with that of the empirical PSF as in Figure 5.2, but now for the F850LP filter. A clear systematic discrepancy between the two measurements can be identified, which is quantified by a mean magnitude difference of $\langle \overline{m}_{850,emp} - \overline{m}_{850,lib} \rangle = 0.784 \pm 0.342$ mag.

As to address which of the measurements is of better quality, we compare the measurement with those by Blakeslee et al. (2009) in the right frame of Figure 5.3. In that image it becomes clear that the measurements with the library PSF follow a relatively good correspondence with the literature values by Blakeslee et al. (2009). The empirical PSF seems to systematically underestimate the sbf flux, leading to larger sbf magnitudes.

As the library PSF values clearly show more consistent results, we decide to disregard the empirical PSF measurements and only use the library PSF frames for measuring the F850LP signal and its uncertainty in the remainder of this work.

We do not address the F475W filter here as no reference values in literature are available for this band, meaning that we cannot make the comparison with literature as in the right frame of Figure 5.3. However, there also exists a systematic difference between the empirical and library PSF measurement of $\langle \overline{m}_{475,emp} - \overline{m}_{475,lib} \rangle = 0.201 \pm 0.148$ mag. For reference, the library PSF against empirical PSF plot as in Figure 5.3 for the F475W is given in Appendix B.1.

Although we could opt for continuing with measurements using both the library PSF frames and the empirical PSF frames as we did for the F160W, we note that the discrepancy between the two sbf measurements is systematic, instead of fully random. Although we cannot compare our measurements with literature to identify which measurements are of better quality, we use our experience with measurements of the ACS WFC in the F850LP. As to stay consistent with these other measurements with ACS WFC imaging, we decide to only keep the library PSF measurements for measuring the sbf magnitude and its uncertainty in the remainder of this work for the F475W.

5.1.5 Background level and final adjustments

When presenting the results thus far, we have performed an estimate of the background level as explained in Section 4.2. However, it has turned out that for a significant share of the galaxies, the initial background estimate does not seem to be physically correct. The fit of the Sérsic profile and background component sometimes converges to a Sérsic index that is not in line with values found in literature, and leads to sometimes negative, or very high background levels. This lead to significant outliers in the results presented below. As to correct for these outliers, we have run
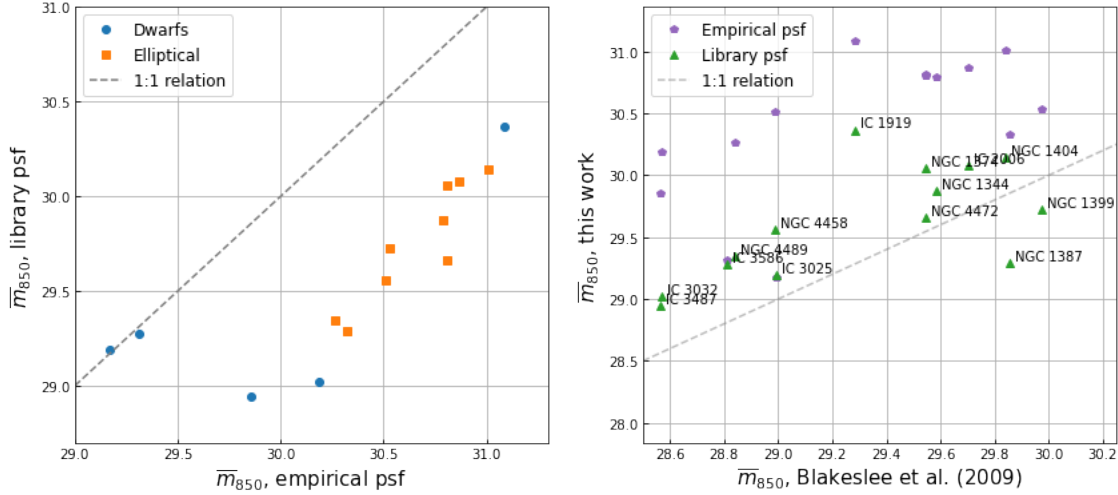
Figure 5.3: The F850LP apparent sbf magnitude measured using the library PSF from the HST archive, compared with the magnitude measured using the PSF extracted from the observed image. The left frame shows the comparison as in Figure 5.2, with the dwarfs and ellipticals in different icons and colors. The right frame shows the apparent sbf magnitude computerd either with the library PSF or the empirical PSF, compared with the measurement from Blakeslee et al. (2009). In both frames the 1:1 relation is shown as a dotted line. In both frames, no uncertainties are shown as these are calculated in a later stage of the sbf pipeline.

the measurement pipeline again with an alternative background level for these galaxies.

Table 6 lists a summary of the estimated background levels for all galaxies in each band. For the outliers (discussed in Section 6.1), we rerun the algorithm with a background level B equal to the median background level reported in Table 6. As standard deviation, we take the difference between the minimum level and the median reported in the same table. This conservative uncertainty should account for the fact that this is a broad estimate, and it should not be considered the true background level.

Each graph that is presented in the following Sections, is also shown with the original results that include the outliers due to incorrectly estimated background in Appendix C.

5.2 Compare with literature

With established choices for the psf models and file types, we can now compare our measurements with the measurements made in literature. This will be a good test for the validity and consistency of our measurement pipeline as compared with previous works.

5.2.1 Infrared

For the infrared bands we display the inferred absolute sbf magnitude compared with the result by Jensen et al. (2015) in Figure 5.4. The apparent SBF magnitudes have been converted to absolute SBF magnitudes by using the distance moduli presented in Blakeslee et al. (2009). We present the version of the absolute sbf magnitudes from Jensen et al. (2015) that have been measured using the same distance moduli.

In Figure 5.4, a trend can be observed in both wavelength bands with the exception for some apparent outliers (IC 3025, NGC 4489) in the F160W band. However, for both bands we seem to by systematically underestimating the sbf power as compared to the values reported by Jensen
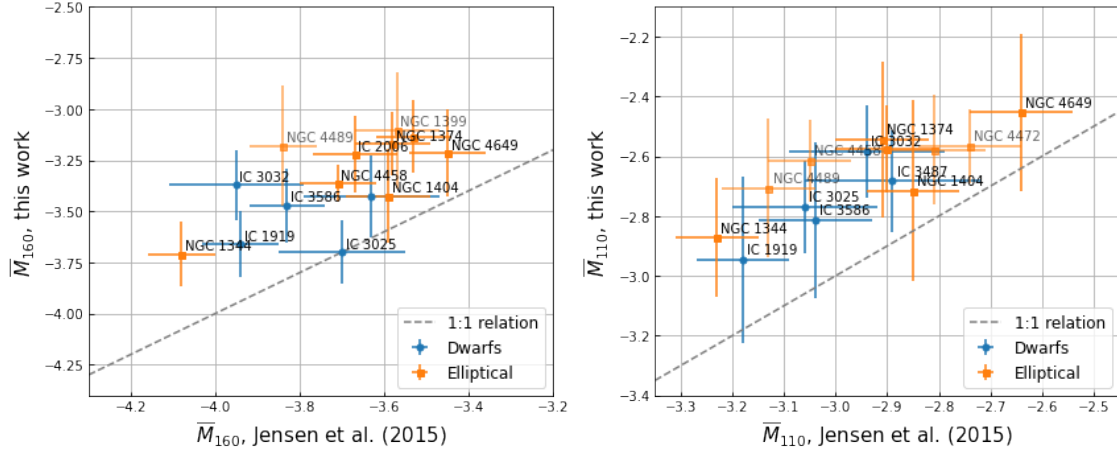
Figure 5.4: Comparison of the absolute sbf magnitude in the F160W and F110W bands with the absolute SBF magnitude by Jensen et al. (2015). The dwarfs and ellipticals are shown with different symbols and colors. The 1:1 relation is shown by the dotted line. The faint galaxies correspond to galaxies for which the sbf measurement did not succeed. These are discussed in Section 6.1. In the left frame, the labels for NGC 4472 and IC 3487 are not shown as they overlap the galaxies around NGC4458 an NGC 1374. In the right frame, the same holds for NGC 1399 and IC 2006.

et al. (2015).

5.2.2   F850LP

For the visible bands, we can only make a comparison with literature in the F850LP; there have not been made measurements for the F475W band before. We make the comparison with the measurements by Blakeslee et al. (2009) in Figure 5.5.

Again, we have converted apparent sbf magnitudes to absolute sbf magnitudes using the distance moduli presented in Blakeslee et al. (2009). We can see that there is relatively good correspondence between the values in Blakeslee et al. (2009) and those that we have measured, although again with a seemingly systematic underestimation of the sbf power.

5.2.3   Color-sbf calibration

To complete the comparison with literature, we display the color-magnitude calibration for each filter band as proposed by Jensen et al. (2015) and Blakeslee et al. (2009). Both studies present calibrations for the relation between $g_{475} - z_{850}$ color and absolute sbf magnitude in their works with the main goal to be able to calibrate the distance measurement. For both the F110W and F160W bands, Jensen et al. (2015) provide two calibrations; one that includes bluer colors below $(g_{475} - z_{850}) < 1.2$ mag, and a linear calibration that only holds for the red galaxies. For the F475W, no calibrations are available, but we do show the relation in this image to indicate the trend present. Evidently, we see a similar behavior as in Figure 5.4 and 5.5, although we can now better see what the effect is on the offset based on color.

5.3   Sbf gradients

A potentially interesting component when measuring surface brightness fluctuations is the existence of sbf gradients. These gradients are an indication of potentially varying stellar populations in the different regions of the galaxy, and can aid with the interpretation of sbf calibrations. On the other hand, sbf gradients can be an indication of inconsistencies in the measurement pipeline. For example, an incorrectly subracted background level has a larger influence towards the faint
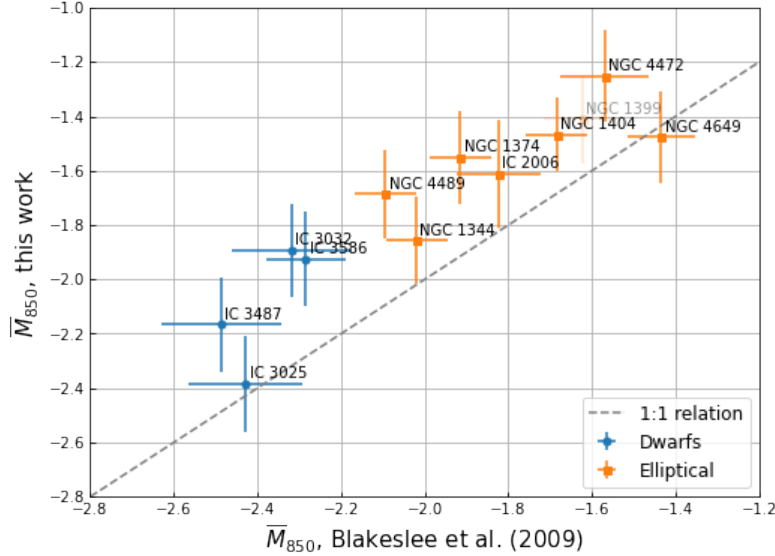
Figure 5.5: Same as in Figure 5.4, but now comparing the F850LP measurements with the reference values from Blakeslee et al. (2009).

outer edges of the galaxy than towards the center. A significant incorrectly estimated background level hence could lead to an observed sbf gradient.

In Figure 5.7 we can see that for some galaxies noteworthy sbf gradients exist. The uncertainties due to sbf gradients have not been taken into account in comparing with literature in Figures 5.4 and 5.5, but they do provide significant implications for these comparisons. Both Jensen et al. (2015) and Blakeslee et al. (2009) measure $\overline{m}_{160}$ and $\overline{m}_{850}$ in regions of varying radius for each galaxy, and they have slightly different bounds on the width of the annuli used and the shape (elliptical or circular). Hence, although we could include the uncertainty due to radial sbf gradients into the full galaxy sbf uncertainty, it might be much more insightful to compare the sbf-color relation in each of the concentric annuli.

Extreme examples of sbf gradients include NGC 1399, NGC 1374, and NGC 1404. For these galaxies, the difference between the sbf measurement in various annuli seems to span more than 0.5 mag. Although sbf gradients can be expected, these gradients should not be of this magnitude. Hence, the sbf gradients here might either be an indication of an improper sbf measurement for these galaxies, or alternatively might indicate the sensitivity of the sbf measurement to the chosen radius of the galaxy. We note that before correcting the background level for some galaxies and running the algorithm again, some galaxies showed even larger sbf gradients (which can be observed in Figure C.4).

5.4 Sbf colors and population models

As to place our results into the perspective of the predictive power of multi-band sbf measurements for constraining (secondary) stellar populations by Rodríguez-Beltrán et al. (2021), we plot the galaxies in various sbf color-color spaces in Figure 5.8. To compare the populated color space with the usual color space, we show mean colors from literature for each of our galaxies in Figure 5.9. As to place the results into the perspective of the work by Rodríguez-Beltrán et al. (2021), we also show their Figure 3 (Fig. 5.10 here). Although the filters in which we measure the sbf magnitude are different from the filters that Rodríguez-Beltrán et al. (2021) use, Figures 5.8 and 5.9 should give an indication of how sbf colors populate a vastly different color-space than mean colors.
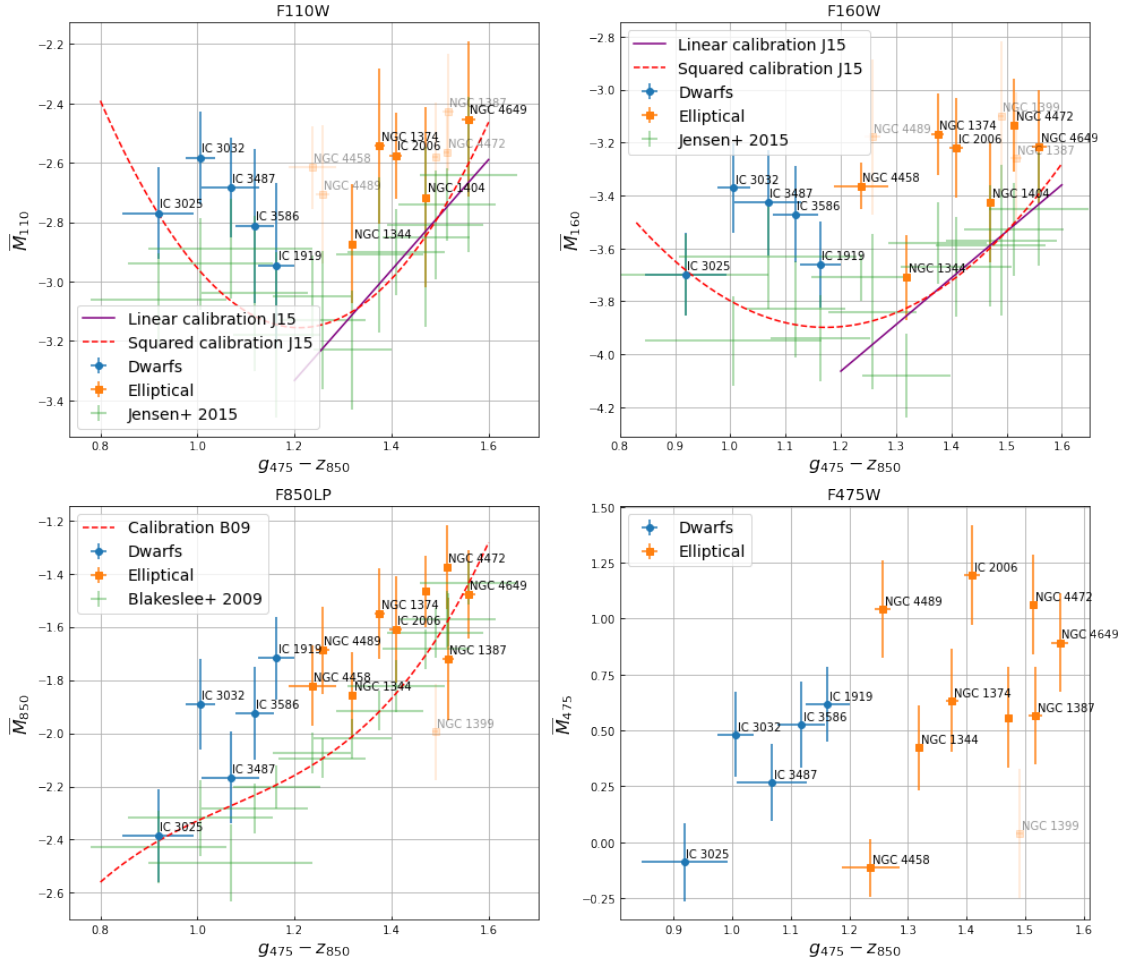
Figure 5.6: The $\overline{M}$ - color relation for each of the different filter bands analysed within this work. If available, calibrations by other works (Blakeslee et al., 2009; Jensen et al., 2015) are shown, together with the measurements of that work where the calibrations were based on. Dwarfs and ellipticals are indicated with the same colors and symbols as in other figures. The outliers are plot in faint colors, and are discussed in Section 6.1.

The following labels are not shown due to crowding of the plot: Top left: NGC 1399 (positioned next to IC 2006). Bottom left: NGC 1404 (positioned above NGC 1374). Bottom right: NGC 1404 (positioned next to NGC 1387).
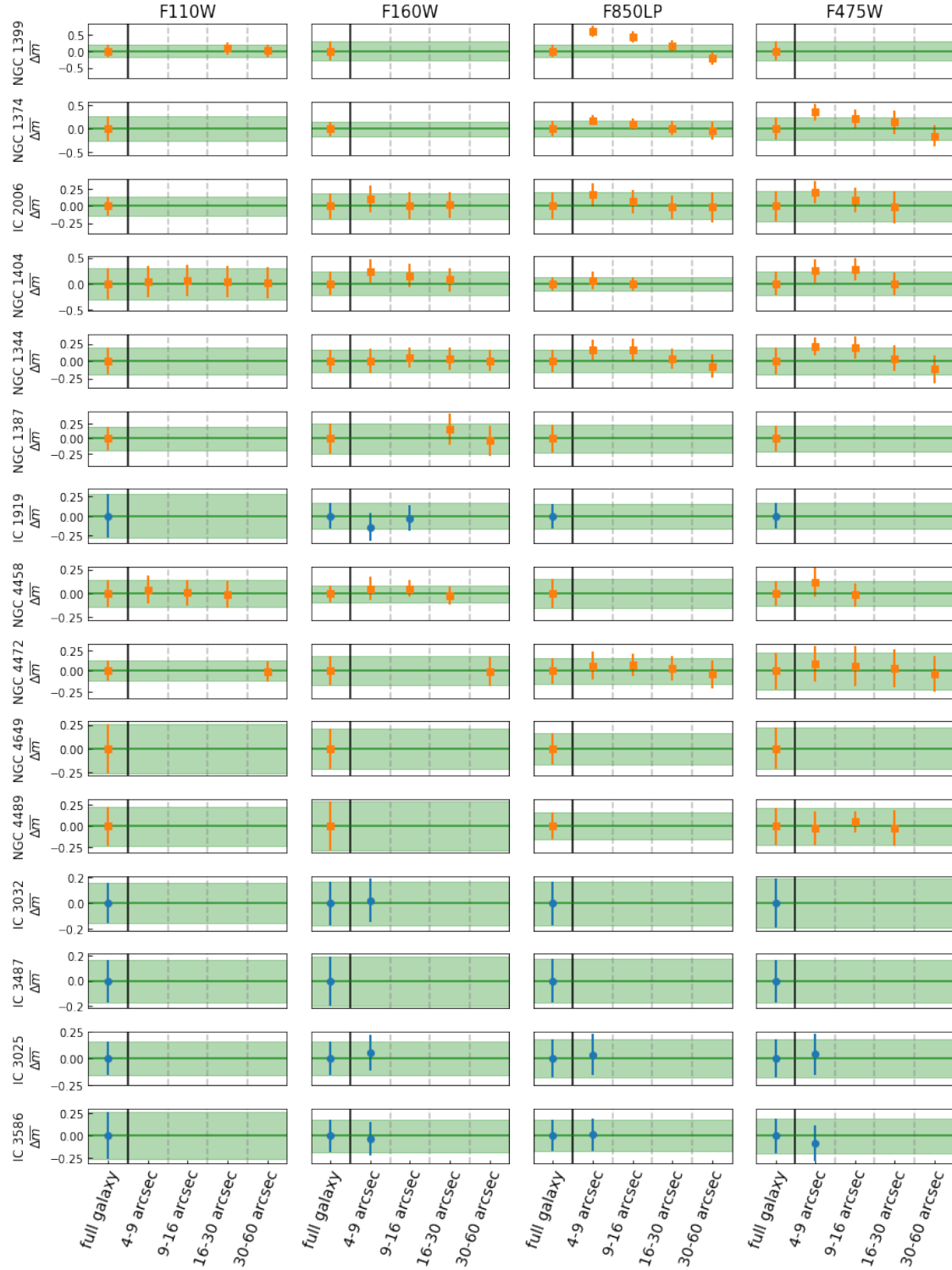
Figure 5.7: For each galaxy in our sample, we show the difference between the measured apparent sbf magnitude in the full galaxy and the magnitude measured in each annulus, given by $\Delta\overline{m}$. The hued beam indicates the uncertainty of the full galaxy measurement. The scale of the y-axis is the same for all filters in each individual galaxy, but differs between the galaxies. If an annulus does not show a data point, this means that the sbf magnitude could not be measured in this annulus. The galaxies are ordered as in Table 1. The dwarfs and ellipticals are shown in the same colors as in e.g. Figure 5.4
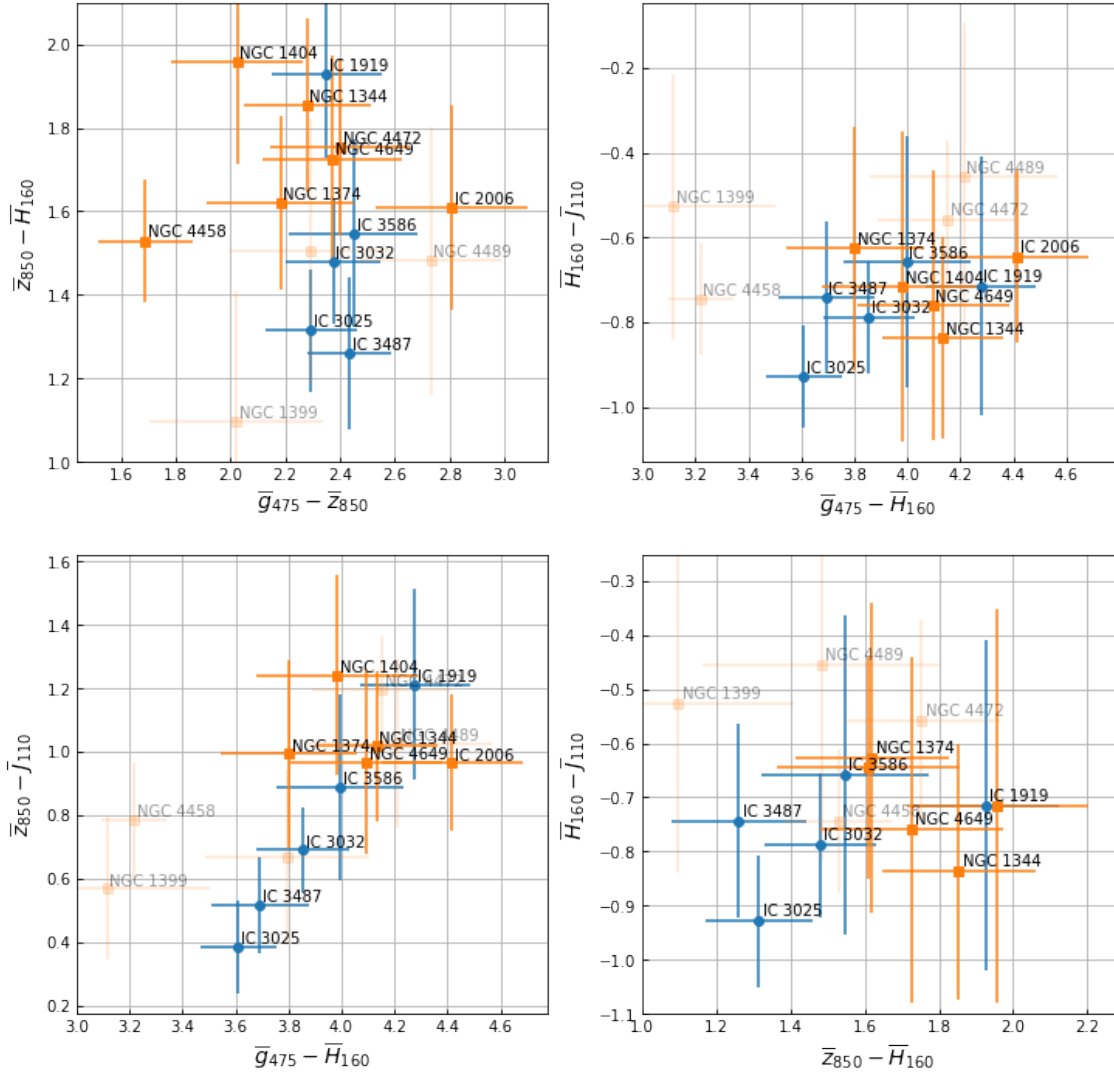
Figure 5.8: The SBF color-color relation for a range of SBF colors. We provide a number of different combinations of the different filters. The colors and markers are the same as for the Figures presented thus far. The outliers are shown fainter than the good quality measurements. The Figures should be representative of the sbf color-color space as presented by Rodríguez-Beltrán et al. (2021) in Figure 5.10.

The following labels are not shown due to crowding of the plot: Top left: NGC 1387 (positioned next to IC 23032). Bottom left: NGC 1387 (positioned next to IC 3032). Bottom right: NGC 1404 (positioned next to IC 1919) and IC 2006 (positioned between IC 3586 and NGC 1374).
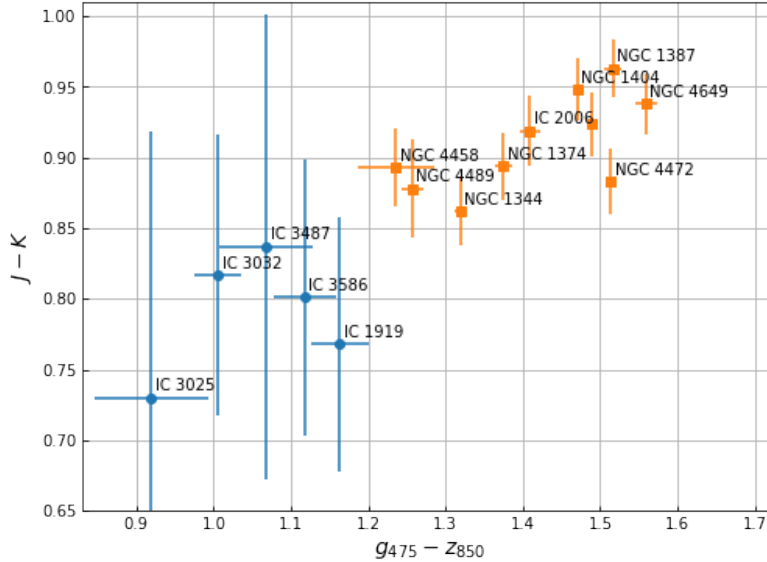
Figure 5.9: The mean $g_{475} - z_{850}$ color by Blakeslee et al. (2009) versus the $J - K$ colors from 2MASS (Skrutskie et al., 2006), for each galaxy in our sample. The label NGC 1399 is not shown; that galaxy is positioned next to IC 2006.

Comparing Figure 5.8 and Figure 5.9, we can infer that the sbf colors span very different range than the mean colors. Whereas the mean colors follow a clear and tight relation, the sbf colors populate a vastly different parameter space. Furthermore, employing various color combinations shows that even the combination of various sbf colors reveals different structures and hence might reveal potentially different information about the stellar populations.

If compared with Figure 5.10, we can infer that the different color spaces might indicate the potential to infer information about (secondary) stellar populations. The $\overline{g}_{475} - \overline{z}_{850}$ versus $\overline{z}_{850} - \overline{H}_{160}$ color-space (the top left frame in Figure 5.4) is the sbf color-space in our sample that comes most close to that in Figure 5.10. If we make a qualitative comparison, we can make the observation that younger, more metal poor populations (the dwarf galaxies) are located below the larger ellipticals, in a narrow $\overline{g}_{475} - \overline{z}_{850}$ range. The ellipticals seem to populate a more broad range in $\overline{g}_{475} - \overline{z}_{850}$ colors. Comparing with Figure 5.10, these elliptical galaxies would be placed in the region dominated by composite stellar populations (CSP) (the "grey" areas in Fig. 5.10). Hence, this might be an indication that some of the galaxies in our sample could contain composite stellar populations.

Although evidently, the employed colors in this work are different, the potential for stellar population studies becomes clear. A next, crucial step in this work would be to integrate the CSP models from Rodríguez-Beltrán et al. (2021) into the filters employed in this work, in order to learn what the exact stellar populations are that might be revealed.

6   Discussion

The methodology and the various results as presented in Section 4 and 5 provide sufficient cause for discussion. The various model choices and processing steps have resulted in an apparent systematic difference compared with literature for each filter band. Furthermore, the broad range of different galaxies analysed, including a number of dwarfs, give rise to a number of seemingly
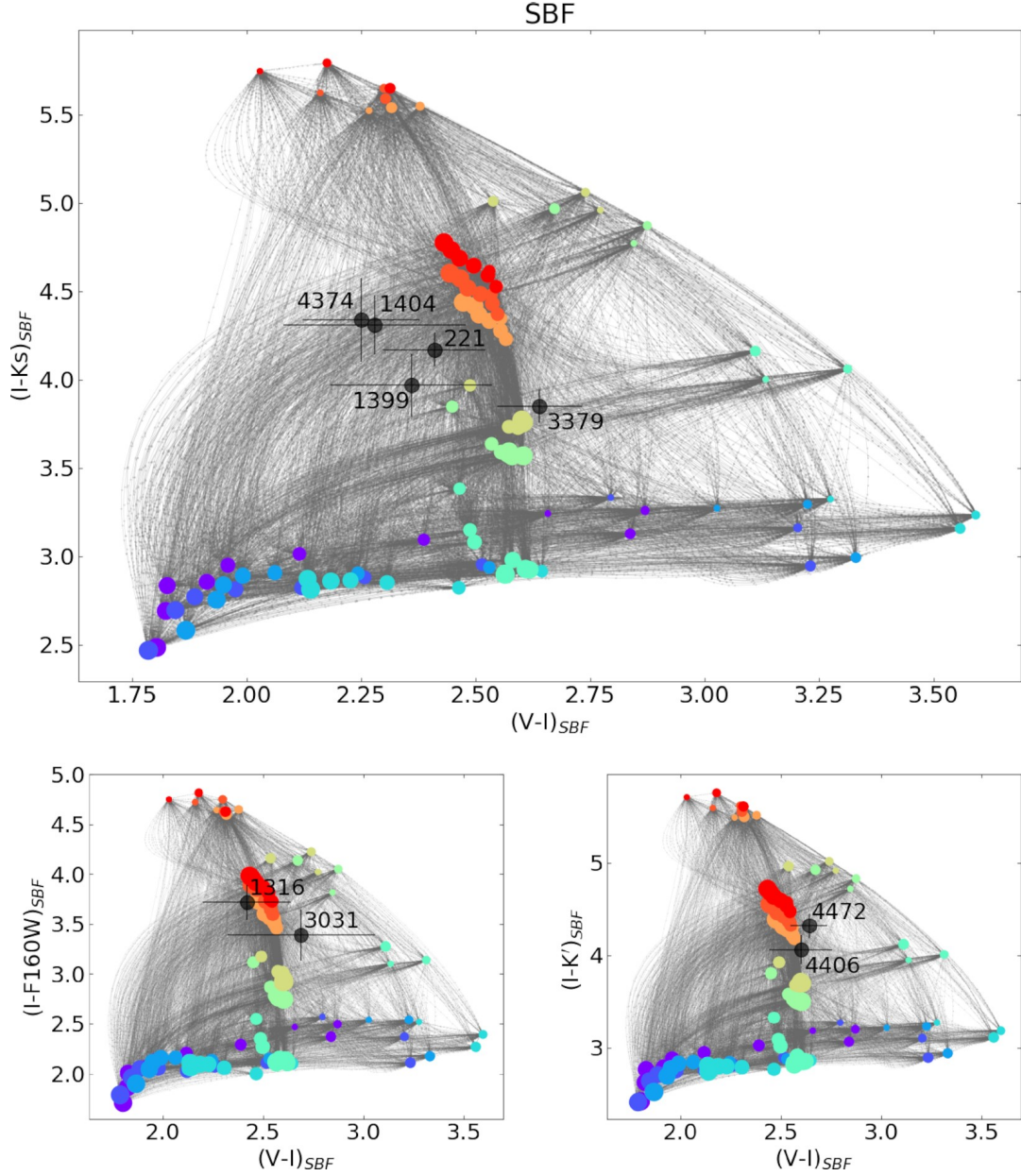
Figure 5.10: Figure 3 of Rodríguez-Beltrán et al. (2021). The dots correspond to single stellar populations, following a range of ages and metallicities. The color corresponds to the metallicity of the stellar population ([M/H] = -1.79 (purple) to [M/H] = 0.26 (red)). The size of the indicators indicates the age, ranging from 0.4 Gyr (smallest) to 14 Gyr (largest). The grey lines connecting all single stellar populations represent composite stellar populations, with varying mixing fractions. The data points are reference galaxies for which archival sbf measurements were available. The images indicate the sbf color-color space, with a different reference K band for for each frame. Rodríguez-Beltrán et al. (2021) show that galaxies populate the color-space dominated by single stellar populations when using mean colors (see their Fig 2, shown for reference here in Appendix D), while in SBF color space, these galaxies also populate the area in which the composite stellar populations exist.

Filter	median	mean	std	min	max
F110W	1.525	3.083	3.040	0.810	10.838
F160W	0.821	1.472	1.540	0.355	5.251
F850LP	0.054	0.068	0.071	-0.001	0.273
F475W	0.058	0.092	0.116	-0.000	0.427

Table 6: Summary of the estimated background levels in each filter band. We report the median background level over all galaxies, the mean, standard deviation, and the min and max values. The units are e^- s^{-1} pix^{-1}

outliers.

In Section 6.1 we will provide a brief discussion for each of the galaxies in our sample, discussing potential problems with the measurements that are not captured in the reported measurement uncertainties. We will also discuss whether it has been required to re-run the algorithm with an adjusted background level. For each of the galaxies, this should give an indication of the quality of the inferred sbf magnitude. If we deem the estimate inaccurate, we argue why the galaxy should be left out of the sample. This will be followed by a discussion of the implemented sbf measurement pipeline in general in Section 6.2. We discuss what this all means in view of the results for the stellar population models in Section 6.3.

6.1 Individual Galaxies

We will briefly discuss each of the galaxies in our sample to comment on potential peculiarities. For insight into the results for each galaxy, we refer to the images that are returned by the sbf pipeline, and have been stored on the online database[5]. For cases for which it is insightful to portray the images in this work, we will provide the figures in Appendix E.

To provide a reference about the shape and type of galaxy that we have analysed, we display each of the galaxies in the F850LP filter in Figure 6.1. We will address each galaxy in the order in which they are given in Table 1 except for IC 1919, which will be addressed together with the other dwarfs in Section 6.1.2. While discussing the galaxies, we learn that it is insightful to present a summary of the estimated background level B for each run, combined with the Sérsic indices. These are the background levels and corresponding Sérsic indices computed before re-running the algorithms with an adjusted background level for some galaxies. The background levels are reported in Table 6 and the Sérsic indices in Table 7.

6.1.1 Ellipticals

NGC 1399: While being the first galaxy addressed here, it is already a very interesting one. NGC 1399, the central galaxy in the Fornax cluster (e.g. Bílek et al., 2024), is relatively bright and should provide sufficient signal such that the sbf signal could be measured properly. At the same time, it is also one of the galaxies that exhibits the largest sbf gradients (Fig. 5.7). Comparing with sbf gradients for other ellipticals in e.g. Cantiello et al. (2005), we do know that we can expect sbf gradients to some extent, but the gradients for NGC 1399 seems to be overestimated. The only individual galaxy for which Blakeslee et al. (2009) explicitly display a sbf gradient is NGC 1399. They show that for the F850LP band the sbf gradient should cover approximately 0.4 magnitudes, which is lower than the value we infer.

When taking a deeper look into the measurements and the results intermediate results thereof, we cannot identify any noteworthy particularities. Taking a look into literature however, results in an interesting find regarding the Sérsic fit that was made in order to estimate the background level

---

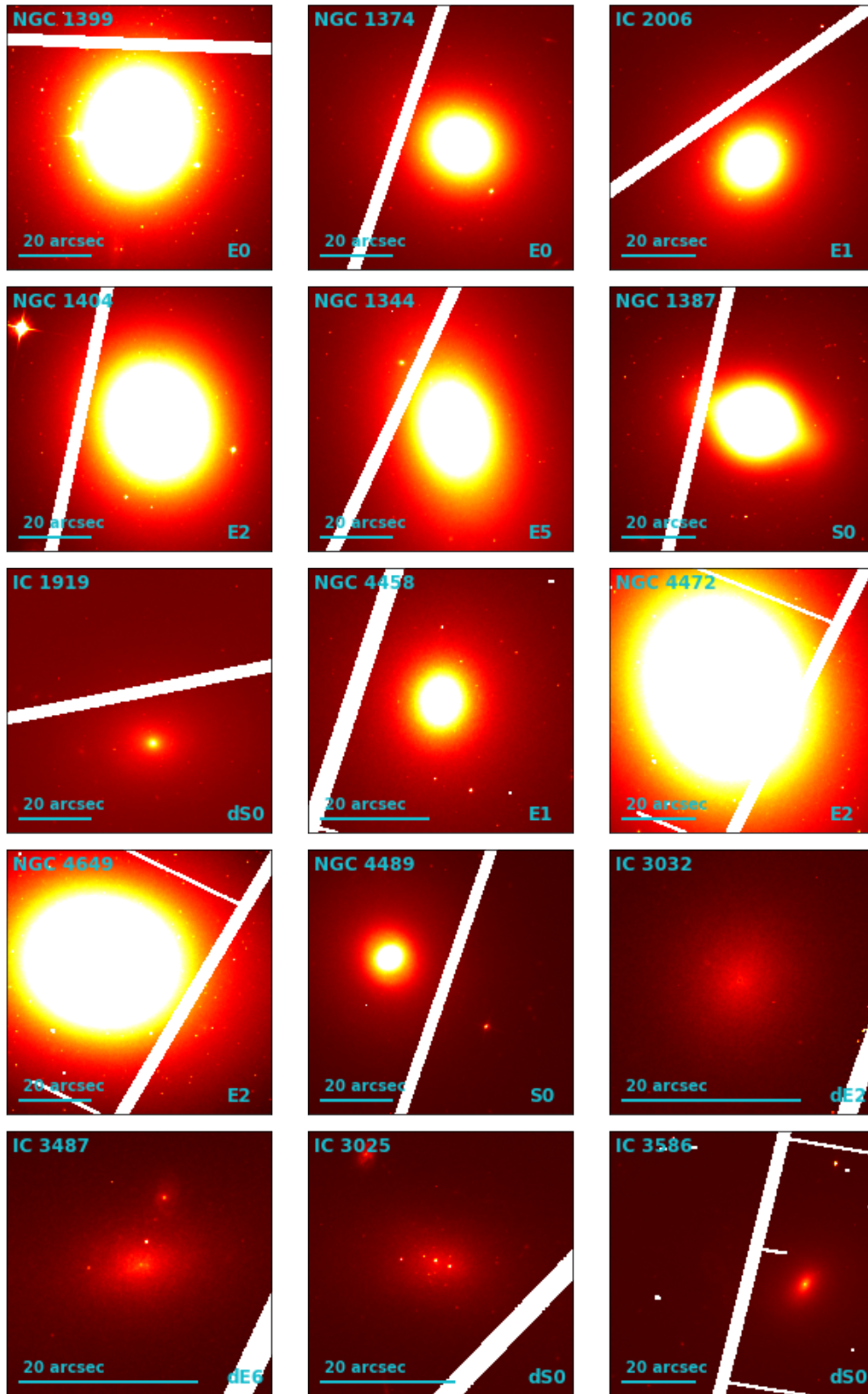[5]https://astrodrive.astro.rug.nl/index.php/s/Tg5yRlV5vKWcavg

Figure 6.1: The F850LP observations for each galaxy in the sample. The name is shown in the top left, the scale in the bottom left, and the galaxy classification as in Table 1 in the bottom right. The galaxies are scaled to the same intensity.

	F110W	F160W	F850LP	F475W
NGC 1399	2.63	3.37	1.98	1.95
NGC 1374	5.01	6.35	6.08	7.93
IC 2006	2.75	2.62	4.74	5.05
NGC 1404	2.43	2.47	2.24	2.25
NGC 1344	4.04	4.06	3.69	3.59
NGC 1387	2.10	6.98	2.88	2.92
IC 1919	1.23	1.61	5.47	5.38
NGC 4458	5.23	5.28	6.88	6.88
NGC 4472	3.35	3.16	2.17	2.10
NGC 4649	2.55	3.73	1.54	1.69
NGC 4489	6.52	13.76	. . .	. . .
IC 3032	1.37	0.96	0.85	0.91
IC 3487	1.65	1.52	1.22	1.39
IC 3025	. . .	1.48	1.33	1.30
IC 3586	3.65	3.52	2.24	1.86

Table 7: The Sérsic indices as measured when performing the Sérsic + background fit as explained in Section 4.2. We do not report uncertainties on these indices, as the indices have not been stored in the implementation of the pipeline. We simply report the index of the last iteration step. For NGC 4489 and IC 3025 the fitting algorithm was not able to converge, hence no background level is reported there.

of the observation from Section 4.2. The Sérsic indices that we find range from $n = 1.95$ in the F475W to $n = 3.37$ in the F160W band. When comparing to literature, Bílek et al. (2024) report a value of $n = 8.1$, while Graham & Driver (2007) even find a value of $n = 16.8$. Vaughan et al. (2018) report the extended halo in which NGC 1399 resides, indicating that often a fit is made of a Sérsic profile combined with one or more other components for the halo component. This large difference between our Sérsic index and that found in literature might indicate that the Sérsic + background fit made to determine the background level could result in an improper background estimate. Although the curve represents the elliprical annuli well, physically the value for B_{final} might actually overestimate the true background level.

If the subtracted background level is too high, this means that the isophotal model that we measure has a uniformly too low value. When scaling the residual fluctuations with the square root of the galaxy model, we will then scale with an uniformly too low value, which means that the amplitude of the sbf fluctuations is overestimated. This effect is larger towards the outskirts of the galaxy where the galaxy intensity is lower, as the ratio between the true intensity and the offset due to incorrect background subtraction is larger. This means that the sbf power in the nri towards the outskirts will be overestimated more than towards the center, leading to a gradient in resulting sbf amplitude. Thus, this indicates that an sbf gradient might actually be an indication of an incorrectly subtracted background level.

For this reason, we have including this galaxy in the re-run with adjusted background levels. This has lead to a reduction in the sbf gradient (comparing Fig. 5.7 and Fig. C.4), but still a significant gradient remains. Due to this unexpectedly large sbf gradient and the seeming offset from the relations in Figures 5.4 and 5.5, we decide to mark this observation as an outlier.

NGC 1374: This galaxy is one of the galaxies for which there seem to be little implications. There are some slight sbf gradients in the F475W band, which might potentially be an indication of an improper background estimate in this band, but this does not seem to be problematic. When comparing with literature in Figure 5.4 and 5.5, NGC 1374 also does not seem to be an outlier, and we have no reasons to assume that there are significant problems with this measurement other than the systematics that hold for each. We have not re-run the algorithm for this galaxy.

IC 2006: There seem to be no apparent issues for this galaxies in the infrared bands. However, when looking at the background level that was yielded after iteration of the Sérsic + background algorithm, we yield a slightly negative background level in the F475W band as well as in the F850LP band. Although the resulting background level is low ($-4 \cdot 10^{-5} \mathrm{e^- s^{-1}}$ for the F850LP and $-1.3 \cdot 10^{-3} \mathrm{e^- s^{-1}}$ for the F475W), this is clearly not physically correct. This is also shown in the resulting Sérsic index for those fits, which are higher in the visible bands than in the infrared bands. By e.g. Kelvin et al. (2012) and Häußler et al. (2013) we know that, also for elliptical galaxies, we should expect the Sérsic index to be increasing with wavelength, opposed to what we find for IC 2006.

However, we do not expect this incorrectly estimated background level to have a very significant effect on the measured sbf amplitude. The median background level in the F850LP and F475W is in the order of 0.05 $\mathrm{e^-}$ $\mathrm{s^{-1}}$ $\mathrm{pix^{-1}}$, which is in the order of 1% of the mean surface brightness profile. Hence, although the estimated background level is clearly physically incorrect, we still do deem the measured sbf magnitudes to be within the uncertainties for this galaxy.

NGC 1404: This galaxy is one of the galaxies that shows most consistent results in all bands, with appropriately estimated brightness profiles, consistent Sérsic indices and proper background levels. There are slight sbf gradients but these seem to be in line with scales that can be expected (e.g. Cantiello et al., 2005). However, a seemingly large background level compared to the mean level in the F110W band did lead us to re-do the measurement in this specific band.

NGC 1344: Also for NGC 1344 we obtain a very certain sbf fit with very little particularies, yielding in an sbf magnitude that we are fairly confident of. NGC 1344 also is one of the galaxies that yields results most in line with literature (e.g. Fig. 5.6). Cantiello et al. (2005) reports sbf gradients for NGC 1344 in the I-band, which are in line with the gradients found in Figure 5.7.

NGC 1387: This galaxy is peculiar in our sample as we came upon the available observations in the infrared bands by coincidence. This means that we cannot calibrate the sbf amplitude in these bands with Jensen et al. (2015). Furthermore, the observations for this galaxy have slightly different characteristics as compared to the other galaxies. Especially in the F110W, the observing time is approximately half as much as for the other galaxies.

The sbf is measured without significant implications in the F160W band, but for each of the other bands the measurements show serious limitations. There turns out to be a sprial structure at the center of the galaxy, which becomes apparent after subtracting the smooth model and normalising to create the nri. For reference we depict the nri for the F850LP band in Appendix E.1, Figure E.1 to show this structure.

We have re-run the algorithm for this galaxy and included a central mask to exclude the spiral structure in the center of the galaxy. This allows for a proper estimation of the sbf amplitude in the visible bands. In the infrared bands, residual structure unfortunately still remains after modelling the smooth surface brightness profile of the galaxy. In these bands, we hence still mark the measurement as not trustworty, and we have shown it as an outlier in the images from Section 5.

NGC 4458: Before re-running the algorithm with an adjusted background level, this galaxy seems to be a significant outlier in both infrared bands. Although performing better in the visible bands, the sbf power still seemed to be underestimated. A more detailed look into the measurement did, interestingly enough, not point out a certain problem. In all wavelength bands, the residual image as well as the luminosity function fit looked very clean. We did find the Sérsic indices for the visible bands to be higher than for the infrared bands as opposed to what we would expect (Kelvin et al., 2012; Häußler et al., 2013), but the estimated background level fell within one σ off the average for each band (Table 6). On the other hand, again a significant difference

with literature is found in the Sérsic index; Terzić & Graham (2005) find an index of $n = 2.6$, as opposed to values between $n = 5.23$ and $n = 6.88$ that we report. Since NGC 4458 is relatively faint (e.g. Morelli et al., 2004), the potential mis-fit of the Sérsic and background profile might result in the underestimation of the sbf magnitude. Therefore, we have decided to include this galaxy in the re-run with adjusted background levels.

The adjusted run does result in a better correspondence with literature values for most bands. However, for the F110W band the PSF is sampled very badly, showing significant fluctuations in the PSF power spectrum. Hence, we mark the measurement in this band as an outlier.

NGC 4472: This galaxy is one of the galaxies that on the first glance shows the best correspondence to values measured in literature in all bands. It is also one of the brightest galaxies in our sample. However, a more detailed look at the measurements learn that there are a number of inconsistencies. The estimated background level after fiting the Sérsic + background fit is very large, leading to the outliers for the F110W and F160W bands in background level in Table 6. This might be one of the causes of the relatively large sbf gradients in the F160W band that were observed for this galaxy (as explained in the discussion of NGC 1399, see Fig. C.4). In addition, the PSF in the F110W band is of very questionable quality, leading to an additional source of uncertainty in this band.

Rerunning the pipeline with an adjusted background level has lead to the measurement for this galaxy falling more in line with the other measurements. However, as the PSF is badly sampled in the F110W, we do also mark the measurement uncertain for NGC 4472 in this band.

NGC 4649: This is one of the galaxies with the brightest apparent magnitude in our sample. However, also for this galaxy the Sérsic + background model does not seems to describe the physical properties of the Sérsic profile and the background well, apparently largely overestimating the background level in the infrared wavelength bands when we compare the background level with those in Table 6. This does not seem to happen in the visibile bands. Rerunning the algorithm with adjusted background level in the infrared bands leads to a suitable measurement in those bands.

NGC 4489: This galaxy seems to be a significant outlier in the F160W band. A thorough look at the measurements learns that there is again a significant source of uncertainty in the estimate of the background level. In Table 6, we only report the Sérsic index for the final iteration in the Sérsic + background fit without uncertainties. For this galaxy however, the Sérsic index varies between $n = 8$ and $n = 14$ between iterations. Hence this galaxy is another example of the Sérsic + background model not representing the data well. For the infrared bands we find furthermore that the PSF is very improperly characterised, and even after averaging between individual PSF frames showing a significant variation in the radial power spectrum. Even after re-running the algorithm with the adjusted background level, the PSF has not been sampled well enough for this galaxy to provide a trustworthy measurement, hence we mark it as uncertain for the infrared bands.

For the visible bands, the background + noise model turns out not to be able to converge, and no Sérsic fit can be made. For this galaxy however, the initial background level B_0 falls well within the average for those bands (Table 6). Hence, we have run the algorithm with that background level. In these bands, this does not lead to reason to distrust the measurements, and we leave it in our sample.

6.1.2 Dwarfs

Dwarf galaxies are in general considered more difficult targets for measuring the sbf signal due to their more inconsistent stellar populations. Although these targets exhibit more intrinsic scatter in the relation between color and absolute sbf magnitude and hence are less suitable for distance

measurements, these galaxies might be suitable targets for the stellar population studies due to the ranging types of populations. This of course only holds, íf we can properly measure the sbf signal.

In the right frame of Figure 5.8 we can clearly see that the dwarf galaxies in our sample have much more blue colors than the larger ellipticals. Furthermore, in Figure 6.1 we can observe the galaxies to be much fainter, while also showing a more irregular structure. Besides this we can even see some star forming regions for some galaxies. A priori, we should be aware of these issues and treat the measurements with more care than compared to the larger galaxies.

IC 1919: This galaxy was one of the large outliers in Figure C.3. A more detailed look into the comparisons with literature learned that the largest offset for this galaxy seemed to lie in the F850LP band. Running the F850LP band for this galaxy with the adjusted background level solved the issue.

Koleva et al. (2011) measure a Sérsic index of $n = 2.17$ for this galaxy, while our indices range from 1.23 in the F110W to 5.43 in the F850LP. This is an indication that again, our background + Sérsic profile is not in correspondence with literature, which does again lead to inaccurate sbf estimates. Furthermore, we find that `ellipse` does not succeed in creating a smooth galaxy profile with no residual structure. The residual shows significant structure, partly due to younger populations and dust (shown in Appendix E.2, Fig. E.2) which does provide another root of uncertainty. We do not have radial sbf measurements for this galaxy in the visible bands due to our bound set on the number of unmasked pixels in each annulus. We would expect these to be present. Even though the residual structure left after subtracting the background level could be a cause of uncertainty, we expect this to be covered well enough by excluding the lowest and highest wavenumbers in the fit of the Fourier power spectrum. Therefore we leave the galaxy in our sample in all wavelength bands.

IC 3032: While being relatively faint, this is a dE2 type, showing a smooth elliptical profile and no apparent star-forming regions. In each of the individual bands, the measurement for this galaxy following the implemented pipeline does not show implications. Except for the additional intrinsic uncertainties due its blue color and the systematic uncertainties in the sbf measurement, there are no hidden problems for this galaxy.

IC 3487: despite a background spiral in the field of view (slightly noticeable in Figure 6.1) and some apparent star formation within the galaxy, the implemented pipeline is very well able to mask out these structures. Manually cutting out a smaller field of view did help the pipeline to properly process this galaxy. Similarly to IC 3032, there is no reason to assume hidden uncertainties other than the systematics.

IC 3025: This dwarf shows star forming regions in its profile, which we can identify in Figure 6.1. Still, except for the F110W band the implemented pipeline does not result in any significant problems. For the F110W band however, the model is not able to converge to a final background level, and after a number of iteration steps it fails due to an offset outer ellipse. However, the final estimated background level is very close to the median background level (Table 6). Since the background estimation failing automatically leads to a relatively large uncertainty on the background level, we do capture this within the reported uncertainties. Hence, we get to the same conclusion in all bands as for IC 3032 and IC 3487.

IC 3586: This galaxy is another one that shows a well characterised Sérsic + background fit, PSF, combined globular cluster and background galaxy luminosity function, and a smooth surface brightness model. The method yields some small residual structure in the F110W band, but this does not seem to lead to significant outliers.

6.2 Methodology

Following the discussion of the individual galaxies and the sbf measurements thereof, we find that the framework that has been implemented does still result in systematic effects in essentially each filter band. Although we have attempted to implement the individual measurement steps with great care, we point out a number of important considerations, would the framework be developed further.

6.2.1 Background level estimation

Although we have attempted to apply the framework as proposed by Jensen et al. (2015) and Jensen et al. (2021) for estimating the background level for each observation by iterating on the a fit of the radial surface brightness profile and converging to a background level, we have seen that this does result in final estimates for the Sérsic parameters that significantly deviate from literature (NGC 1399, NGC 4458, IC 1919) and some that show a Sérsic index behavior opposite to what we expect in literature (NGC 1374, IC 2006, IC 1919, NGC 4458, e.g. Kelvin et al. (2012); Häußler et al. (2013)). Although most of the observed galaxies are nearby and hence bright enough that the background level only is a small component of the total flux, we have seen that the background as a large effect on the quality of the results (clearly seen when comparing the results in Section 5 with those in Appendix C). The critical assumption that we have made to assume that the radial light profile can be described by a Sérsic + background model has clearly not been valid. Would the method be developed further, a more thorough model of the background level is crucial.

6.2.2 Smooth surface brightness model

Although the smooth surface brightness model does sometimes still result in residual structure being present within the residual image, the `ellipse` tool seems to work relatively well. It might be worthwhile to consider performing a secondary fit on the residual and assess whether this would aid in removing the residual structure. For now, this does however not seem to be one of the main issues that need to be addressed.

If the method would be extended to galaxies with different morphologies and more complex structures, then it should be considered to use other modelling tools such as `mgefit`, or as proposed by Foster et al. (2024), to consider bicubic spline models, or Gaussian smoothing kernels for the smooth profile fit. However this would also be something that would be addressed in a later stage.

6.2.3 Source mask

Evidently, a more robust procedure to set the thresholds for source detection while incorporating the noise due to the subtracted smooth model should be set in place. Although this is challenging, among others due to detailed literature on the matter being sparse, optimizing the procedure to mask sources would be required for extending the current implementation for galaxies that are located at a larger distance. Testing the current implementation to a number of galaxies in the sample of Jensen et al. (2021), we find the resulting source mask not to capture all background sources. Potentially, other methods for masking sources could be considered, such as MTObjects (Teeninga et al., 2016). These methodologies working in a different manner could make the masking procedure more intuitive. However, a more detailed study would be required to investigate this.

For the stellar population studies however, the current implementation could be left in place. If we would constrain our sample to relatively nearby galaxies such as in Fornax and Virgo, the current methodology works appropriately.

6.2.4 PSF

We have implemented a method to calculate the PSF profile using a number of different approaches. The difficulty and peculiarity in modelling the smooth profile stays apparent and the systematic difference in the sbf measurement using the library psf versus the empirical psf (Figures 5.2, 5.3, B.1) shows that the choice of PSF extraction methodology can be a large source of (systematic) uncertainty. For the ACS bands this issue is less problematic as we were able to extract smooth PSF profiles from a moderately crowded area in the globular cluster field NGC 0104, where the extracted psf seems to represent the shape of the sbf power spectrum very well for essentially all galaxies.

As pointed out as well by Jensen et al. (2015) and Jensen et al. (2021), the infrared bands are simply more problematic and sensitive due to the PSF being undersampled (e.g. Lauer, 1999) and the spatial variation in the PSF accross the detector (Anderson & Bedin, 2017). The resulting PSF power spectrum has depended on the library PSF measurements, but also here we are dependent on the quality of the stars in the field of view of each observation in the Dauphin et al. (2021) database. The quality of the stars observed in the days before and after the observation of the target galaxy, from which the library PSF cutouts are made, are not constant and vary over observations, as we have seen with NGC 4458 and NGC 4472. An alternative approach would be to only select PSF sources from the Dauphin et al. (2021) database that are of even higher quality, potentially spanning a larger period around the date that the observation was made. Then however it would become questionable how much the PSF would be affected by "breathing" of the instrument. Hence, the PSF in the infrared stays a source of uncertainty.

6.2.5 Drizzling and Fourier fit

Although we have argued in Section 5.1.1 that using the drizzled files compared to overlapping the flat-fielded files does not matter much for the final measured sbf magnitude, we are aware that would the method be developed further, a more detailed understanding of the properties of the correlated noise components in the drizzled frames would be desired. An analysis as proposed in Mei et al. (2005a) could provide an indication of the wavenumbers at which the background power spectrum start to be correlated and hence should be excluded from the fit. For now, the Fourier fit, and especially the wavenumbers k^- and k^+ between which we apply the fit, are still a potential source of systematic uncertainty.

The procedure implemented here has been tested and seems to give a suitable mean sbf magnitude, but alternative methods such as a Monte Carlo approach with randomization of the initial and final wave numbers (Carlsten et al., 2019b) has not been tested. Alternatively an approach in which the fit is made for a range of different wave numbers and taking the value for which the resulting P_0 reaches a plateau (e.g. Cantiello et al., 2013, 2018b) could also be explored. For now, this step stays a potential source of uncertainty.

6.2.6 Remaining uncertainties

Even when addressing all of the steps above, some potential unexplored uncertainties remain. For example, we have simply added the uncertainties of the individual components in quadrature in Equation 4.37, but evidently some of these are correlated. Furthermore, as pointed out by Rodríguez-Beltrán et al. (2024), there remains a stochastic uncertainty in the sbf magnitude, purely due to the stochastisity of the sbf fluctuations within the measured aperture. They show that even keeping the aperture and sbf magnitude fixed, different realisations of the same galaxy following a Monte Carlo approach, leads to another component of uncertainty, that is often excluded in empirical sbf calculations.

Lastly we want to express on the methodology that we have explicitly attempted to approach the implementation of the methodology as independently as possible to previous works. This has

been done partly as a means to validate results of previous works, and to actively explore the effect of underlying model choices that need to be made. Although we have combined components of the measurement procedure as described by a range of works, we have also shown that evident systematic uncertainties remain. Although we could have attempted to tweak our parameters in the method as to reduce the systematics, we have as much as possible attempted to approach each individual component as a problem of its own. This does yield an evident systematic offset, for which evidently more work on the method is required to investigate the source thereof, but does result in as independent results as possible.

6.3   Sbf colors

The main result in this work shows the behaviour of different sbf colors as compared with the mean-colors parameter space. Placing the result in the context Rodríguez-Beltrán et al. (2021), we can see that clearly, the sbf colors populate a different color space than the mean colors, which could indicate a potential source of information about the stellar populations. The next step herein would be to integrate the CSP models that are presented by Rodríguez-Beltrán et al. (2021) into the filters employed in this work. We would then be able to quantise whether different populations can truly be uncovered.

Taking a last look at Figure 5.8 and Figure 5.10, we can draw the cautious conclusions that the ellipticals seem to populate a slightly broader range of sbf colors, which might be an indication that various kinds of secondary populations might exist within these galaxies. The dwarfs are situated more closely to each other. However, these statements should be interpreted with great care as the parameter space of the underlying populations are not characterised in the investigated color space. The conclusion that the sbf color-space reveals potential undiscovered information can however be drawn.

We want to state that although systematic uncertainties on the measured sbf magnitudes remain, the offsets could be corrected by a fixed shift of the magnitude $\overline{m}$ to obtain the results found in literature. In color-space, these systematics would also correspond to a fixed shift, but it would not lead to differences in the structures that are observed. Hence, the conclusions that were drawn based on these graphs would not be vastly different.

7   Conclusion

In this work we have provided a new, independent implementation for the sbf method. We have explored the model choices that need to be made in order to be able to measure the sbf amplitude, and we have seen how small changes in the method can have a large effect on the measured sbf amplitude. The method turns out to be challenging to implement due to the various components that need to work together, and the vast number of parameter choices that need to be made. Great care is required to deduct the suitable model choices.

With the current implementation it is possible to measure the sbf magnitude for elliptical (dwarf) galaxies that are not significantly affected by dust. However, a systematic difference with the literature remains. Further investigation in the implementation of the method is required to improve the results, in which many components such as the estimate of the background model, a quantification of the correlated noise components of the drizzled frames and its effect on the fit of the Fourier power spectrum, and a more thorough model of the PSF are should be reconsidered.

Instead of attempting to reach outward as far as possible and use sbf to be able to infer distances to galaxies, we have provided an attempt to work the other way around, and use the dependence of the sbf signal on the underlying stellar population to learn something about this stellar population. As Rodríguez-Beltrán et al. (2021) has shown, galaxies populate a vastly dif-

ferent parameter space in sbf color-color space than compared to mean color-color space. We confirm this by measuring the sbf magnitude in four different HST bands for a number of galaxies in the Virgo and Fornax cluster. We show how various sbf color spaces show a different distribution of the sampled galaxies. This is an indication that the populations that make up these galaxies are not uniform, and that there might potentially be hidden secondary stellar populations.

We cannot set stringent constraints on the populations that make up these galaxies. This would require integrating the composite stellar populations that are presented by Rodríguez-Beltrán et al. (2021) into the filters that were employed in this work. Besides further refinement of the implemented sbf measurement procedure, this would be a next step in the continuation of this work.

References

Ajhar E. A., Lauer T. R., Tonry J. L., Blakeslee J. P., Dressler A., Holtzman J. A., Postman M., 1997, Astronomical Journal, 114, 626

Anderson J., 2022, One-Pass HST Photometry with hst1pass, Instrument Science Report ACS 2022-02

Anderson J., Bedin L. R., 2017, Monthly Notices of the Royal Astronomical Society, 470, 948

Barbary K., 2016, The Journal of Open Source Software, 1, 58

Benítez N., et al., 2004, Astrophysical Journal, Supplement, 150, 1

Bertin E., Arnouts S., 1996, A&AS, 117, 393

Bílek M., Hilker M., Renaud F., Richtler T., Chaturvedi A., Samurović S., 2024, Astronomy and Astrophysics, 682, A111

Binggeli B., Sandage A., Tammann G. A., 1985, Astronomical Journal, 90, 1681

Binggeli B., Tammann G. A., Sandage A., 1987, Astronomical Journal, 94, 251

Biscardi I., Raimondo G., Cantiello M., Brocato E., 2008, Astrophysical Journal, 678, 168

Blakeslee J. P., 2012, Ap&SS, 341, 179

Blakeslee J. P., Cantiello M., 2018, Research Notes of the American Astronomical Society, 2, 146

Blakeslee J. P., Tonry J. L., 1995, Astrophysical Journal, 442, 579

Blakeslee J. P., Vazdekis A., Ajhar E. A., 2001, Monthly Notices of the Royal Astronomical Society, 320, 193

Blakeslee J. P., Lucey J. R., Tonry J. L., Hudson M. J., Narayanan V. K., Barris B. J., 2002, Monthly Notices of the Royal Astronomical Society, 330, 443

Blakeslee J. P., et al., 2009, Astrophysical Journal, 694, 556

Blakeslee J. P., et al., 2010, Astrophysical Journal, 724, 657

Blakeslee J. P., Jensen J. B., Ma C.-P., Milne P. A., Greene J. E., 2021, Astrophysical Journal, 911, 65

Bradley L., et al., 2020, astropy/photutils: 1.0.0, doi:10.5281/zenodo.4044744

Buzzoni A., 1993, Astronomy and Astrophysics, 275, 433

Cantiello M., Blakeslee J. P., 2023, arXiv e-prints, p. arXiv:2307.03116

Cantiello M., Raimondo G., Brocato E., Capaccioli M., 2003, Astronomical Journal, 125, 2783

Cantiello M., Blakeslee J. P., Raimondo G., Mei S., Brocato E., Capaccioli M., 2005, Astrophysical Journal, 634, 239

Cantiello M., et al., 2013, Astronomy and Astrophysics, 552, A106

Cantiello M., et al., 2018a, Astrophysical Journal, Letters, 854, L31

Cantiello M., et al., 2018b, Astrophysical Journal, 856, 126

Cantiello M., et al., 2024, Astrophysical Journal, 966, 145

Cappellari M., 2002, Monthly Notices of the Royal Astronomical Society, 333, 400

Carlsten S. G., Beaton R. L., Greco J. P., Greene J. E., 2019a, Astrophysical Journal, Letters, 878, L16

Carlsten S. G., Beaton R. L., Greco J. P., Greene J. E., 2019b, Astrophysical Journal, 879, 13

Carlsten S. G., Greco J. P., Beaton R. L., Greene J. E., 2020, Astrophysical Journal, 891, 144

Carlsten S. G., Greene J. E., Peter A. H. G., Beaton R. L., Greco J. P., 2021, Astrophysical Journal, 908, 109

Carlsten S. G., Greene J. E., Beaton R. L., Danieli S., Greco J. P., 2022, Astrophysical Journal, 933, 47

Cohen Y., et al., 2018, Astrophysical Journal, 868, 96

Côté P., et al., 2004, Astrophysical Journal, Supplement, 153, 223

Dauphin F., Anderson J., Bajaj V., Dressel L., Sahu K., Bourque M., Shanahan C., 2021, The WFPC2 and WFC3 PSF Database, Instrument Science Report WFC3 2021-12

Dressel L., 2015, in , Vol. 7, WFC3 Instrument Handbook for Cycle 23 v. 7. p. 7

Erwin P., 2015, Astrophysical Journal, 799, 226

Ferguson H. C., 1989, Astronomical Journal, 98, 367

Ferrarese L., et al., 2012, Astrophysical Journal, Supplement, 200, 4

Foster L. M., Taylor J. E., Blakeslee J. P., 2024, Monthly Notices of the Royal Astronomical Society, 527, 1656

Freedman W. L., et al., 2001, Astrophysical Journal, 553, 47

Fruchter A. S., Hook R. N., 2002, PASP, 114, 144

Garnavich P., et al., 2023, Astrophysical Journal, 953, 35

Gilmozzi R., Spyromilio J., 2007, The Messenger, 127, 11

Gonzaga S., Hack W., Fruchter A., Mack J., 2012, The DrizzlePac Handbook

Goullaud C. F., Jensen J. B., Blakeslee J. P., Ma C.-P., Greene J. E., Thomas J., 2018, Astrophysical Journal, 856, 11

Graham A. W., Driver S. P., 2005, PASA, 22, 118

Graham A. W., Driver S. P., 2007, Astrophysical Journal, 655, 77

Greco J. P., van Dokkum P., Danieli S., Carlsten S. G., Conroy C., 2021, Astrophysical Journal, 908, 24

Greisen E. W., Calabretta M. R., Valdes F. G., Allen S. L., 2006, Astronomy and Astrophysics, 446, 747

Häußler B., et al., 2013, Monthly Notices of the Royal Astronomical Society, 430, 330

Jedrzejewski R. I., 1987, Monthly Notices of the Royal Astronomical Society, 226, 747

Jensen J. B., Tonry J. L., Thompson R. I., Ajhar E. A., Lauer T. R., Rieke M. J., Postman M., Liu M. C., 2001, Astrophysical Journal, 550, 503

Jensen J. B., Tonry J. L., Barris B. J., Thompson R. I., Liu M. C., Rieke M. J., Ajhar E. A., Blakeslee J. P., 2003, Astrophysical Journal, 583, 712

Jensen J. B., Blakeslee J. P., Gibson Z., Lee H.-c., Cantiello M., Raimondo G., Boyer N., Cho H., 2015, Astrophysical Journal, 808, 91

Jensen J. B., et al., 2021, Astrophysical Journal, Supplement, 255, 21

Jordán A., et al., 2004, Astrophysical Journal, Supplement, 154, 509

Jordán A., et al., 2007, Astrophysical Journal, Supplement, 169, 213

Kelvin L. S., et al., 2012, Monthly Notices of the Royal Astronomical Society, 421, 1007

Khetan N., et al., 2021, Astronomy and Astrophysics, 647, A72

Kim Y. J., Lee M. G., 2021, Astrophysical Journal, 923, 152

Kim Y. J., Kang J., Lee M. G., Jang I. S., 2022, Astrophysical Journal, 929, 36

Koleva M., Prugniel P., De Rijcke S., Zeilinger W. W., 2011, Monthly Notices of the Royal Astronomical Society, 417, 1643

Krist J. E., Hook R. N., Stoehr F., 2011, in Kahan M. A., ed., Society of Photo-Optical Instrumentation Engineers (SPIE) Conference Series Vol. 8127, Optical Modeling and Performance Predictions V. p. 81270J, doi:10.1117/12.892762

Lauer T. R., 1999, PASP, 111, 1434

Mei S., et al., 2005a, Astrophysical Journal, Supplement, 156, 113

Mei S., et al., 2005b, Astrophysical Journal, 625, 121

Mei S., et al., 2007, Astrophysical Journal, 655, 144

Mieske S., Hilker M., 2003, Astronomy and Astrophysics, 410, 445

Mieske S., Hilker M., Infante L., 2005, Astronomy and Astrophysics, 438, 103

Mieske S., Hilker M., Infante L., 2006, Astronomy and Astrophysics, 458, 1013

Mitzkus M., Walcher C. J., Roth M. M., Coelho P. R. T., Cioni M.-R. L., Raimondo G., Rejkuba M., 2018, Monthly Notices of the Royal Astronomical Society, 480, 629

Morelli L., et al., 2004, Monthly Notices of the Royal Astronomical Society, 354, 753

Moresco M., et al., 2022, Living Reviews in Relativity, 25, 6

Mould J., Sakai S., 2009, Astrophysical Journal, 694, 1331

Nantais J. B., Huchra J. P., Barmby P., Olsen K. A. G., Jarrett T. H., 2006, Astronomical Journal, 131, 1416

Pahre M. A., et al., 1999, Astrophysical Journal, 515, 79

Polzin A., van Dokkum P., Danieli S., Greco J. P., Romanowsky A. J., 2021, Astrophysical Journal, Letters, 914, L23

Rodríguez-Beltrán P., Vazdekis A., Cerviño M., Beasley M. A., 2021, Monthly Notices of the Royal Astronomical Society, 507, 3005

Rodríguez-Beltrán P., Cerviño M., Vazdekis A., Beasley M. A., 2024, Astronomy and Astrophysics, 686, A62

Sérsic J. L., 1963, Boletin de la Asociacion Argentina de Astronomia La Plata Argentina, 6, 41

Sérsic J. L., 1968, Atlas de Galaxias Australes

Sirianni M., et al., 2005, PASP, 117, 1049

Skrutskie M. F., et al., 2006, Astronomical Journal, 131, 1163

Stetson P. B., 1987, PASP, 99, 191

Teeninga P., Moschini U., Trager S. C., Wilkinson M. H., 2016, Mathematical Morphology - Theory and Applications, 1

Terzić B., Graham A. W., 2005, Monthly Notices of the Royal Astronomical Society, 362, 197

Tonry J., Schneider D. P., 1988, Astronomical Journal, 96, 807

Tonry J. L., Ajhar E. A., Luppino G. A., 1990, Astronomical Journal, 100, 1416

Tonry J. L., Blakeslee J. P., Ajhar E. A., Dressler A., 1997, Astrophysical Journal, 475, 399

Tonry J. L., Dressler A., Blakeslee J. P., Ajhar E. A., Fletcher A. B., Luppino G. A., Metzger M. R., Moore C. B., 2001, Astrophysical Journal, 546, 681

Uddin S. A., et al., 2023, arXiv e-prints, p. arXiv:2308.01875

Van Dokkum P. G., 2001, PASP, 113, 1420

Van Dokkum P., Danieli S., Cohen Y., Romanowsky A. J., Conroy C., 2018, Astrophysical Journal, Letters, 864, L18

Vaughan S. P., Davies R. L., Zieleniewski S., Houghton R. C. W., 2018, Monthly Notices of the Royal Astronomical Society, 479, 2443

Vazdekis A., Cerviño M., Montes M., Martín-Navarro I., Beasley M. A., 2020, Monthly Notices of the Royal Astronomical Society, 493, 5131

Virtanen P., et al., 2020, Nature Methods, 17, 261

Worthey G., 1993, Astrophysical Journal, 409, 530

Worthey G., 1994, Astrophysical Journal, Supplement, 95, 107

A   Appendix

A.1   Background level estimation
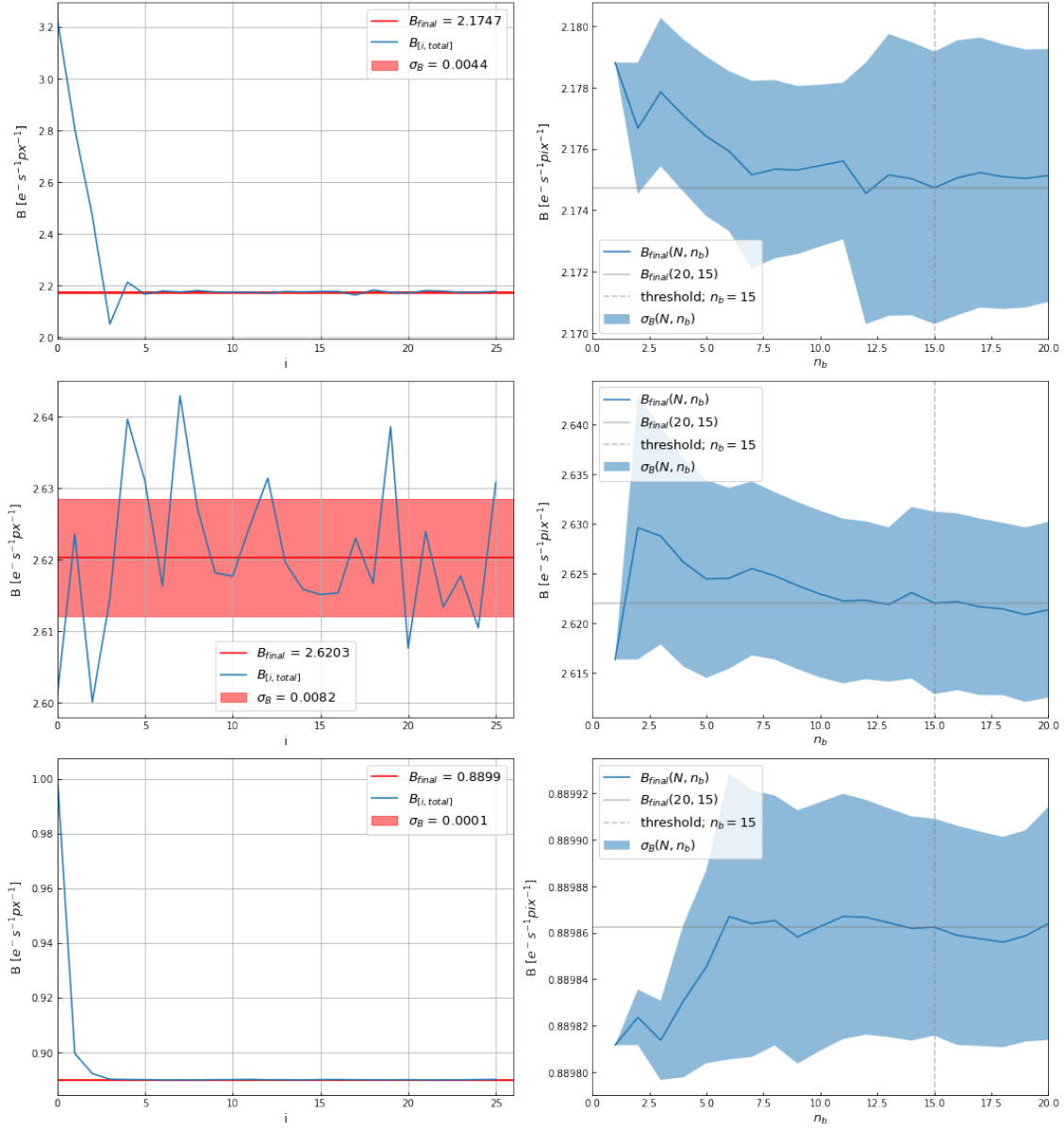
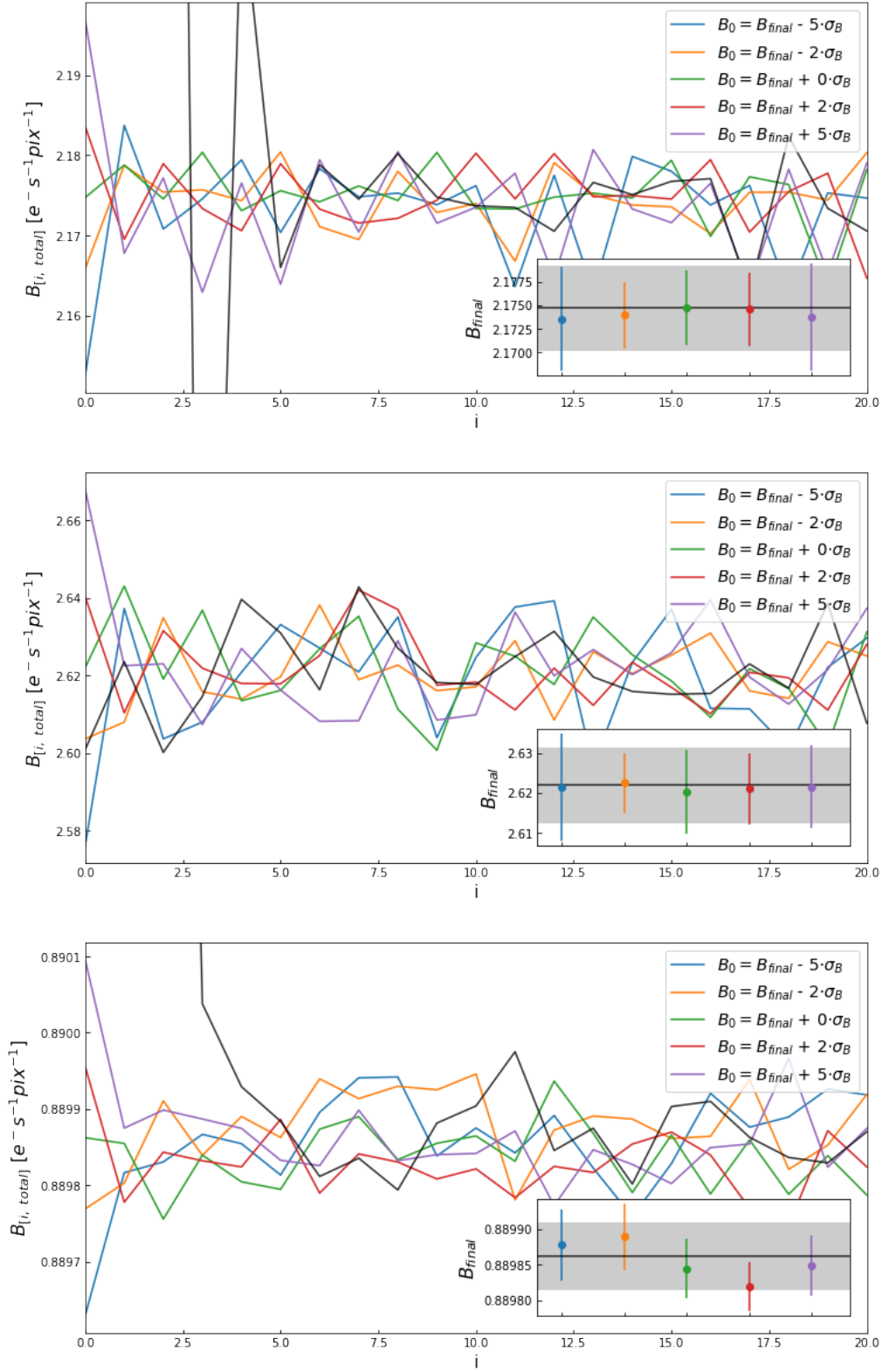Figure A.1: Development of background level as in Figure 4.3, from top to bottom for NGC 0533, NGC 4073, NGC 4914.

Figure A.2: Development of $B_{[i,\ total]}$ as a function of iteration step i for different background values B_0. Same as in Figure 4.4. From top to bottom the iterations correspond to respectively NGC 0533, NGC 4073, NGC 4914.

B   Further results

In this Appendix we will give some further results that are not mentioned in the results section, Section 5. This Appendix will consist mainly of additional figures.

B.1   F475W empirical PSF against library PSF
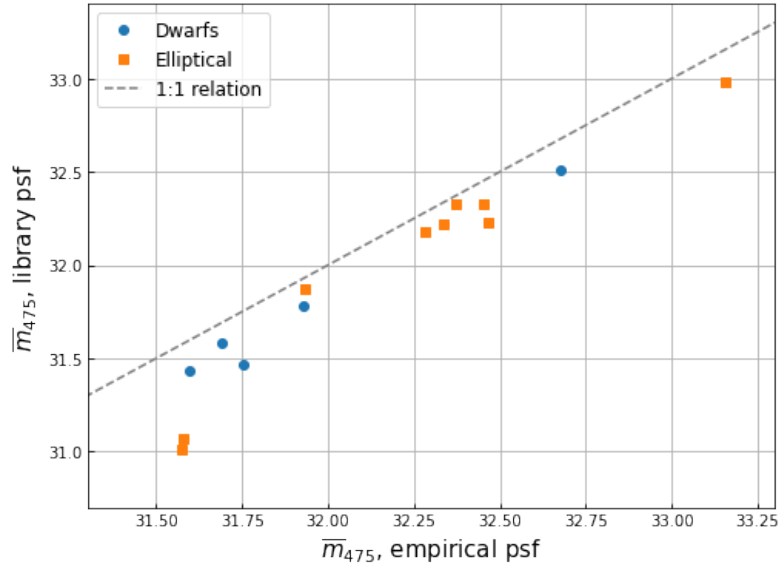
Figure B.1: The apparent sbf mmagnitude measured with the empirical psf as compared to the library psf as in Figure 5.2, but now for the F475W filter band.

C Results with outliers

This Appendix presents the results as given in Section 5 but without the adjustment made to account for the incorrectly estimated background level. The outliers are presented in faint colors in all images.
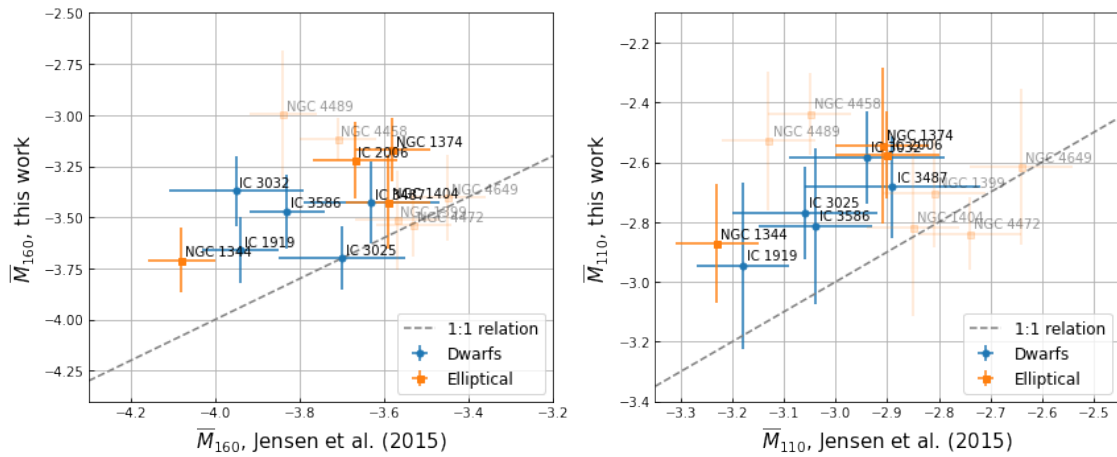
Figure C.1: Same as Figure 5.4, but with the outliers due to incorrect background subtraction indicated faint.
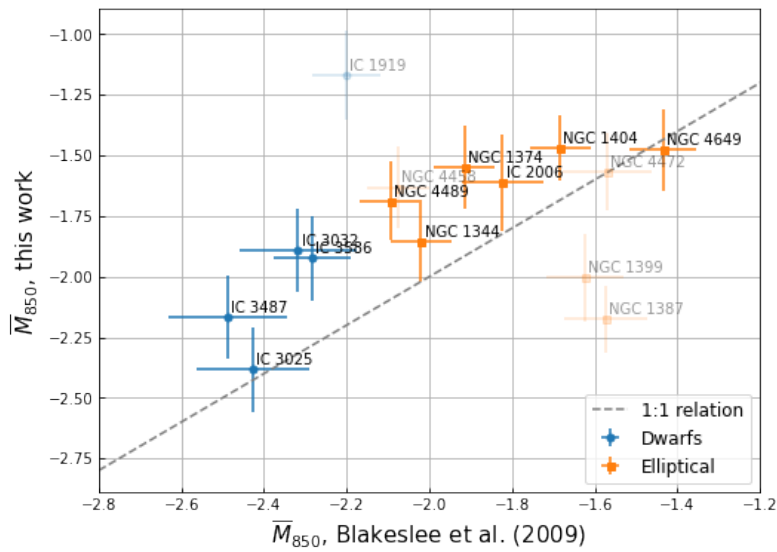
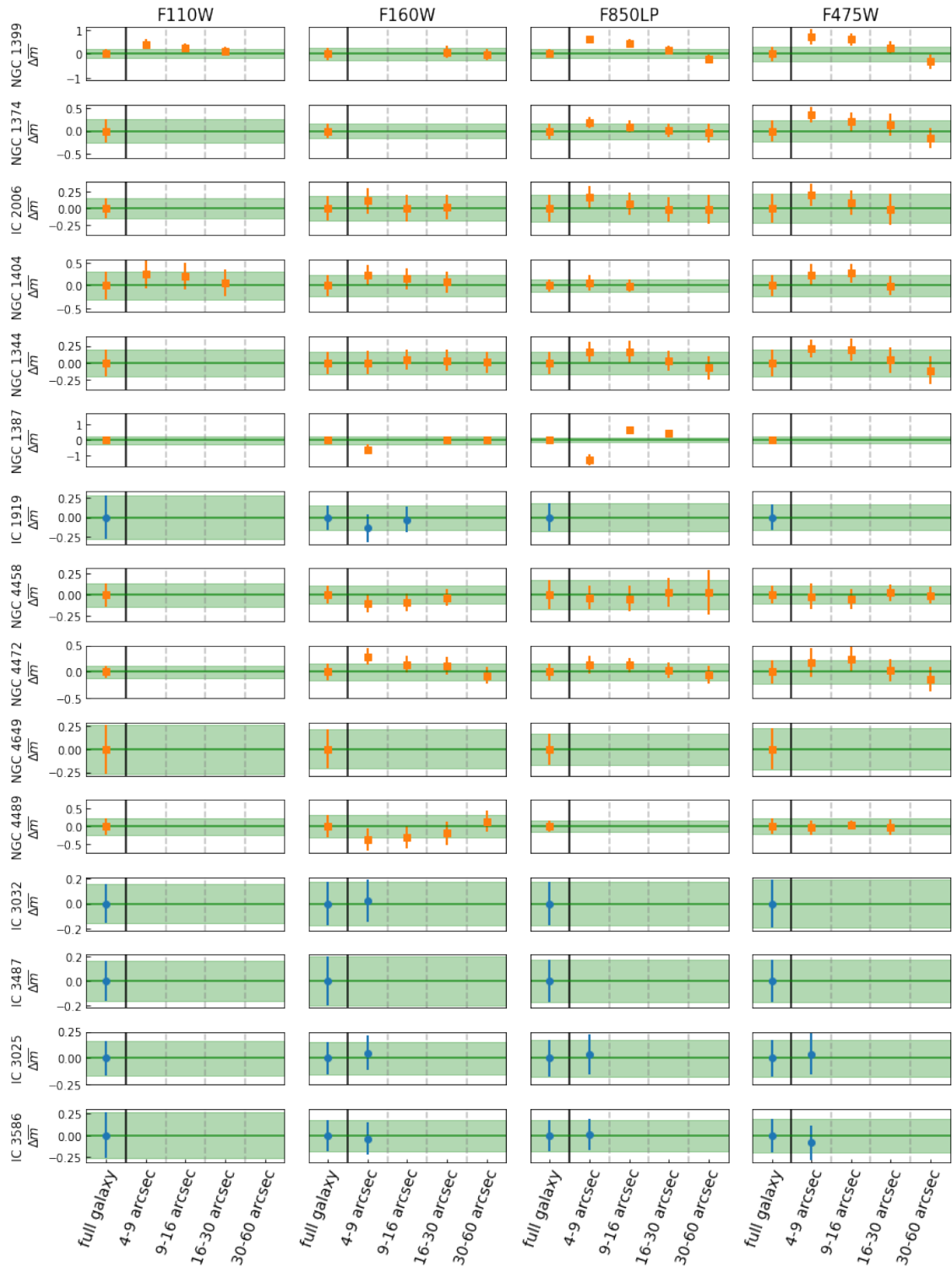Figure C.2: Same as Figure 5.5, but with the outliers due to incorrect background subtraction indicated faint.
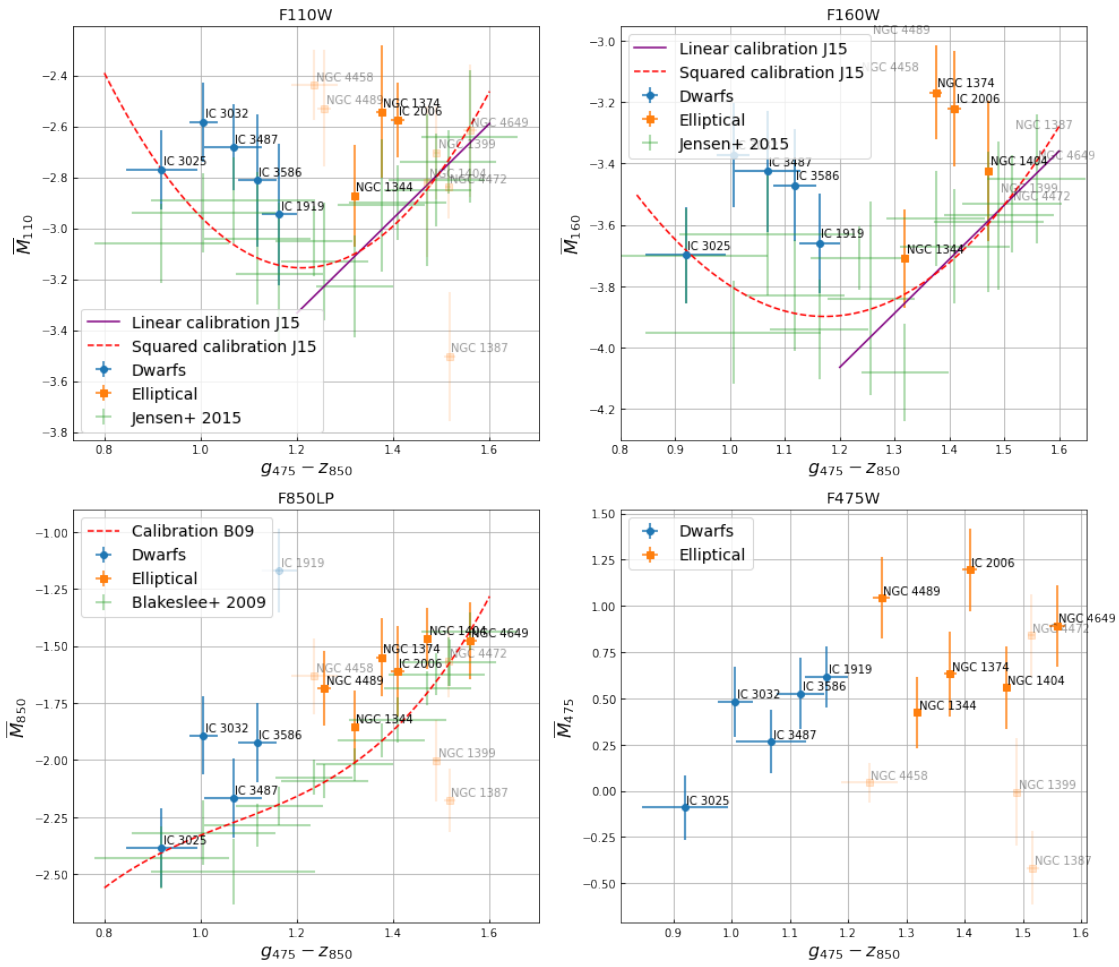
Figure C.3: Same as Figure 5.6, but with the outliers due to incorrect background subtraction indicated faint.

Figure C.4: Same as Figure 5.7, but without accounting for the outliers due to incorrect background subtraction.
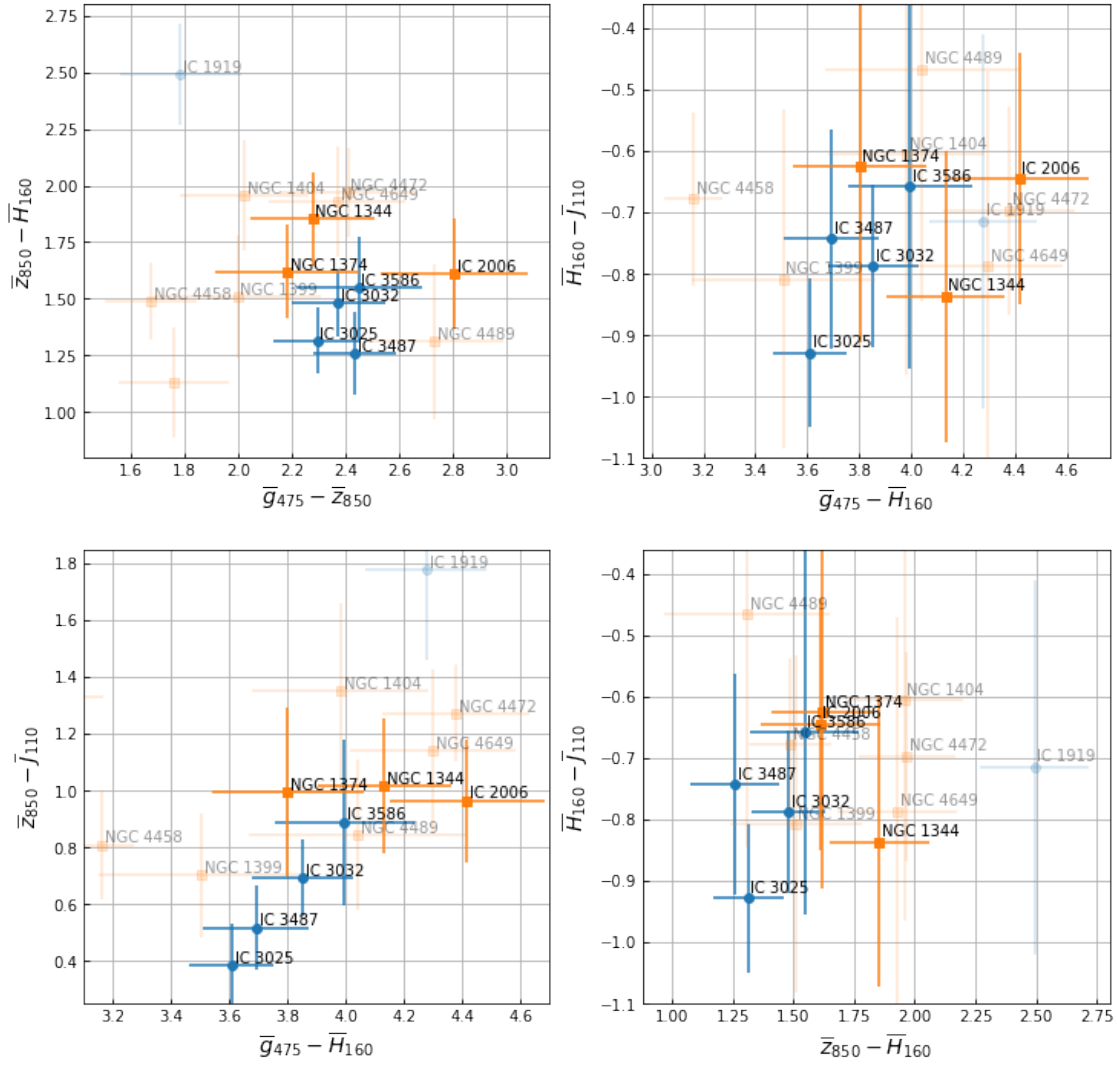
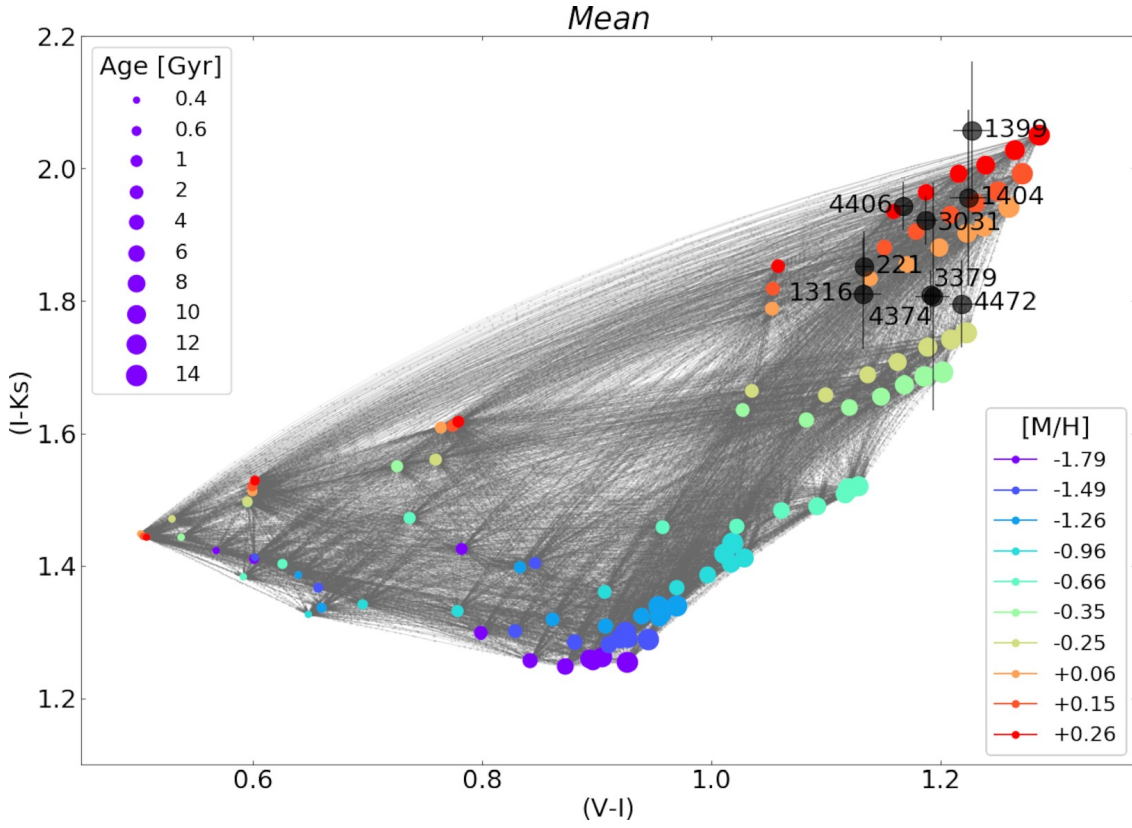Figure C.5: Same as Figure 5.8, but without accounting for the outliers due to incorrect background subtraction.

Figure D.1: Figure 2 of Rodríguez-Beltrán et al. (2021).

E Peculiar galaxies

In this Appendix we will show the figures for some galaxies that give peculiar results. These Figures are referred to in Section 6.1.
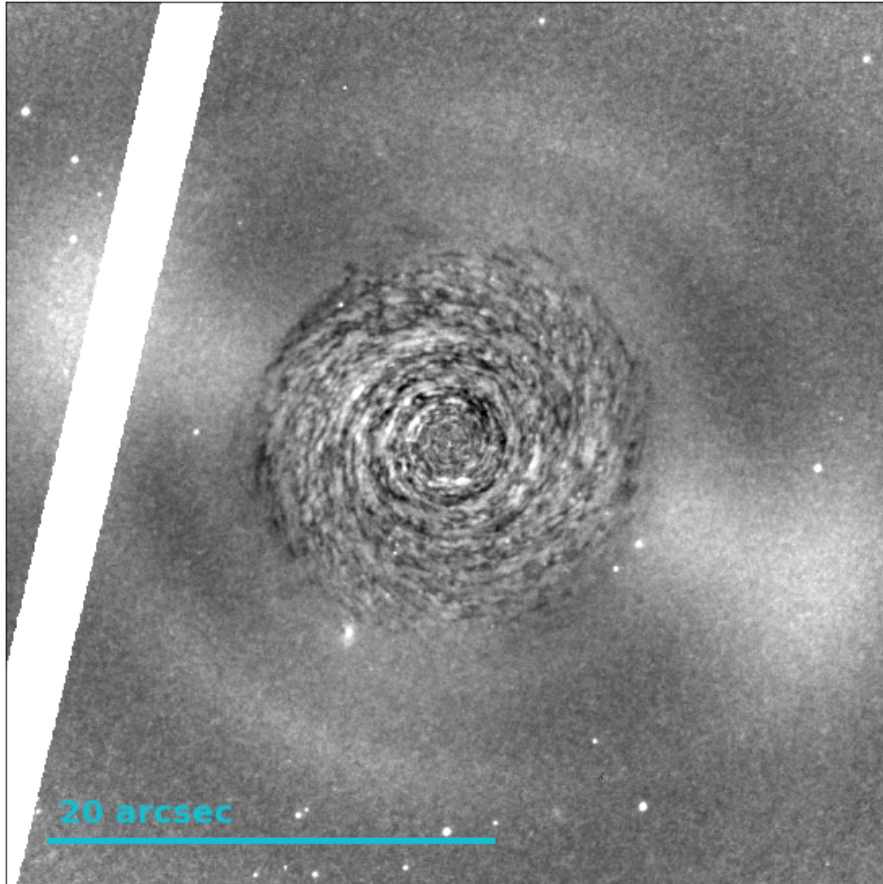
E.1 NGC 1387

Figure E.1: The normalised, residual image cutout I_{ij} for NGC 1387 in the F850LP band. The bad pixel mask $M_{ij}^{\text{bad pix}}$ is shown in white. A clear structure is visible within the galaxy center that is apparent in multiple filters.
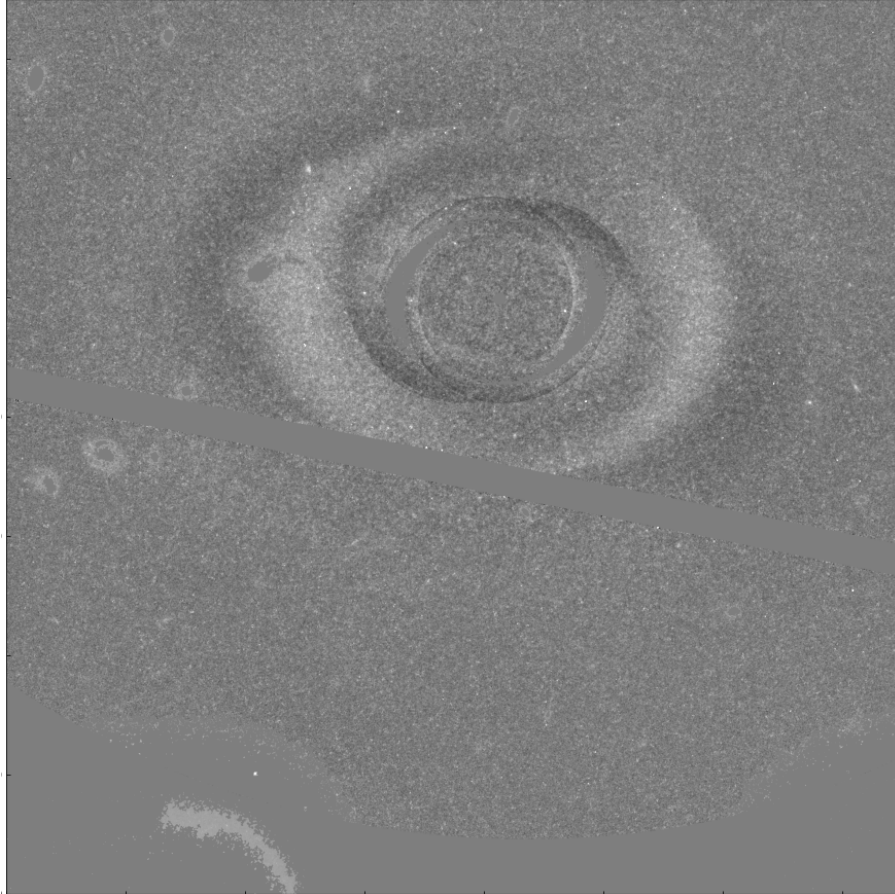
E.2 IC 1919

Figure E.2: The normalised, residual image cutout I_{ij} multiplied with the final mask M_{ij} for IC 1919 in the F850LP band. The smooth model has clearly not a been appropriate in this case.